The Fractal Character and Induced Structures of a Propane/Air Diffusion Flame

By

Hai-lin Li, BEngSc

Submitted in fulfilment of the requirements
for the degree of

Master of Engineering Science

Department of Civil & Mechanical Engineering
University of Tasmania
August 1994

Declaration

I, Hai-lin Li herby declare that this thesis contains no material which has been accepted for the award of any other degree or diploma in any tertiary institution and that, to the best of my knowledge and belief, this thesis contains no material previously published or written by another person, except when due reference is made in the text of the thesis.

Signed 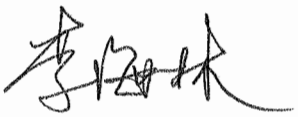 Date May 17, 1995

Abstract

Signal recovery techniques have been used to measure the periodic structures formed in a co-annular Propane/Air diffusion flame due to acoustic excitation of the flow from upstream. The flow response was sensed using the quantitative schlieren technique, and consistent results were obtained on the basis of both axial and transverse optical beam deflections and appropriate analysis of signal records. The two dominant modes of response were identified as a series of alternating ring disturbances along the flow axis at the higher frequency and a series of alternating ring disturbances containing on axis disturbances of opposite sign at the lower frequency. The former mode was essentially associated with the fuel jet shear layer, whilst the latter was associated with the outer annular shear layer surrounding the air flow from the outer nozzle. The strength of disturbances was consistent with mixing fluctuations between cold fuel gas and the products of combustion. Structures induced in the outer shear layer weakened rapidly with the distance from the nozzle, indicating a relatively sudden breakup of coherent structures caused by the excitation near the nozzle. These results provide conclusive evidence that signal recovery from noise by phase reference to an acoustic excitation is an effective means of determining structures and strength of induced disturbance of diffusion flame.

The fractal texture of Propane/Air diffusion flame were obtained by analysing the fractal distribution of flame schlieren images based on the box counting method which is an efficient method used to analyse the fractal texture of diffusion flame schlieren images with a variance of approximately 0.04 in the fractal dimension. The results suggest that diffusion flames do exhibit fractal behaviour and that the value of fractal dimension are around of 2.3~2.47, which varies with the excitation and character of turbulent flow. The Power Spectrum Density (PSD) of propane/air diffusion flame has

also been investigated. These observations of PSD appeared to be generally consistent with the fractal dimensions. A numerical simulation investigation into the fractal relationship between the original field and its schlieren images showed that there is no simple universal relationship between the fractal dimension of the schlieren image and that of the actual spatial field which gave rise to the image. However, it seems that the fractal dimension of the diffusion flame and its schlieren image are similar, whilst the fractal dimension of the schlieren image of a fairly homogeneous turbulent mixing field may exceed that of the field itself appreciably. Contours of differentiated images have potential for revealing any regular character in diffusion flames, the present work showing clear evidence of structures at approximately ±25 ° to the flame axis.

Acknowledgments

I am deeply indebted to my supervisor Prof. M. R. Davis for introducing me to the fascinating and challenging field of turbulence and combustion and for his invaluable guidance and constant encouragement throughout this project.

I would like to thank Mr. Paavo Jumppanen for sharing his expertise in computer analysis and experiment operation, and Mr. Terry McNicol for his assistance in electronic devices. Thanks are also due to Mrs. Juanita Wertepny, the secretary of the Department of Civil & Mechanical Engineering for her assistance when required.

I gratefully acknowledge Mr. Laurie Zambon, Mrs. Louise Oxley and Ms Claire Fuller (ELICOS Centre) for improving my English and correcting the initial drafts; Mrs. Maeve Parker for doing proof reading of this thesis.

Thanks are also extended to my parents and sisters for their moral support throughout the study.

Finally, I wish to express my special thanks to my wife, Xiao-qun Su for her great understanding, encouragement, support and sacrifices.

Nomenclature

Chapter 2 & 3

Capital letters:

L	distance between the flow and the detector
M	molecular weight
N	refractive index
P	pressure
R_e	Reynolds number
R_{gd}	Gladston-Dale molecular refractivity
R_{gd}	Lorenz-Lorentz molar refractivity
St_i	Strouhal number based on an inner nozzle (fd_i/U_i)
St_o	Strouhal number based on an outer nozzle (fd_o/U_o)
U	velocity (m/s)
V_c	convective velocity
X	distance from nozzle to measurement plane (m)
Y	distance from axis to sensing beam (m)

Lower case letters:

d_i	inner nozzle diameter (m)
d_o	outer nozzle diameter (m)
f	frequency (Hz)
n	refractivity fluctuations
$\overline{n}$	mean refractivity
r	radial coordinate from axis (m)
t	time (second)
x, y, z	coordinate directions, origin at nozzle centre (m)

Greek symbols:

ξ, η, ζ	coordinate displacements from measurement point (m)
δ	refractive index

δ_0	constant of integration
ρ	gas density
θ	beam deflection (radians)

Subscripts:

a	axial direction
i	inner nozzle
o	outer nozzle
p	periodic
r	radial direction
t	transverse direction

Chapter 4

Capital letters:

A	surface area
D	fractal dimension
E	dimension
H	fractal relative parameter
L	length
PSD	power spectrum density
R^m	Euclidean metric space
T	time
V	volume

Lower case letters:

f	frequency
l	turbulence integral scale

Greek symbols:

β	slope of *PSD* curve
ε	length of measurement

η	Kolmogorov scale

Subscripts:

2	two dimension
3	three dimension
f	frequency

Table of Contents

Chapter 1 INTRODUCTION

The overall structure of the flow and combustion in turbulent diffusion flames is controlled by the turbulent mixing process. In many approaches to the problem of turbulent combustion, refractive index fluctuation methods have been introduced and these have been related to experimental observations of fluctuation data obtained by the crossed laser schlieren technique. In general, such methods can determine the refractive index of flame components and under certain conditions its temperature and pressure. This thesis extends this application to investigate the periodic structures formed in the co-annular diffusion flame fluctuation due to pure tone acoustic excitation of the flow from upstream which produces identifiable signals at the excitation frequency in the flow. This approach eliminates random mixing structures and retains only the structures induced by the excitation in the signal time records that are averaged over many cycles with a time origin referred to a zero crossing of the excitation signal. The local refractive index fluctuation distribution can be determined using the Abel transform method of Minerbo and Levy (1969) to process the schlieren signal.

In addition to the laser schlieren technique, flow visualization studies of turbulent images have been used in the thesis. It has been evident that the turbulent flame is a chaotic fluid motion. The fractal analysis method developed by Mandelbrot (1983) has been used as a new tool to mathematically describe the highly contorted and roughened turbulent surfaces. The thesis also analyses the fractal character of turbulent schlieren images and attempts to find the fractal dimension relationship between the turbulent flow field and its schlieren image with reference to numerical simulations.

1.1 Literature review

Turbulent combustion has attracted increased interest in recent years and has become a much investigated branch of fluid mechanics. The demands for improved combustion efficiency and decreased pollutant emissions from a variety of combustion devices have led to the need for a clearer understanding of turbulent flows involving chemical reactions. In general, the turbulent flow fields associated with combustion devices are highly complex even in the absence of combustion. The combustion process introduces

an interaction between combustion and turbulence and makes the phenomenon much more complicated to understand and to describe. The effectiveness of many combustion systems is closely related to the flow characteristics inside the combustor and the degree of mixing obtained between the injected fuel and air. The mixing involves two important processes. Large scale structures bring into the mixing layer large amounts of reacting components from the two separated streams. Fine scale eddies enhance the mixing between the reactants at the molecular level, which is a necessary condition to initiate the chemical reaction. The understanding of this complex gas-dynamic process requires analysis of the interactions between fluid dynamics, chemical reaction, acoustic waves and heat release of the reactive system (Ballal *et al.*, 1986).

The structures buried in the flow field have been regarded as large scale coherent structures in the sense that there must be an *underlying organized vorticity connecting different parts* of the structure (Hussain, 1981) such as vortex rings. In general, the structures experience cycles of formation, growth and decay through which the flow becomes gradually independent of the initial condition. The scale and spacing of the vortex rings increases with distance downstream. There are many observations of large scale structures in diffusion flames (e.g. Lysaght *et al.,* 1982; Eichhoff and Winandy, 1985; Lysaght *et al.*, 1985; Chen and Roquemore, 1986; Miake-Lye and Toner, 1987; Cabelli *et al.,* 1988; Gutmark *et al.,* 1991). From flow visualization, it was observed that the structures are sheared and torn into fragments on the high velocity side before being swept downstream. It has been found that a number of parameters (such as Reynolds number, lifted off or attached flame base condition, chemical kinetics, nozzle configuration, secondary flow and buoyancy effect) affect the structures. The velocity and properties (e.g. density, pressure, temperature) are the parameters most often investigated. The variables in a diffusion flow are not deterministic and have to be treated as stochastic or random variables. Thus the statistical description is the only logical method for describing the phenomenon of turbulence in general (Lumley, 1970).

In spite of the complications and difficulties in understanding and describing the combustion process, several turbulent combustion models have been developed so far. The laminar flamelet concept, above all, is becoming very popular as a means of describing turbulent combustion in a regime where the chemical reaction time is short compared to turbulent mixing time scale (Peters, 1986). In this regime, chemical reactions take place within asymptotically thin layers, called flamelets, which are

embedded in the turbulent flow. The flamelet concept can be applied to turbulent diffusion flames, as well as to turbulent premixed flames. The advantage of the concept is that the flame properties can be studied in detail by experiments or numerical calculations separately from the turbulent flow. The visualization of flamelet surfaces and characterization of the flame configuration form the base to take the advantage of the flamelet concept. Instantaneous schlieren images reveal the complicated nature of the flamelet surface. They exhibit multiple scales of wrinkling and this suggests that it will be rather difficult to characterize and quantify the flamelet surface in the absence of any appropriate analytical means.

Of particular concern in this thesis are diffusion (non-premixed) flames which are the major contributor to combustion energy usage in large industrial boilers and furnaces. The fluid dynamics involved in these types of flames are related to mixing layer flow, which is governed by large scale vortices. The roll-up and growth of these vortices are determined by instability forces and mutual interactions (Brown and Roshko, 1974). The large scale structures entrain flow from the two sides of the shear layer and mix the flow at both large and small scales, leading to the molecular mixing necessary for reaction. Understanding of the important role of large coherent structures in mixing layer dynamics will open up the possibility of controlling the flow in the combustion to improve their performance. The development of large scale vortices in a shear layer is influenced by the reaction through heat release and changing of density gradients. In turn, the vorticity controls the reaction by the turbulent mixing process. The physical mechanisms involved in this interaction are not fully understood.

In the theoretical area, the Navier-Stokes equations are still the most useful mathematical equations governing fluid flows, which are valid for instantaneous values of the quantities involved. However the Navier-Stokes equations of motion become considerably more difficult to deal with if density or velocity is considered to be a variable or a function of space and time. For turbulent flows, the Navier-Stokes equations can only be treated further mathematically if average or mean values are substituted, instead of the instantaneous values, in simplified equations.

Due to the extremely complex phenomenon of the turbulent flame, the understanding of turbulence has been advanced more by experimental studies than by fundamental theoretical investigation. Experimental studies are still the most important method for describing the phenomenon of turbulence in general, even though of necessity the two approaches must advance together. From the experimental point of view, the complex

nature of turbulence has led to the development of various techniques for turbulence measurement. Winarto (1979) suggests that the turbulence measurement techniques can be classified into two major groups, probe techniques (e.g. hot wire and film, resistance thermometer, thermocouple, pulsed-wire technique, pressure transducer or microphone) and non-probe techniques. The non-probe techniques can be described as flow visualization techniques, frequency shift or Doppler shift anemometers (e.g. Particle image velocimetry, Laser Doppler Anemometer, Sonic Anemometer), and optical techniques (e.g. shadowgraph, schlieren and interferometry). More detail about turbulent measurement techniques can be found in works by Corrsin (1963), Bradhsaw (1971), Hinze (1975), Winarto (1979), Goldstein (1983) and Hunag (1993).

Flow visualization is generally used as a tool to understand the mechanisms affecting the large scale structures of turbulence and perhaps to identify new flow phenomena. The visualisation studies of diffusion flames have been quite effective in revealing particular features of the mixing and reaction process, in particular for smaller size flames and where the direct access of a probe is difficult. For example, the schlieren visualization and image processing technique can not only provide simultaneous high resolution, time lapse results, which facilitate the detailed interpretation of the measurement data but also digital image processing is specially useful in extracting the patterns of the dynamic process (e.g. Rosensweig *et al.*, 1961; Becher, 1977; Long *et al.*, 1979, 1981, 1983; Balint *et al.*, 1985; Vranos and Liscinsky, 1986; Winter *et al.*, 1987; Chao *et al.*, 1990). Flow visualization using schlieren photography is feasible whenever gradients of the index of refraction, and therefore gradients in density, exist. These observations give clear evidence of very regular, vortex-like structures within a diffusion flame near to the nozzle which break up ultimately into a much more disorderly reaction and mixing region further from the nozzle. More advanced optical methods such as laser induced fluorescence and planer imaging tomography have revealed more detailed cross sections of mixing structures in diffusion flames, and analyses of the progress of the reacting flame front have also demonstrated the development of regular vortex flame front structures (Chao *et al.*, 1991; Gutmark *et al.*, 1991; Paschereit *et al.*, 1992; Brokman and Levin, 1993).

Flow visualization studies, particularly schlieren and laser tomography, show that flamelet surfaces can be extremely rough and therefore difficult to characterise (Suzuki and Hirano, 1984; Wu and Law, 1984). Depending on turbulence conditions the flamelets may form a continuous sheet, several sheets, or may be fragmented into many separate sheets. The local structure of these flamelets will match that of a steady

laminar flame for low levels of turbulence (the wrinkled-laminar-flame case), but the structure is perturbed by surface curvature and by the straining action of the turbulent velocity field as the turbulence increases in intensity. These processes lead to the formation of so-called stretched laminar flamelets. At high levels of turbulence, flamelets are highly fragmented and reaction is dispersed into small pockets of reacting gas.

In physically hostile environments such as combustion zones, there are some difficulties with mechanical measuring probes, such as hot wires, to give a clear indication of a particular flow parameter, since they cannot sustain high temperature or are subject to large errors in measurements. In particular, they cannot be utilized to measure density, pressure or species concentration fluctuations and are difficult to calibrate due to their response to velocity, temperature and composition of the flow. However, some of these difficulties can be overcome by using optical techniques which require no probe to be inserted into the flow and which have a well defined response to mixture refractive index. Optical measurements have many advantages over other techniques. Perhaps the major one is the absence of an instrument probe that could influence the flow field. The light beam can also be considered as essentially inertialess, so that very rapid transients can be studied. Measurements by laser-based systems such as the laser doppler anemometer, and the Rayleigh scattering technique have also been extensively developed. Reviews on this topic have been given (for example) by Johnston *et al.* (1985), but such methods involve the presence of seeding particles in the flow and essentially detect particle motion only.

Probably no real turbulent flow is isotropic or even homogeneous at the large scale. Even assumptions of isotropy and homogeneity can be questionable on a small scale. However, by assuming that the turbulent flow is locally isotropic, it is possible to utilize a technique for measuring turbulent quantities which is related to density fluctuations rather than to the density gradient fluctuations (e.g. Wilson and Damkevala, 1970). Furthermore, since the density fluctuation is related to temperature, pressure and species concentration fluctuations, it is possible to extract information about those fluctuations from the results of measurement by means of the quantitative schlieren technique (Winarto, 1979). The schlieren technique is based on the principle that when a beam of light passes through turbulent flame, the properties of the light beam (energy intensity and path of propagation) will be modified. All these changes will be in response to the mixture refractive index. The refractive index becomes an effective reaction progress variable as it is dominantly related to local temperature and

the progress of a reaction as represented by the extent to which combustion of mixture components has occurred. A more detailed statement can be found in Weinberg (1963).

There have been an increasing number of studies of using the schlieren technique to investigate diffusion flame structures (e.g. Davis, 1971, 1972, 1975, 1987, 1989; Wilson and Damkevala, 1970; Winarto, 1979, 1984; Davis and Rerkshananda, 1993; Davis and Jumppanen, 1993). Davis (1971) found an increase of the fluctuation intensity in proportion to the fourth power of the mean flow Mach number over the subsonic Mach number range by using single beam schlieren system. Davis (1975) used a combination of the crossed beam and Abel transform results to obtain both the scale and fluctuation intensity of the turbulent structure separately. Later, Davis (1987) found the crossed beam schlieren system is well suited to determination of turbulent mixing properties in a diffusion flame of air and hydrogen. He observed *"The mean refractive index distribution is dominantly influenced by the temperature in the flame, and on the lean or rich side of stoichiometric mixture ratio the refractive index is directly related to the progress of turbulent mixing and of the reaction process".*

Excited jet flows have been commonly used to investigate possible noise suppression techniques for jet flows. For unexcited jets (having very low level and broad band pressure fluctuations), Hussain (1981) proposed that the coherent structures in the near region are difficult to identify because of the vast dispersion in shape, size, orientation, strength and convection velocity. Basically, the flow is unstable over a substantial range of disturbance frequencies. Thus instability is induced randomly by disturbances which contain components in this broad range of frequency. For these reasons the practical identification of coherent disturbances in unforced cases is very difficult. Excitation was observed to reduce in intensity the random components in the radiated noise spectrum. Low levels of acoustic forcing in jet flows tend to promote coherent structures in the jet flow that lock on to the excitation and respond in a manner that is consistent with linear stability theory. High levels of forcing promote a transfer of energy from broad band turbulence into the large scale structures in the near nozzle region and greater levels of turbulence in the far field as the coherent structures begin to break up (Tanna and Ahuja, 1985). Using controlled excitation experiments, there have been an increasing number of studies of both time average distributions and physical features showing the existence of large scale coherent structures. Turbulence intensity and spreading rate studies of the near field of an axisymmetrical jet showing strong dependence on the exit flow characteristics (boundary condition, initial

condition, and Reynolds number) have been reported by many researchers (Crow *et al.*, 1971; Hussain *et al.,* 1980; Crighton, 1981; Davis and Rerkshananda, 1993; Davis and Jumppanen, 1993). The detailed characteristics of the flow under acoustic excitation, such as the multiple-eddy merging process, the braid-formation and self-rotating processes, and jet-boundary expansion, etc., can clearly be observed by schlieren visualization and image processing technique.

The existence of large-scale structures in the shear layer of turbulent flows has been noted and confirmed by an overwhelming number of investigators. Experimental evidence has revealed that the evolution of large coherent structures plays a key role in mass entrainment and turbulence characteristics in the flow (e.g. Brown and Roshko, 1974; Winant and Browand, 1974). In addition to the natural flow properties, the interest in excited-flow structures and the potential application of several controlling techniques on flow manipulation have recently attracted much attention. Acoustical excitation has been recognised as an effective tool for controlling the shear flow (Ho and Huerre, 1984), and the importance of the excitation frequency of the flow has been noted. The jet flow is very sensitive to the fundamental excitation, even with a low-level excitation. The flow responds to the excitation with an early initial growth of the fundamental wave in the initial region and more organised formation and pairing of vortices as compared to the natural jet (Han, 1991). At certain frequencies, when the excitation level is raised high enough, specific forced-flow structures other than the well-known natural characteristics, become dominant. These structures and their vortical evolutional characteristics are less understood and are of current importance to research on manipulating turbulent flow.

In the last twenty years new statistical methods for the analysis of rough surfaces and rough, irregular curves have been developed as a separate mathematical subject known as fractals. The theory of fractals has been developed by Mandelbrot (1983) to provide a tool for a mathematical description of highly contorted and roughened surfaces. Basically, fractals are objects that display self-similarity over a wide range of scales. Each fractal object is associated with a characteristic dimension called the fractal dimension, which forms a basic measure of roughness of the surface. Fully developed turbulence has been thought to consist of a hierarchy of eddies, or scales of various orders, and hence to exhibit fractal behaviour (Mandelbrot, 1983). Sreenivasan and Meneveau (1986) have found that the similarity law actually holds for constant property surfaces, such as iso-velocity and iso-concentration surfaces, as well as for the turbulent/non-turbulent interface. This occurred in a range of scales between an outer

and an inner cutoff scale. The outer scale is the turbulent large eddy formation scale while the inner scale is the Kolmogorov microscale. The observed values of fractal dimension range from 2.32 to 2.40 for the turbulent/non-turbulent interface in various nonreacting turbulent flows (Sreenivasan, 1989, 1991; Prasad and Sreenivasan, 1990), even though the mathematics-physics connection is still unclear.

Gouldin (1987) for the first time tried to apply the theory of fractals to describe the flamelet surface. In his argument, the influence on turbulence of combustion is not important, and he considered that in the limit of large ratio of turbulence intensity to normal burning velocity, the flamelet will behave as a passive, constant property surface in the given turbulent flow field. The similarity law must therefore apply to the flamelet surface as well. On the basis of this argument, he developed a model to predict the turbulent burning velocity, which seems to show a good agreement with the available experimental data. In this model Gouldin adopted the value of 2.37 for the fractal dimension of flamelet surface, with reference to the measured values for nonreacting flows. This value has to be based on the measurement of the actual flamelet itself. Takeno (1990) investigated the fractal-like character of the laminar flamelet surface in turbulent premixed combustion of lean methane air mixtures by using the laser tomography technique to visualize the instantaneous flame surface in the two-dimensional section cut by the laser sheet. He found the flame surface actually exhibits a self-similarity behaviour in a narrow range of scale, but he doubted the surface is truly fractal because the fractal magnitude and scale range are smaller than expected.

There have been a lot of convincing evidence to show that the fractal dimension is a useful concept for analysis of complex regions in turbulent flow which has two advantages (Sreenivasan, 1986, 1991). First, it enables us to venture beyond the existing statistical tools, which are rather heavily based on central-limit-type arguments. Second, it has allowed us to enter a number of areas of non-linear science. As a result of the introduction of fractal dimension into turbulent flow, there has been considerable work in the direction of building fractal-based models for turbulent combustion (Mandelbrot, 1975; Gouldin, 1987, 1988, 1989; Sreenivasan, 1986, 1989, 1991; Takeno, 1990). The exploration of the fractal in turbulent flow is still in a growth phase (Sreenivasan, 1991).

The approach to be adopted in this thesis extends the application of the schlieren technique to the turbulent combustion problem where the observations must be related

to the refractive index fluctuations in the combustion zone. The application of a regular, periodic acoustic excitation of the diffusion flame provides a phase referenced excitation signal so that measured signals from the laser schlieren sensing system can be averaged to eliminate random or turbulent signal components and recover the component due to the excitation. The density gradient of turbulent flow can be obtained via the Abel transform of the measured signal. In addition, the schlieren turbulent image taken by a video camera will be used to investigate the fractal distribution of turbulent images. Because of the difficulty in the direct measurement of fractal dimension in the flame, it is a very useful attempt to find the fractal dimension relationship between the turbulent flow field and its schlieren image by a numerical simulation method in the latter part of the thesis.

1.2 Outline of the thesis

The principles of the schlieren technique and its application are introduced in Chapter 2. Two important experiments are described in this chapter: (a) the schlieren single average time record of the diffusion flames induced by controlled excitation; (b) the acquisition of turbulent schlieren images to investigate fractal distribution. The Prewitt image processing principle, which helps to reveal more detail from flame images, is also reviewed in the latter part of this chapter.

Chapter 3 describes the numerical processing of a schlieren single record, which includes full details of the Abel equation transform technique and its application for the solution of the axial and transverse averaged schlieren signals. After a series of integrations of Abel transformed results, the complete distribution of the convecting refractive index is formed. A discussion of experimental results is included in the latter part of the chapter.

The principles of fractal dimension and its application in the turbulent field are introduced in Chapter 4. Varied flame images are used in analysing the fractal dimension images and are calculated by the box counting method. A very important feature for investigating the fractal dimension relationship between the diffusion flame density field and its schlieren image is considered using numerical simulation. Additionally, the spectrum analysis of schlieren image is reviewed in this chapter as this provides useful information for placing the fractal analysis in a more conventional context. Finally, the conclusions for both parts of the work are stated in Chapter 5.

Chapter 2 OPTICAL OBSERVATION OF DIFFUSION FLAMES

This chapter considers the analytical foundation of the two experimental methods to be used here: (1) Observation of the structures induced by periodic acoustic excitation of a diffusion flame and (2) investigation of the fractal structures of diffusion flame images. Both experiments are applied to the same combustion facility to generate the diffusion flame, but used different measurement systems. The first experiment used the well known laser schlieren technology which is basically a modification, developed mainly by Davis (1975), of the Toepler schlieren technique. The second used the schlieren image frame acquisition and processing system which is basically another modification of the schlieren technique and was developed by the Department of Civil and Mechanical Engineering, University of Tasmania (1993). This system has image analysis software specifically written for the schlieren image application but which can also be used in applications other than schlieren image. The equipment comprises a video camera with fast electronic shutter, frame grabbing, interface unit and image processing software developed specifically for this work.

2.1 The introduction of the laser schlieren technology

The use of a schlieren optical system to make quantitative measurements of density fluctuations has been described by Davis (1971,1972). This measuring technique is one of three optical methods (shadowgraph, schlieren and interferometric techniques) which are based on the fact that the propagation path of a light beam is modified as the light beam travels through a region of space which is filled with an inhomogeneous fluid. All three techniques are valuable when visualising flows in which density differences occur naturally or are artificially induced. When used quantitatively, these techniques can often be used to determine density, pressure, and / or temperature variations in the flow. From these, other properties of the flow field (e.g. laminar versus turbulent nature of the motion, boundary-layer thickness, points of separation, and reattachment) can often be inferred (Winarto, 1979). The shadowgraph technique is sensitive to the change of the second derivative of

refractive index (or density), whereas the Mach-Zehnder interferometry technique is sensitive to the absolute density changes. The schlieren light beam is sensitive to the change of the first derivative or density gradient in the flow field.

One difficulty in applying most optical techniques is obtaining localised or point data of the flow properties. Fisher and Krause (1967) were the first to suggest the use of the two orthogonal beam system to detect the flow properties at the beam intersection point. Wilson and Damkevala (1970) applied the cross correlation technique to investigate the statistical properties of turbulent density fluctuations using a system with a thin laser beam and a photo detector. The system can resolve the point data of flow properties, and can be termed as a dynamic and quantitative system, unlike the conventional schlieren system which is considered to be a qualitative system (using a photographic plate). By using the locally isotropic and homogeneous flow assumptions, Davis (1971) obtained the point data of density gradient intensity and integral length scale via the Abel transform of single beam system. In 1972, Davis applied this technique to supersonic flows. Subsequently, Davis (1975) combined the results of the Abel transform and cross beam correlation to obtain the density gradient intensity and the integral length scale separately. In this version of the measuring system, a position sensitive photo-diode and a laser beam were used instead of an incandescent lamp and a photomultiplier tube. A substantial improvement of signal to noise ratio was obtained by this type of detection system. Winarto and Davis (1984) used this system for making detailed measurements of high subsonic Mach number axisymmetric turbulent jets of air, in both heated and unheated conditions as well as of the hydrogen diffusion flame (Winarto, 1979). Davis and Rerkshanandana (1993) used the quantitative cross beam schlieren system further to investigate the unexcited dynamic behaviour of large scale coherent structures for subsonic heated flow at relatively low Reynolds numbers. They arranged the system with radial-axial detecting beams to obtain the cross correlation functions which then show the signature of large structures. The assumptions of separable variables and axisymmetry (arising from the isotropic and homogeneous flow assumptions) of the kernel of the Abel equation are reexamined in the zone with large structures in their work. More recent research on a diffusion flame using the schlieren system has been published by Davis and Jumppanen (1993). By using the feature that the quantitative, dynamic laser schlieren sensing system has a spatial averaging characteristic response that makes it particularly sensitive to spatially coherent structures in a turbulent mixing region, they have found that a coaxial

turbulent diffusion flame has maximum response at two distinct Strouhal numbers associated with mixing at inner and outer shear layers.

The principle aim of the first investigation of this thesis is to establish the structure of disturbances of a diffusion flame flow density by the schlieren technique. In the experiment it is assumed that the density fluctuations are related to the appropriate mean property gradients in terms of coefficients relative to pressure, temperature and composition for the refractive index. Observations were made for a set of values of axial distance and exciting frequency.

In the present experiments, the quantitative cross beam schlieren system is used to investigate the structures induced by periodic acoustic excitation of a diffusion flame. As shown in Figure 2.1, a Cartesian system of coordinates is defined as follows. The origin is at the centre of the circular nozzle exit plane. The x-axis is perpendicular to the exit plane and in the direction of the jet axis. The y and z-axes are mutually orthogonal to each other and to the x-axis. The nozzle exit plane is then defined or identified as the y-z plane at x = 0, other y-z planes, being parallel to the nozzle exit plane, can be defined for various values of x. The light beam is traversed on the y-z plane with the beam direction being in the y direction and the traverse direction in the z direction. To simplify the mathematical analysis it is useful to define a new set of axes ξ, η and ζ which are parallel to the x, y and z axes respectively. The origin of the new set of axes is located at a point (x, 0, z).

The relationship between the optical path and the refractive field has been presented by Weinberg (1963) as:

$$\theta = -\int \frac{1}{N}\frac{\partial N}{\partial \xi} d\eta \qquad (2.1.1)$$

where

θ = angle of deflection in x-y plane

N = refractive index

η = direction along the light path

ξ = direction perpendicular to the light path.

The refractive index of any gas is related to the gas density by the well known Gladston-Dale empirical equation (Weinberg, 1963)

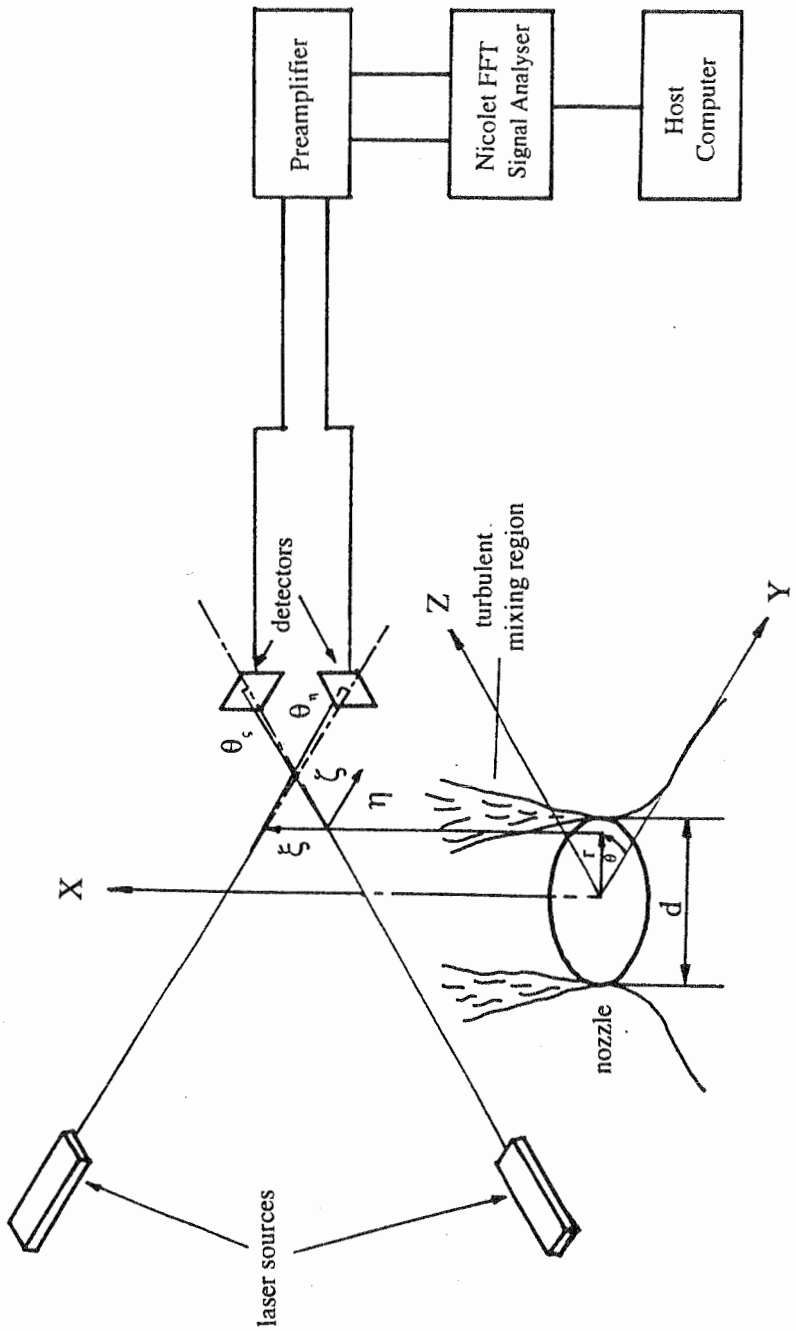

Figure 2.1 The crossed beam Laser Schlieren measurement system.

$$(N-1)/\rho = \delta/\rho = R_{gd} \qquad (2.1.2)$$

Where ρ is the gas density and R_{gd} is generally known as the Gladston-Dale constant or the Gladstone-Dale refractivity.

Because $N = 1+\delta$, and δ is of the order 0.0003 (0.000293 for air), the variation of refractive index N will be replaced by δ.

$$\theta \approx -\int \frac{\partial \delta}{\partial \xi} \mathrm{d}\eta \qquad (2.1.3)$$

The refractive index (N) of a turbulent flame can be defined by a component of local mean change ($\bar{n}$) relative to the ambient, a component of local fluctuating part (n) and an ambient value (N_a) such as that $N = N_a + \bar{n} + n$. The refractive index N_a is very close to 1 and considered to be constant outside the flow field, and much larger than the summation of $\bar{n}$ and n. Similarly, the angular deflection θ consists of a mean value, $\overline{\theta(t)}$, and a fluctuating value, $\theta(t)$. So we have

$$\Theta = \bar{\theta} + \theta = -\int_{-\infty}^{\infty} \frac{\partial \bar{n}}{\partial x} dy - \int_{-\infty}^{\infty} \frac{\partial n}{\partial x} dy \qquad (2.1.4)$$

The investigation of mean fluctuation value ($\bar{n}$) has been reported by Rerkshanandana (1989). In this experiment, only the local fluctuating part (n) has been investigated and will be separated from the mean value ($\bar{n}$).

2.2 Experiment of laser schlieren measurement

Experiments in the first part of this research were carried out on a combustion research facility which allowed the laser schlieren measurement system to be applied to a diffusion flame formed by a jet of fuel gas and a co-flowing jet of air.

The laser schlieren flow measurement system consists of two orthogonal and identical laser beams (0.5 mW Spectrum Physics helium-neon lasers) and deflection sensing photo-diodes (United Detector Technology PIN-SC-10 sensing the deflection from the helium-neon lasers). One laser is fixed whilst the other can be

traversed horizontally and vertically. In this way the lasers can be made to traverse through different cross sections in the flow. The laser beams pass through the flow and generate the angular deflection about the z (θ_ζ) and y (θ_η) axes (Figure 2.1). These angular deflections are sensed by two photo-diodes and are converted into electrical analogue output signals.

As shown in Figure 2.1, the laser beam traverses the η-ζ plane along the η- direction and is deflected in directions orthogonal to its path, i.e. in the ξ-ζ plane. This deflection can be resolved into two orthogonal components, namely the axial component in the ξ-direction and the radial (transverse) component in the ζ-direction. The operation of the photodetector is such that each of the two components of the angular deflection can be measured separately. Each photo-diode senses both vertical and horizontal deflection independently and has separate outputs for either direction (θ_a corresponds to a horizontal beam deflection). More detail about the schlieren measurement system can be found in Winarto (1979) and Rerkshanandana (1989).

The angular deflection experienced by the beam in the axis (vertical) direction is thus given below:

$$\theta_a = \int \left(\frac{\partial \delta}{\partial x} \right) dy \qquad (2.2.1)$$

and similarly, we have the radial (horizontal) deflective angle,

$$\theta_r = \int \left(\frac{\partial \delta}{\partial z} \right) dy \qquad (2.2.2)$$

The voltage outputs from the photo diode were connected to a pair of differential amplifiers (Princeton Applied Research Model 133 low-noise preamplifier). The outputs from the amplifiers were averaged by a Nicolet 660B dual channel FFT analyser having a 1024 point signal record length, and transferred to on H.P.286 personal computer via the parallel bus RS323-c.

In the context of the present work, there are two approaches to investigate the distribution of the disturbances of density induced in the diffusion flame. One uses

the vertical deflection component (θ_a) and another uses horizontal deflection component (θ_r) to analyse the properties. Theoretically, both signals should ultimately lead to the same result. However, the impossibility of having exactly identical experimental conditions for two series of measurements (e.g. laser source, photodetector, preamplifiers) will inevitably cause some differences. The radial component of a signal positioned on the centre line of the nozzle will be generally less sensitive to the flow near the nozzle position than further downstream as the flame will not be fully developed and structures in the initial thin shear layer of the flame will be more axial-symmetric. However, the vertical component output signal will be sensitive to the flow when the beam is at the nozzle axis even if the induced structures are axisymmetric.

In general, the frequency and spatial response of this system depends on the combined effects of all the component characteristics in the detecting system, such as the light beam thickness, the preamplifier, and the signal analyser which are known from the manufacturer's data and the theory of signal analysis. To redress the uncertainty of non-linear effects, small perturbation signal averaging techniques were used to evaluate flow responsiveness to acoustic forcing. In this method, the mixing diffusion flame is excited within the upstream nozzle by a periodic acoustic signal. The excitation provides a phase reference to the averaging signal which can be applied to the detected schlieren output over an arbitrary number of periods with a time origin referred to a zero crossing of the excitation signal. This approach eliminates the random mixing structures and retains only the structures induced by the excitation in the signal time records from the schlieren system.

The combustor used for the diffusion flame study is mounted on a two direction traversing base (Figure 2.2). The combustor can be moved in a direction orthogonal to the one laser. Alternatively, the combustor may be moved vertically. Figure 2.3 shows a photograph of the laboratory equipment in use. The combustor is a concentric nozzle system, consisting of a central propane jet surrounded by a coannular air jet. The flame was stabilised by providing a flat annular face between the co-current unmixed fuel and air flows. The combustor comprises an inner circular nozzle (gas nozzle) and an outer co-annular nozzle (air nozzle). The inner nozzle has a diameter of 6 mm and carried propane gas at an exit velocity of 2.5 m/s (*Re* approx. 1000). The outer co-annular nozzle, having an inner diameter of 10 mm and an outer diameter of 20 mm, carried atmospheric air at an exit velocity of 2.0 m/s (*Re* approx. 3000). The diffusion flame was subjected to excitation from a

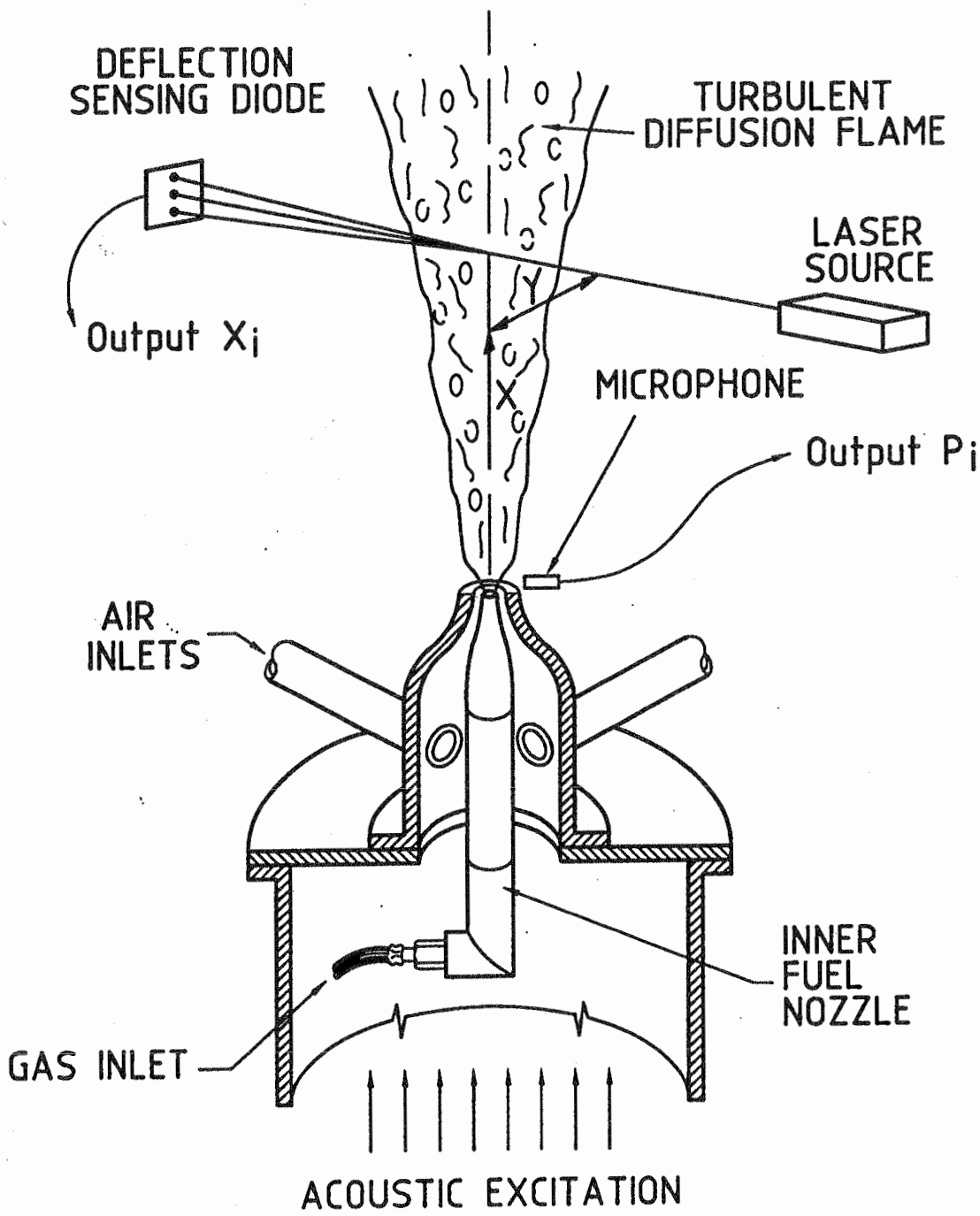

Figure 2.2 General arrangement of combustion nozzle system and measurement system.

loud-speaker located beneath the nozzle system as illustrated in Figure 2.2. The loud-speaker was driven by a signal generator. Perturbations of sinusoidal form were normally used. This arrangement enabled repetitive measurements at any given phase in the perturbation cycle. Two condenser microphones were calibrated to sense the acoustic pressure and were located in the wall of the air flow contraction nozzle just ahead of the nozzle exit, and also just outside the shear layer between the outer air flow and surrounding air close to the nozzle exit plane. A signal generator was used to produce the excitation signal and the trigger signal for the FFT analyser. In the present report, the trigger signal is input to channel A and the analyzer was used in single averaging (or single recovery) mode.

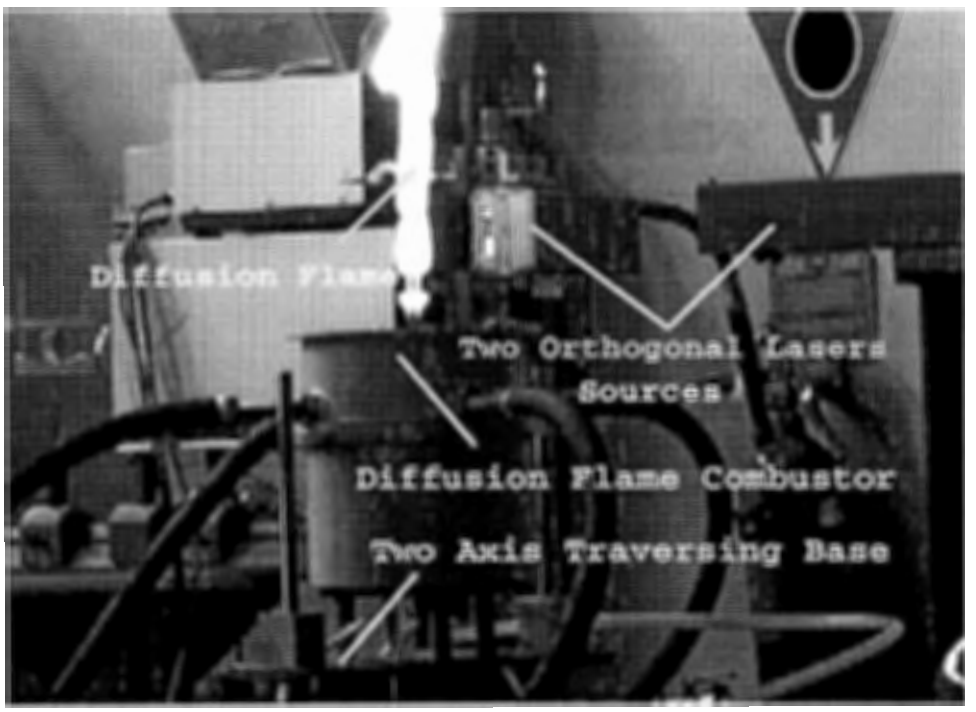

Figure 2.3 Photograph of the laboratory equipment in use (with very low flame velocity).

This system formed a vertical turbulent diffusion flame with a distance from the flow axis of visible length of approximately 300 mm (Figure 2.3). The range of fuel and air discharge velocities from the nozzle was restricted by the conditions under which the diffusion flame can be stabilised and attached to the nozzle. The overall structures of the diffusion flames at the test conditions are shown in Figure 2.4 under series conditions. There is clear evidence of both the inner and outer regions of mixing, the latter having a much larger physical scale. Of particular interest is the

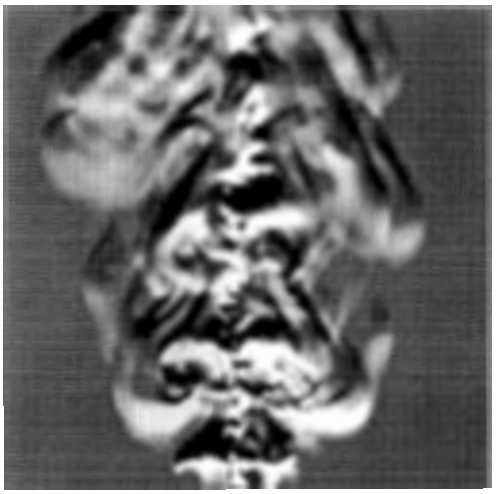

(a1)

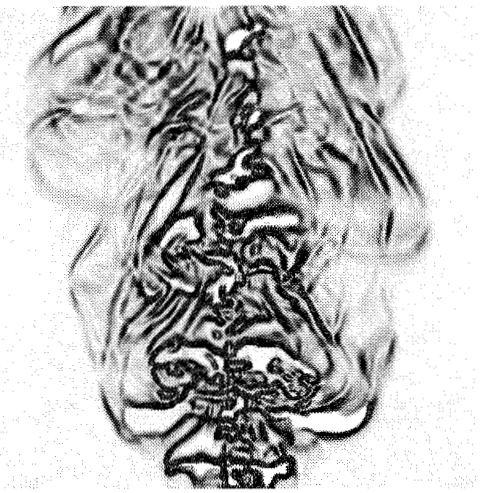

(a2)

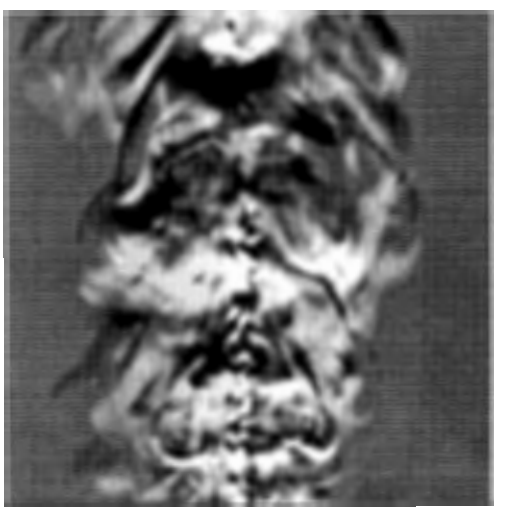

(b1)

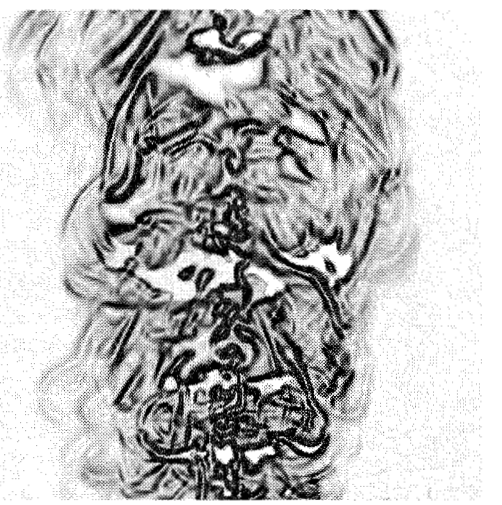

(b2)

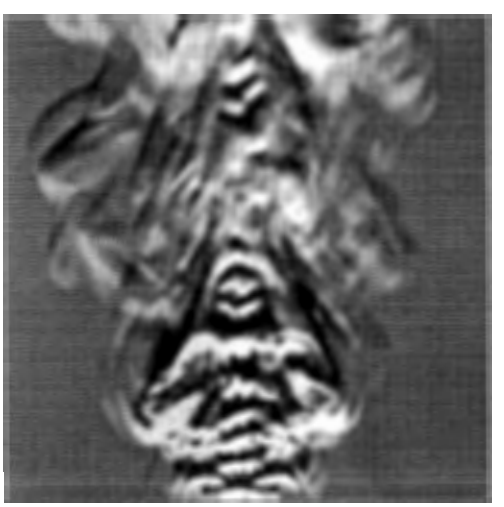

(c1)

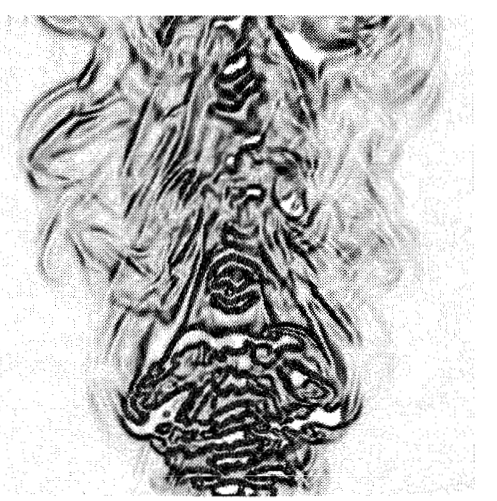

(c2)

Figure 2.4 Visualisations of the diffusion flame. (a1) (b1) (c1) Instantaneous schlieren images. (a2) (b2) (c2) Image enhanced by Prewitt filter algorithm. (a) Natural flow. (b) 40 Hz excitation. (c) 420 Hz excitation.

effectiveness of the Prewitt image enhancement filter algorithm in clearly delineating the structures embedded in the original schlieren image (Figure 2.4). More detail about Prewitt image processing will be discussed later (section 2.5).

Figure 2.5 shows the excitation signal used in the investigation. The strength of the signal was restricted for the same reason as velocity to produce conditions under which the diffusion flame can be stably attached to the nozzle. The excitation signal is not perfectly symmetrical due to imperfection in the loud speaker system and inherent geometric features of the nozzle chamber system which are not axisymmetric. These factors will have implied consequences with regard to the interpretation of the time averaged signal records and may ultimately have contributed to discrepancies between axial and radial resolution of the induced coherent structures which are assumed to be axisymmetric.

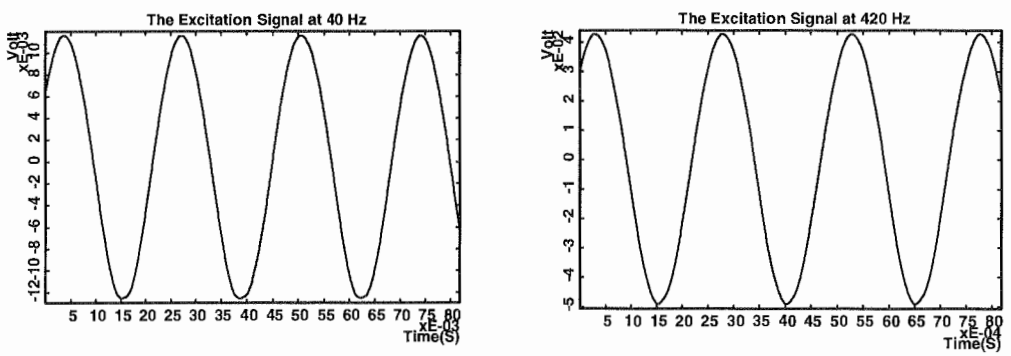

(a) (b)

Figure 2.5 Excitation signals of diffusion flame. (a) 40 Hz (b) 420 Hz (0.1 volt = 89 Pa for 40 Hz and 474 Pa for 420 Hz acoustic pressure at nozzle exit).

In the present work, the measurements were made at two fixed values of X, namely at X = 35 mm (X/d = 5.83), X = 70 mm (X/d = 11.67), where d = 6 mm, is the nozzle exit diameter. At each value of downstream distance (X/d), the beam was set at different positions in z-direction to record a set of average signal records. The overall distribution of the structure induced in the diffusion flame can be obtained by processing these results.

The experimental condition of the images are as shown below:

(1.) Low frequency excitation diffusion flame.

Excitation frequency = 40 Hz
Excitation strength = 0.012 V, correspond 21.9 Pa at nozzle exit
Velocity of fuel = 2.5 m/s Velocity of air = 2 m/s
Nozzle dimeter = 6 mm Temperature of ambient = 20°C

(2.) High frequency excitation diffusion flame image.
Excitation frequency = 420 Hz
Excitation strength = 0.045V, correspond 252 Pa at nozzle exit
Velocity of fuel = 2.5 m/s Velocity of air = 2 m/s
Nozzle dimeter = 6 mm Temperature of ambient = 20°C

The averaged schlieren signal, representing the refraction angle, was recorded as a time record for various positions of the detecting beam at different distances from the flow axis. To provide reliable data for the Abel equation inversion and to eliminate background noise, the averaging was carried out over more than two thousand cycles of excitation and response. The results were recorded as follows.

All axial fluctuating component averaged signals are identified in files:
A35.xx, A35.xxx, A70.xx, A70.xxx.
All radial fluctuating component averaged signals are stored in files:
R35.xx, R35.xxx, R70.xx, R70.xxx.

Where 35 or 70 indicates whether the laser beam is located at 35 mm or 70 mm from nozzle exit, xx or xxx is a two digit or three number, which represents the laser beam distance (mm) from the nozzle axis. At 40 Hz excitation condition xx is a two digit number and at 420 Hz xxx is a three digit number, which represents the laser beam distance ($10^{-1} \times mm$) to the nozzle centre (axis) at 420 Hz excitation condition.

The average signal records are shown in Figures 2.6 to 2.9 for axial and radial beam deflections respectively. These figures show a series of various radial locations of deflection beam records. As can be seen the records are quite smooth and regular in general. Some exceptions appear in the radial component records with the laser on or near the axis with a position close to the nozzle exit with low frequency (Figure 2.6, R35.00, R35.02) and with high frequency excitation (Figure 2.7, R35.000). In the former case, the signal is relatively small (less than 10% of the maximum value of A35.00) and it appears that the irregularity apparent is due to lack of symmetry of

the other dominant mode of mixing at approximately ten times the excitation frequency. The existence of a small but finite averaged result on the axis in these cases indicates that the excitation is not perfectly symmetrical due to the small excitation frequency component (Figure 2.5) and that this high frequency inner structure, although not being directly excited, has a tendency to phase lock to the lower excitation frequency. This is evidenced by a near regular fluctuation on the small residual averaged record. However, these effects are quite small and are apparent only in radial observations with the laser passing through the flow axis. The averaged records at the outer edge of the flow with high frequency excitation show the presence of more irregular, random fluctuations, but this is merely a consequence of the very small response to high frequency excitation in this region of the flow. This phenomena suggests that the axis component signal is more reliable than the radial. It would appear to be inevitable that signals with the laser outside the region of flow will reflect some residual small random noise effects, whilst the radial deflection record with the sensing beam on the flow axis indicates more specifically the limitation due to slightly imperfect axisymmetry of the excitation. Analysis of these records and extraction of the structures induced in the flow will be discussed in Chapter 3.

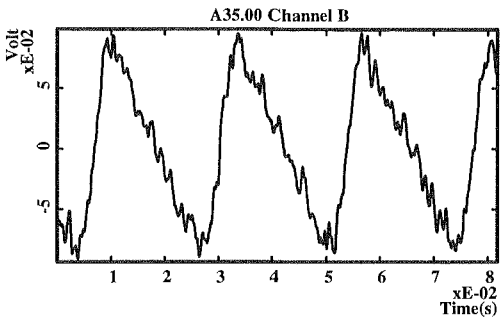
A35.00 Channel B
Volt
xE-02
xE-02
Time(s)

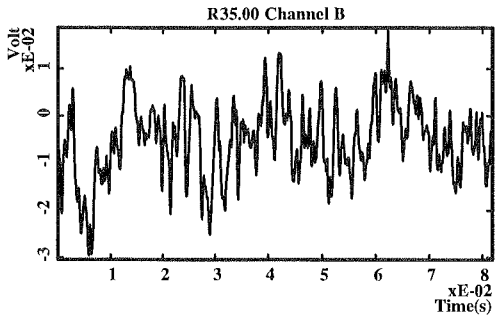
R35.00 Channel B
Volt
xE-02
xE-02
Time(s)

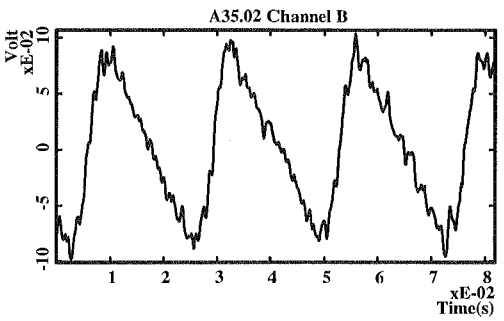
A35.02 Channel B
Volt
xE-02
xE-02
Time(s)

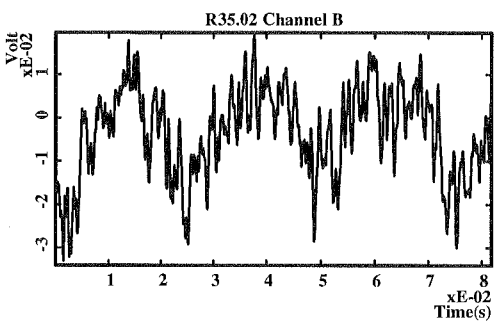
R35.02 Channel B
Volt
xE-02
xE-02
Time(s)

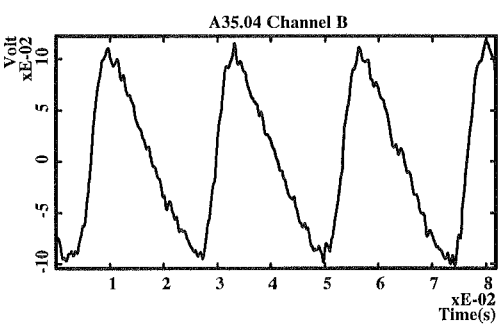
A35.04 Channel B
Volt
xE-02
xE-02
Time(s)

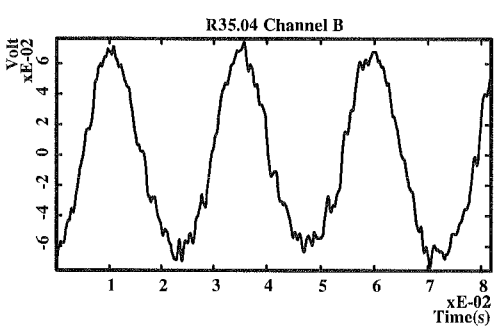
R35.04 Channel B
Volt
xE-02
xE-02
Time(s)

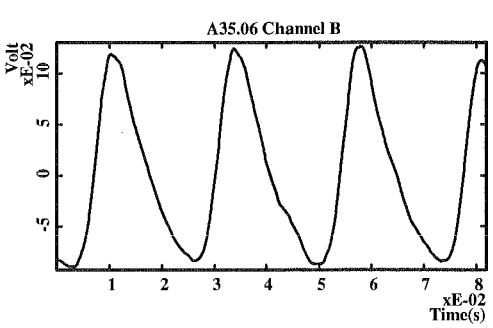
A35.06 Channel B
Volt
xE-02
xE-02
Time(s)

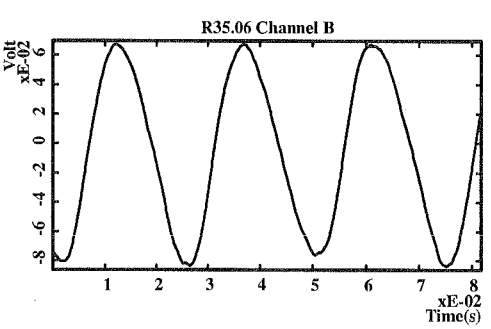
R35.06 Channel B
Volt
xE-02
xE-02
Time(s)

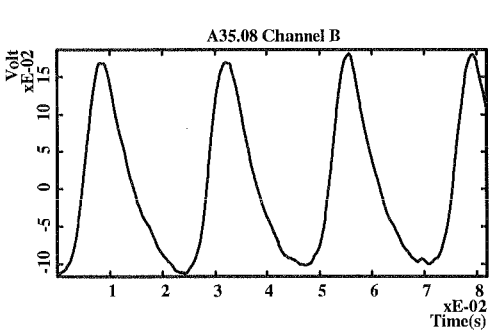
A35.08 Channel B
Volt
xE-02
xE-02
Time(s)

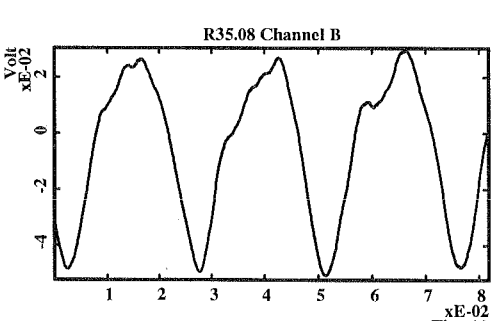
R35.08 Channel B
Volt
xE-02
xE-02
Time(s)

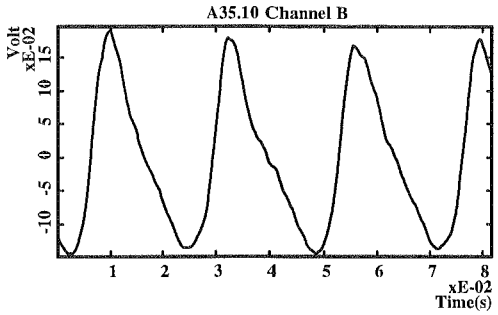
A35.10 Channel B
Volt
xE-02
xE-02
Time(s)

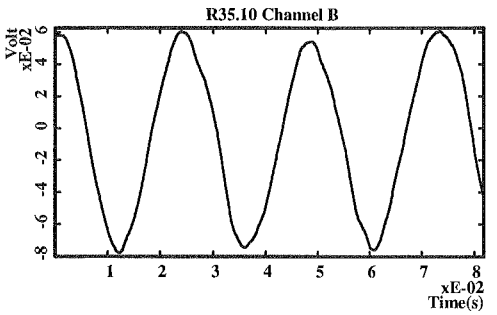
R35.10 Channel B
Volt
xE-02
xE-02
Time(s)

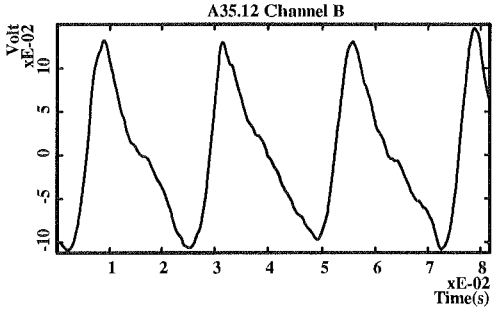
A35.12 Channel B
Volt
xE-02
xE-02
Time(s)

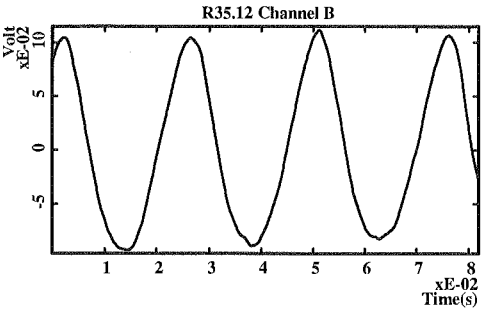
R35.12 Channel B
Volt
xE-02
xE-02
Time(s)

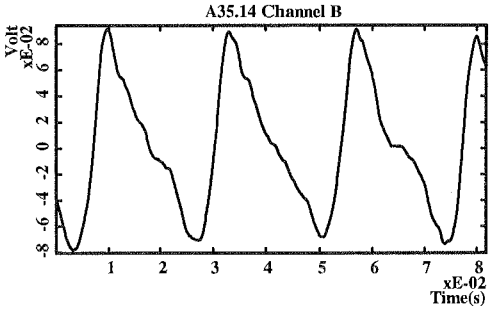
A35.14 Channel B
Volt
xE-02
xE-02
Time(s)

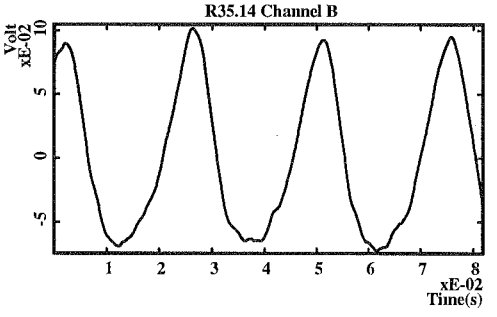
R35.14 Channel B
Volt
xE-02
xE-02
Time(s)

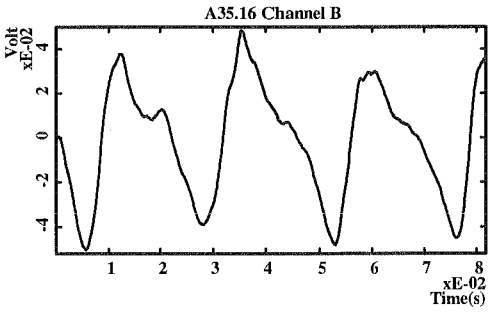
A35.16 Channel B
Volt
xE-02
xE-02
Time(s)

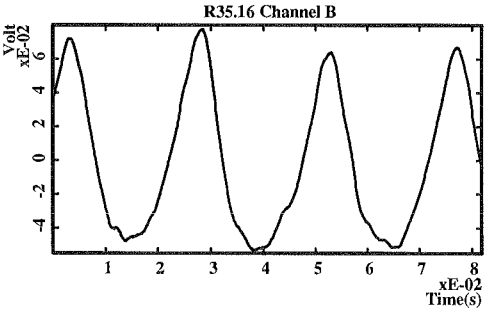
R35.16 Channel B
Volt
xE-02
xE-02
Time(s)

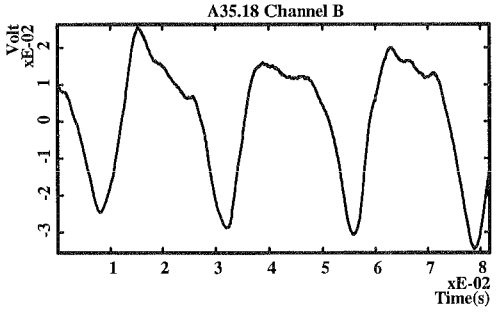
A35.18 Channel B
Volt
xE-02
xE-02
Time(s)

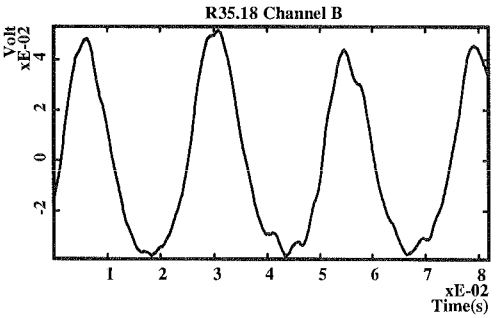
R35.18 Channel B
Volt
xE-02
xE-02
Time(s)

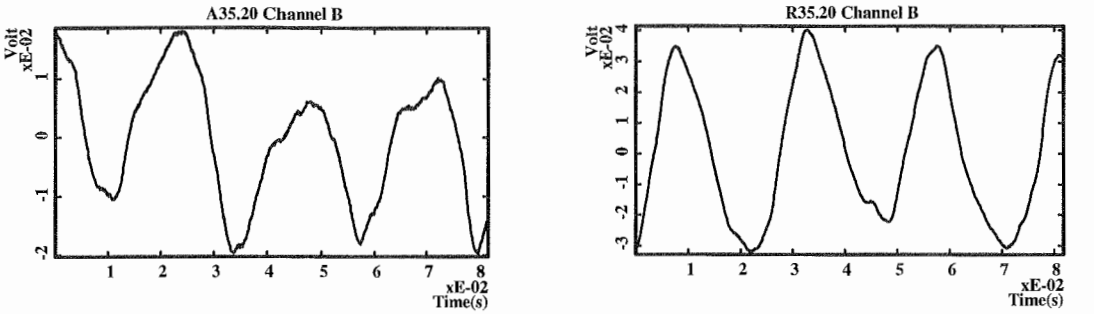

Figure 2.6 Time averaged deflection signal records extracted from the schlieren record output signal by signal recovery methods (excitation frequency = 40 Hz, X = 35 mm, X/d = 5.83, 1 volt = 213.7 radians).

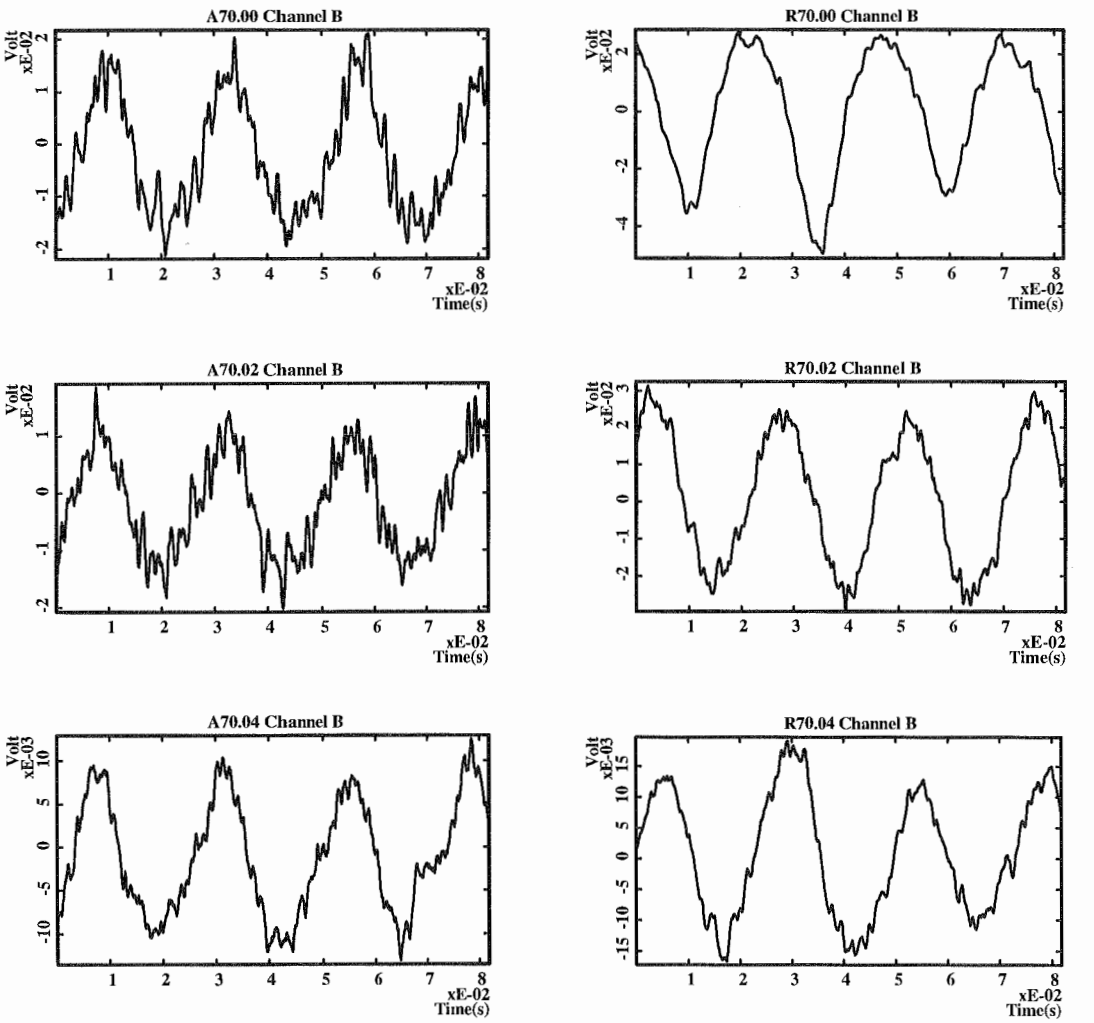

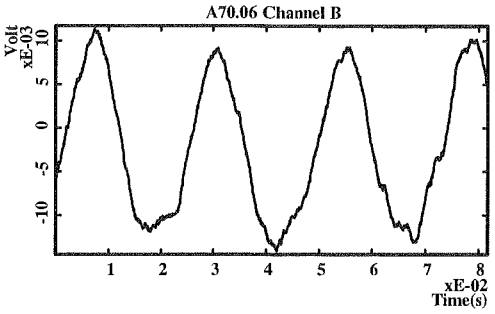
A70.06 Channel B
Volt
xE-03
xE-02
Time(s)

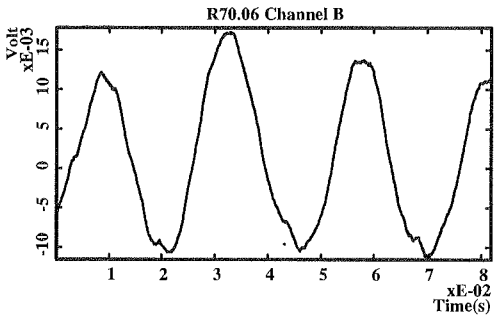
R70.06 Channel B
Volt
xE-03
xE-02
Time(s)

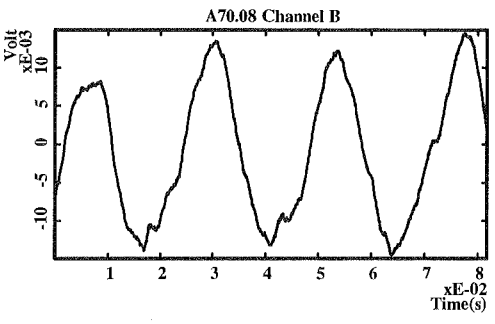
A70.08 Channel B
Volt
xE-03
xE-02
Time(s)

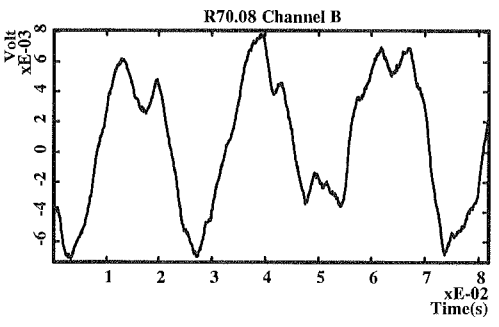
R70.08 Channel B
Volt
xE-03
xE-02
Time(s)

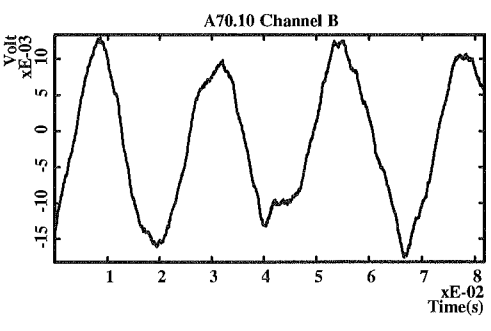
A70.10 Channel B
Volt
xE-03
xE-02
Time(s)

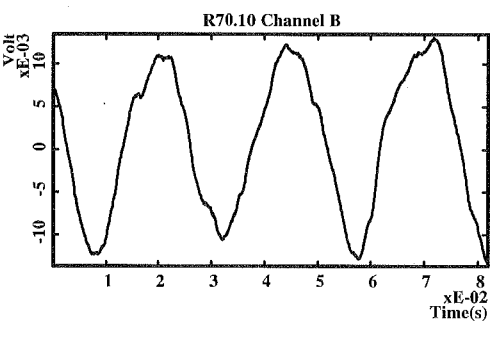
R70.10 Channel B
Volt
xE-03
xE-02
Time(s)

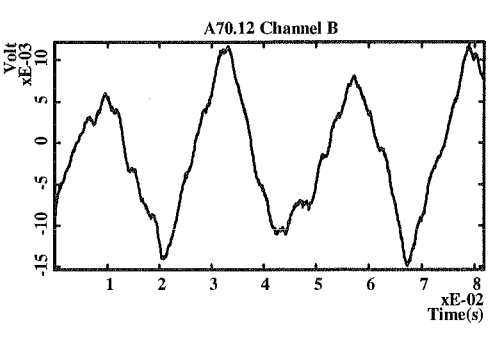
A70.12 Channel B
Volt
xE-03
xE-02
Time(s)

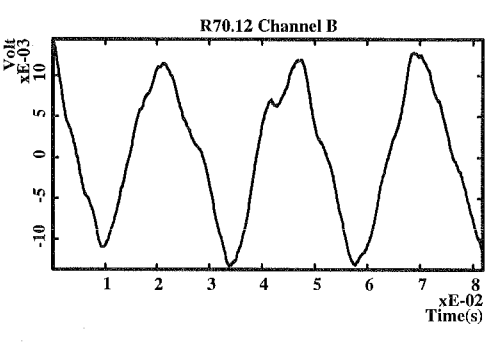
R70.12 Channel B
Volt
xE-03
xE-02
Time(s)

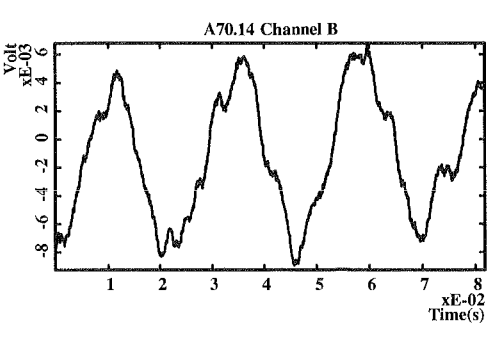
A70.14 Channel B
Volt
xE-03
xE-02
Time(s)

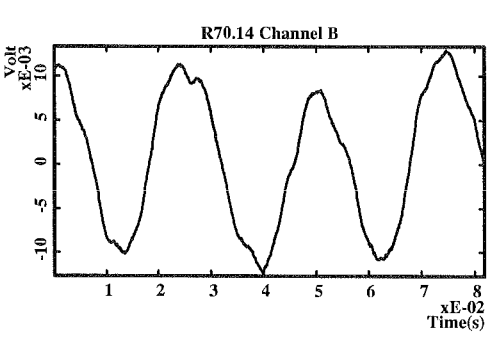
R70.14 Channel B
Volt
xE-03
xE-02
Time(s)

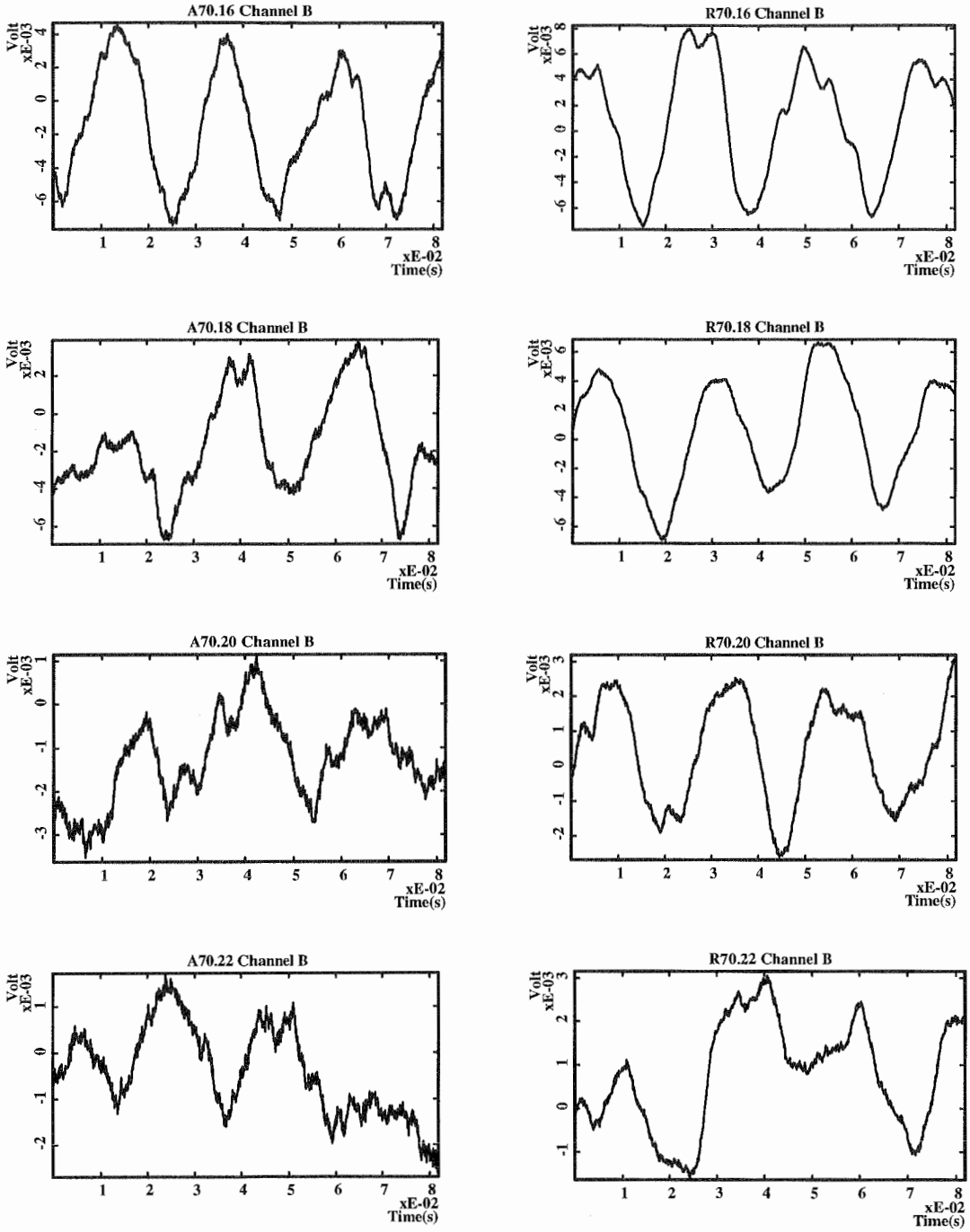

Figure 2.7 Time averaged deflection signal records extracted from the schlieren record output signal by signal recovery methods (excitation frequency = 40 Hz, X = 70 mm, X/d = 11.67, 1 volt = 213.7 radians).

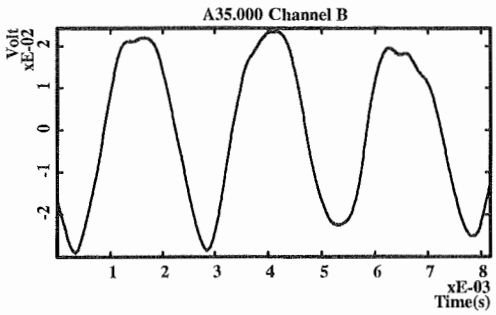
A35.000 Channel B
Volt
xE-02
xE-03
Time(s)

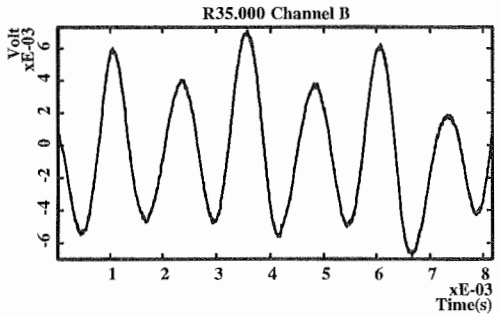
R35.000 Channel B
Volt
xE-03
xE-03
Time(s)

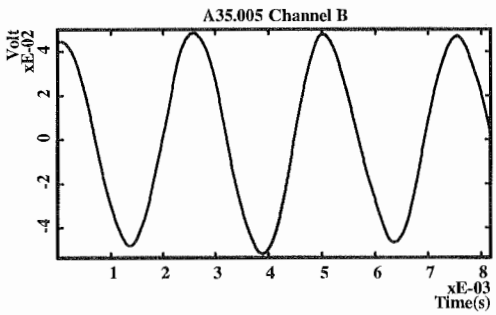
A35.005 Channel B
Volt
xE-02
xE-03
Time(s)

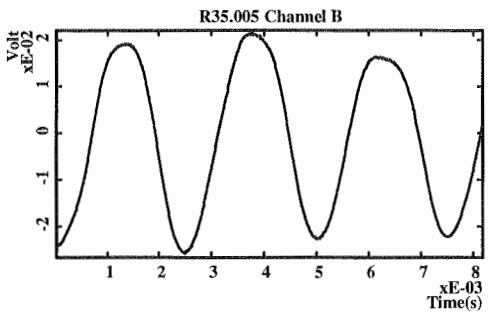
R35.005 Channel B
Volt
xE-02
xE-03
Time(s)

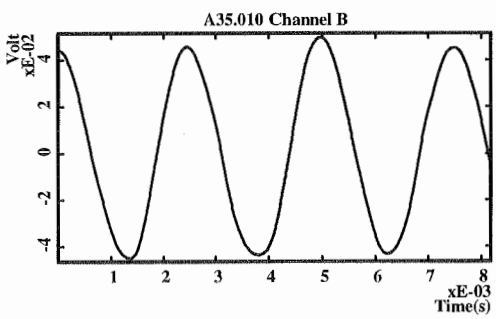
A35.010 Channel B
Volt
xE-02
xE-03
Time(s)

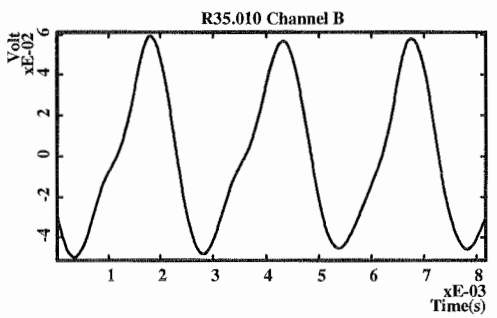
R35.010 Channel B
Volt
xE-02
xE-03
Time(s)

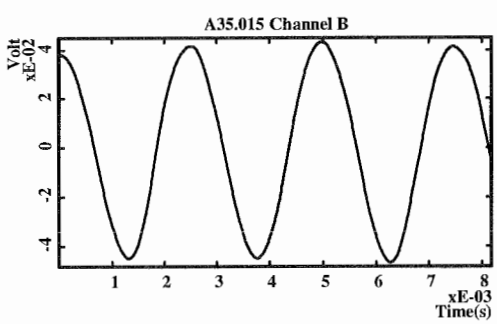
A35.015 Channel B
Volt
xE-02
xE-03
Time(s)

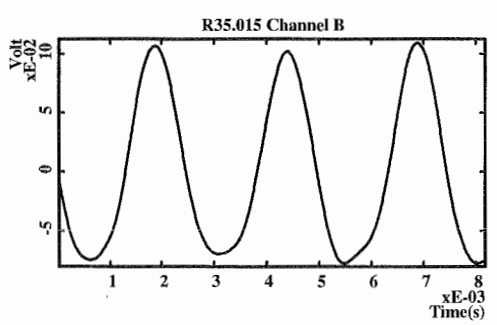
R35.015 Channel B
Volt
xE-02
xE-03
Time(s)

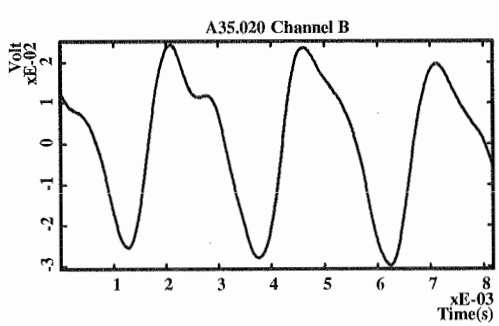
A35.020 Channel B
Volt
xE-02
xE-03
Time(s)

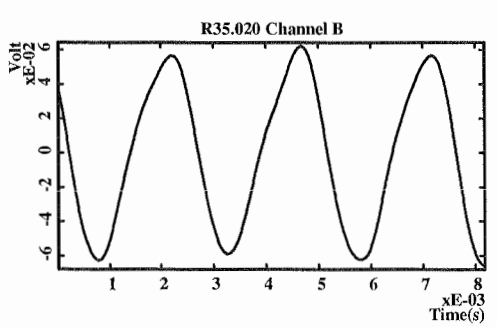
R35.020 Channel B
Volt
xE-02
xE-03
Time(s)

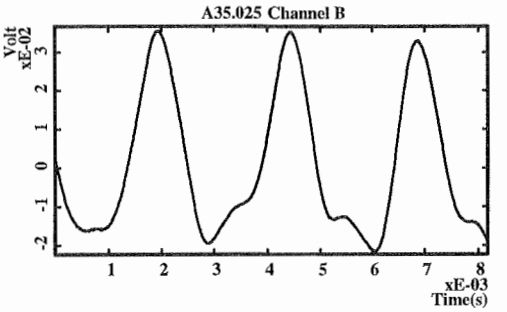
A35.025 Channel B
Volt
xE-02
xE-03
Time(s)

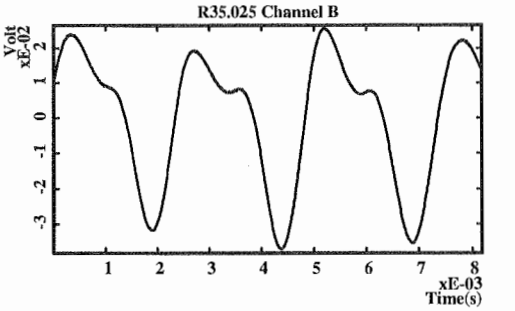
R35.025 Channel B
Volt
xE-02
xE-03
Time(s)

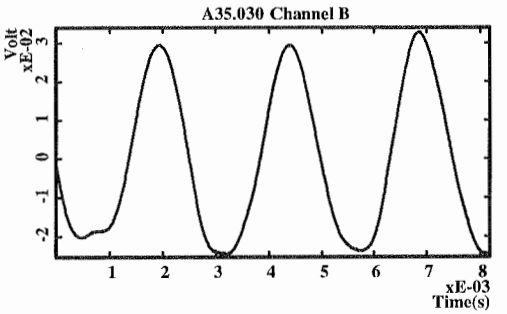
A35.030 Channel B
Volt
xE-02
xE-03
Time(s)

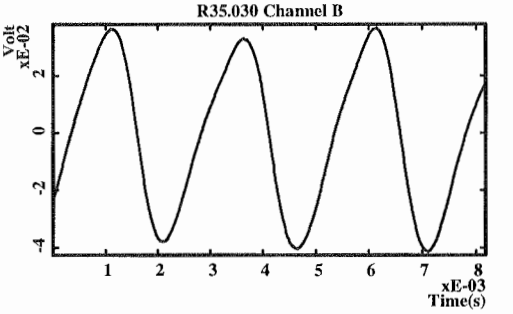
R35.030 Channel B
Volt
xE-02
xE-03
Time(s)

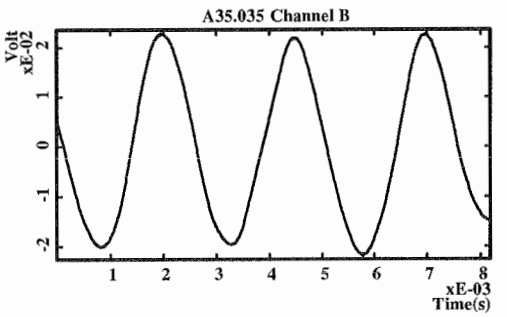
A35.035 Channel B
Volt
xE-02
xE-03
Time(s)

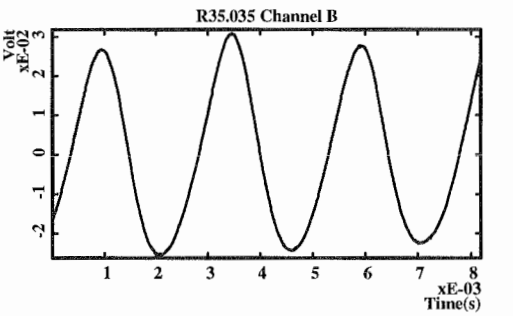
R35.035 Channel B
Volt
xE-02
xE-03
Time(s)

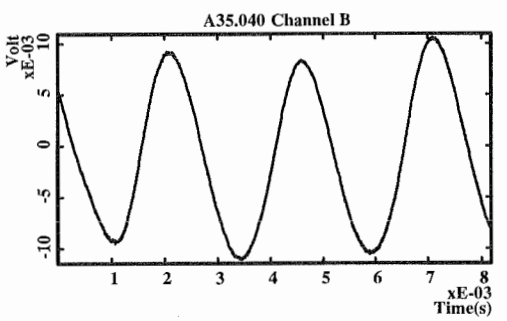
A35.040 Channel B
Volt
xE-03
xE-03
Time(s)

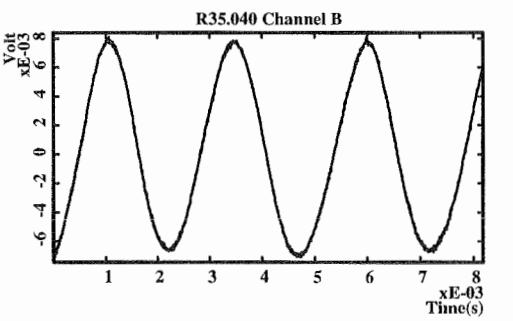
R35.040 Channel B
Volt
xE-03
xE-03
Time(s)

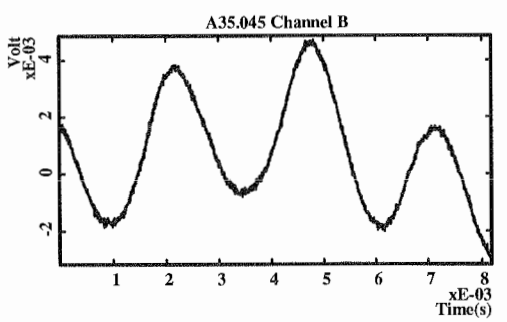
A35.045 Channel B
Volt
xE-03
xE-03
Time(s)

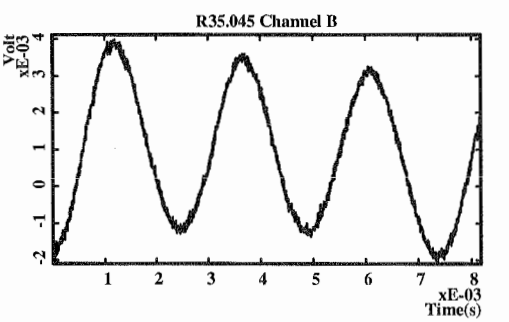
R35.045 Channel B
Volt
xE-03
xE-03
Time(s)

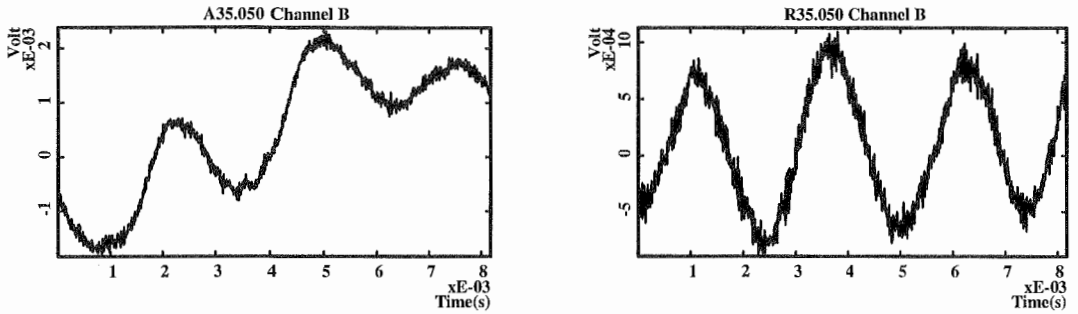

Figure 2.8 Time averaged deflection signal records extracted from the schlieren record output signal by signal recovery methods (excitation frequency = 420 Hz, X = 35 mm, X/d = 5.83, 1 volt = 213.7 radians).

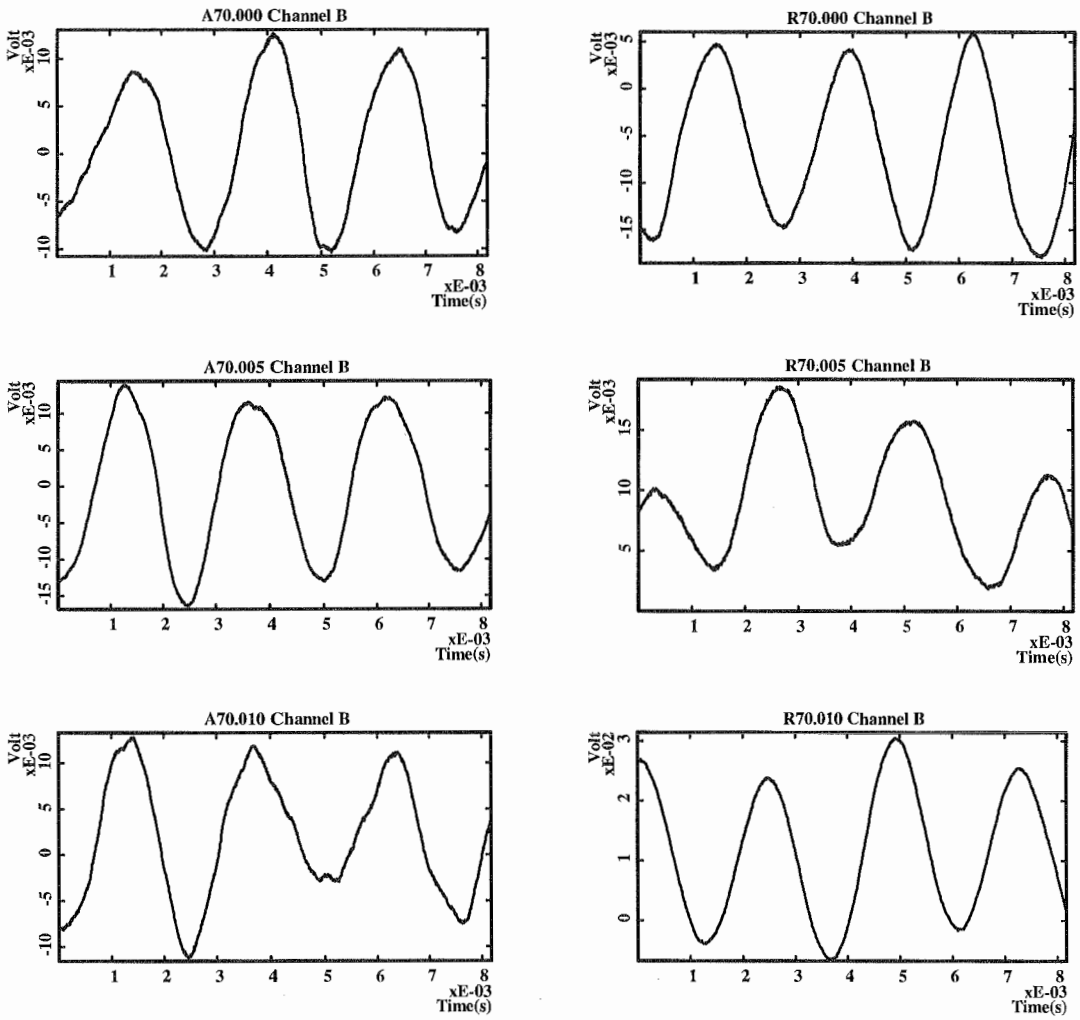

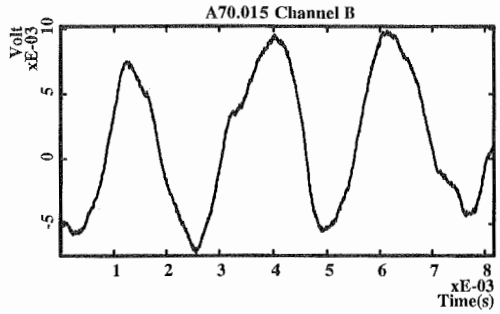
A70.015 Channel B
Volt
xE-03
xE-03
Time(s)

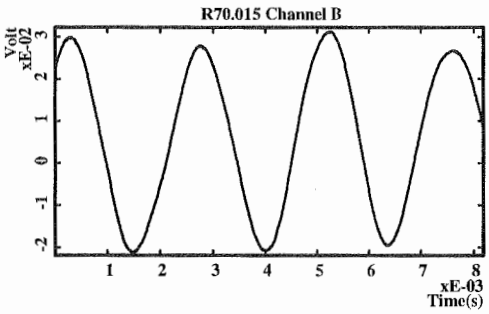
R70.015 Channel B
Volt
xE-02
xE-03
Time(s)

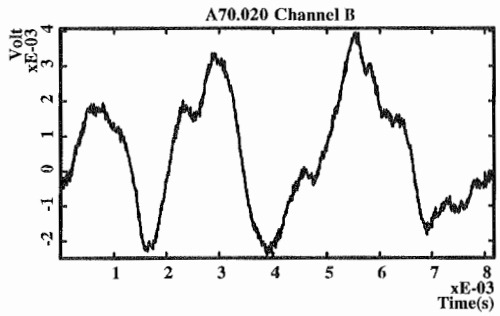
A70.020 Channel B
Volt
xE-03
xE-03
Time(s)

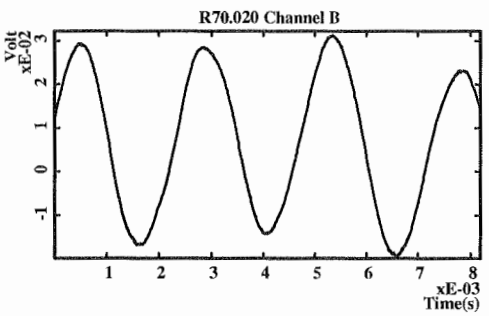
R70.020 Channel B
Volt
xE-02
xE-03
Time(s)

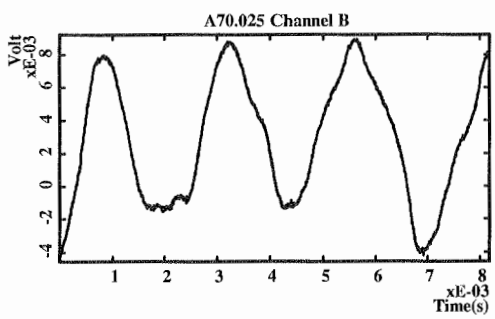
A70.025 Channel B
Volt
xE-03
xE-03
Time(s)

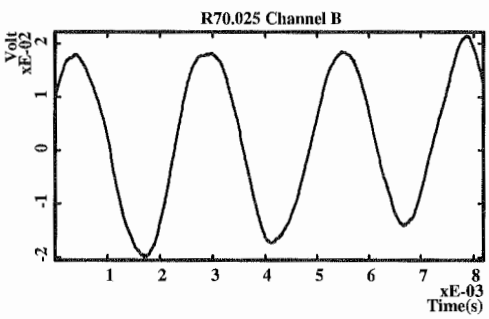
R70.025 Channel B
Volt
xE-02
xE-03
Time(s)

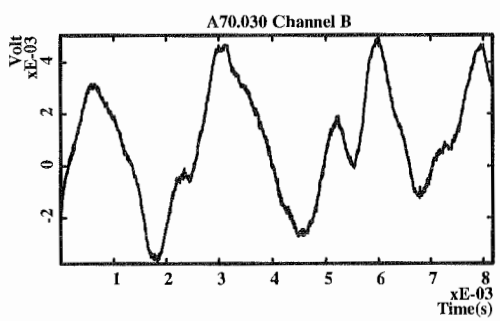
A70.030 Channel B
Volt
xE-03
xE-03
Time(s)

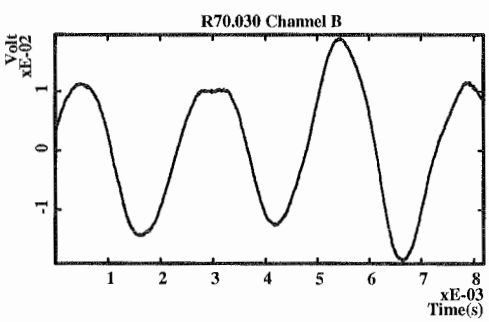
R70.030 Channel B
Volt
xE-02
xE-03
Time(s)

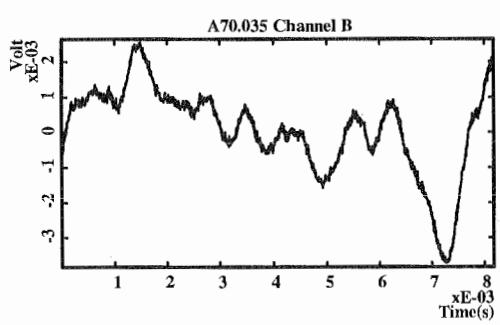
A70.035 Channel B
Volt
xE-03
xE-03
Time(s)

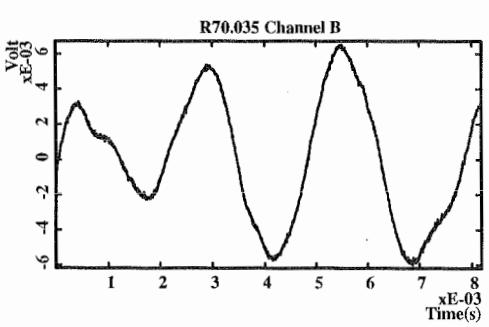
R70.035 Channel B
Volt
xE-03
xE-03
Time(s)

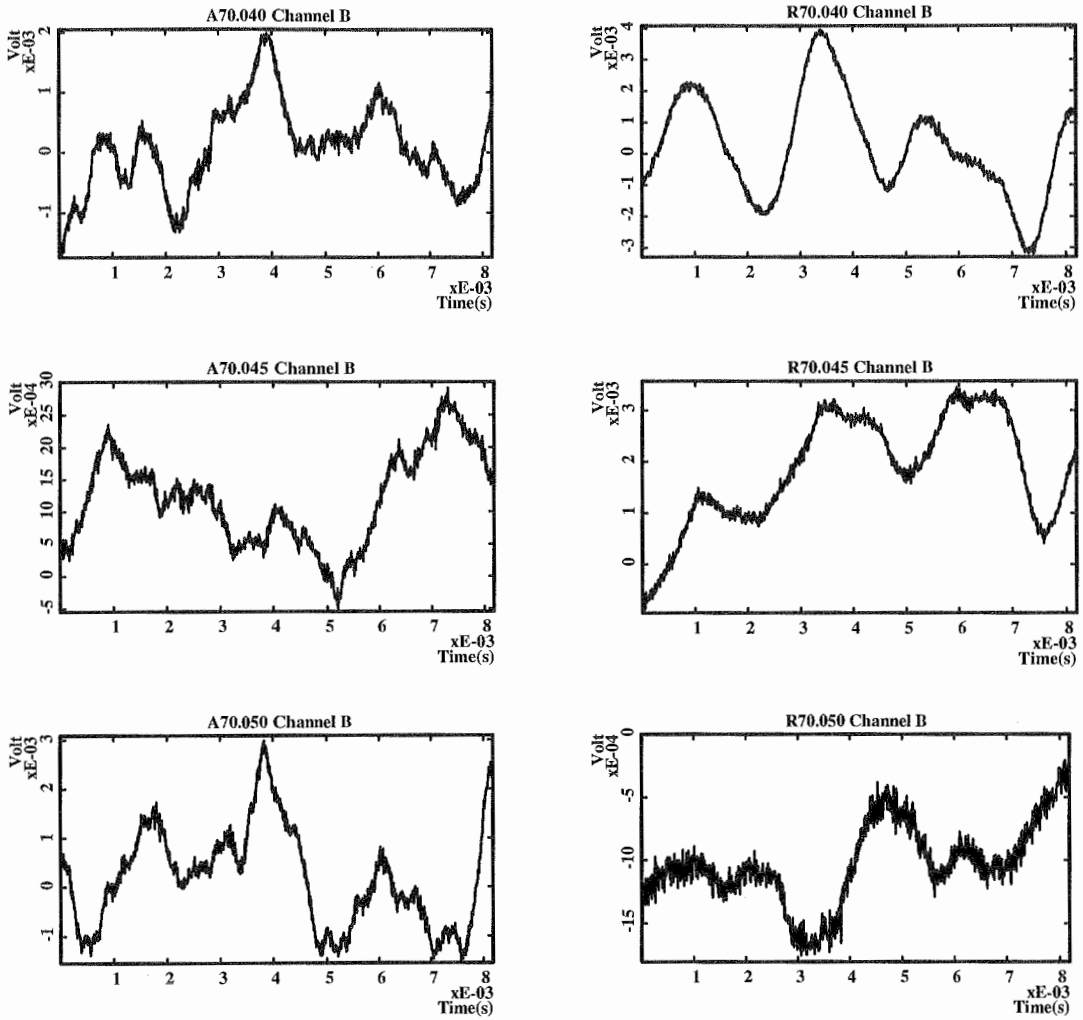

Figure 2.9 Time averaged deflection signal records extracted from the schlieren record output signal by signal recovery methods (excitation frequency = 420 Hz, X = 70 mm, X/d = 11.67, 1 volt = 213.7 radians).

2.3 The measurement of experimental parameters

2.3.1 Calibration of absolute refractivity values

The fluctuating voltage output from the detector is linearly proportional to the fluctuating movement of the detecting beam. In other words, the voltage response of the detector is a function of the light beam spot deflection from its centre or null position. The instantaneous value of the total beam deflection angle might thus be calculated from the beam point deflection at the photo diode and the distance from the photo diode to the flow field. One source of error in the experiment is due to the uncertainty in determining the location of the effective deflection point (in other words the determination of L) in the flow from which the angular deflection is measured. Because L is uncertain, in practice, a constant value of $L = L_0$ is assumed in calculating the results. A slight error is thus introduced in relating the detector output to the beam deflection in the experiment. But the relative error in the angular deflection calculation is of magnitude $(L - L_0)/L_0$. It is obvious that a large value of L_0 will reduce the error. However, a large value of L_0 is accompanied by large linear deflection at the photodetector with a corresponding increase in error due to the increased deviation from linearity of the detector. Thus for any given situation, there exists an optimum value of L_0 for which the total error is minimum.

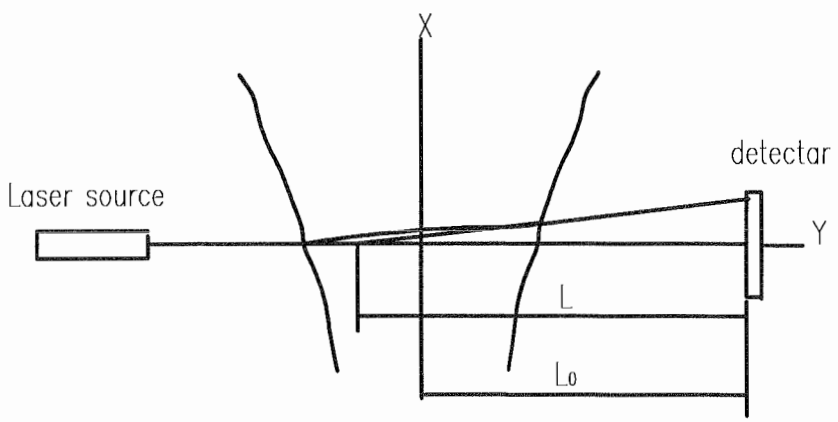

Figure 2.10 Beam deflection by refractivity field.

According to Winarto (1979), the maximum value of fluctuating angular deflection would be approximately an order of 10^{-3} gradient which corresponds to a linear beam spot deflection on the detector of 10^{-3}m or 1 mm. The distance L_0=1.2 m used

in the present work is thus seen to be appropriate to the linear region of the sensors used and the error is found to be less than 2.5% in this experiment (Figure 2.10). The variation in the length L from L0 is approximately ± 25 mm, that is also a ± 2.0 % variation, which is closely comparable in magnitude with the detector nonlinearity)

The expression for the output voltage is:

$$V(z,t) = L.S.G.\theta(z,t) \qquad (2.3.1)$$

where

$V(z, t)$ = instantaneous fluctuation signal (voltage) at input to Nicolet 660B signal analyser.

L = 1.2 m...distance from the deflection point to the detector diode

S = 17.81 (mv/mm).....sensitivity of the detector

G = 10 ... the gain of amplifier

t = time(s)

z = distance from centre position to light point on detector (mm)

θ = angle of deflection (radians)

Thus we have

$$\theta(z,t) = \frac{V(z,t)}{17.81 \times 10 \times 1.2}(\text{radians}) = \frac{V(z,t)}{213.72}(\text{radians}) \qquad (2.3.2)$$

By this transformation, the output voltages can be converted into angles of deflection.

2.3.2 Calibration of sound pressure levels (SPL)

The overall sound pressure level is a good indicator of the excitation level, which relates the excitation strength to the flow characteristics. The background ambient sound pressure level (SPL) was maintained below 57 dB throughout the experiments. The SPL was calibrated using a B & K Sound Level Meter (Type 2230), which has a 10 Hz -50 kHz bandwidth and 24 dB - 133 dB measuring range. The resolution is 0.1 dB. The microphone detector has a 2 cm distance to the

nozzle. *Leq* is used in the experiment, which is the sound pressure level averaged over the measurement period. It can be considered as the continuous steady sound pressure level which would have the same total acoustic energy as the real fluctuating noise over the same time period. The measurement of *Leq* is based on the equal energy principle:

$$L_{eq} = 10 log_{10} \frac{1}{T} \int_0^T \left(\frac{P(t)}{P_0} \right)^2 dt \qquad (2.3.3)$$

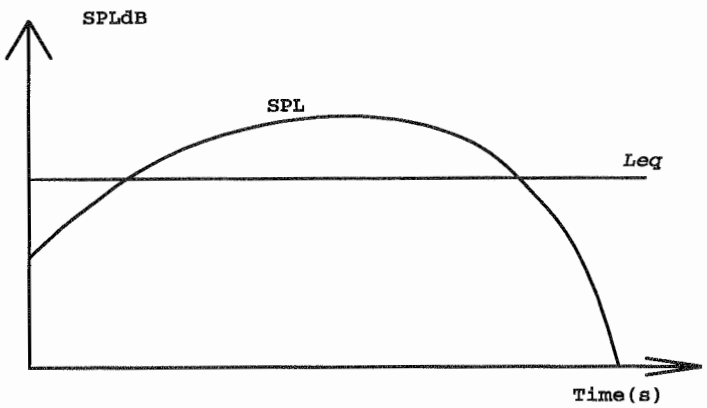

Figure 2.11 The relationship between *SPL* and time.

The *SPL* in the experiment was generated by the background noise (SPL_b) and the excitation signal (SPL_e). The SPL_b can be taken as constant in the experiments. However, the SPL_e varied as excitation strength and frequency varied. The relationship between excitation strength and *SPL* has been recorded separately at volt excitation frequencies 40 Hz and 420 Hz. The calibration results are shown in Figures 2.12 and 2.13, which show the relationship between the SPL and excitation strength. The higher frequency of excitation generates a stronger SPL than the low frequency at the same input excitation voltage level. Both curves have a region of linear increase, above which the SPL increases more slowly despite the excitation level rapidly increasing. The experiment excitation strengths and SPL levels are described below, when the filtered levels are recorded for the octave band containing the excitation signal. The general background noise is predominantly low frequency in nature mainly originating in the exhaust extractor fan system. The background noise level is obtained without extractor and combustion operating. The levels with flame have the combustion operating, whilst those with extractor fan have only the

fan operating. The total level has the diffusion flame operating with excitation applied.

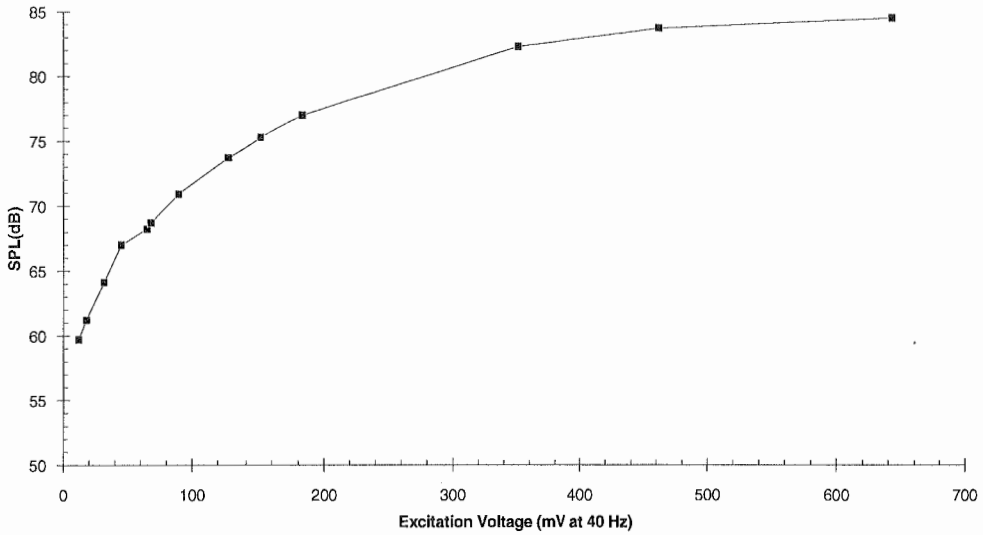

Figure 2.12 The SPL Calibration (using 40 Hz filter and exhaust fan off).

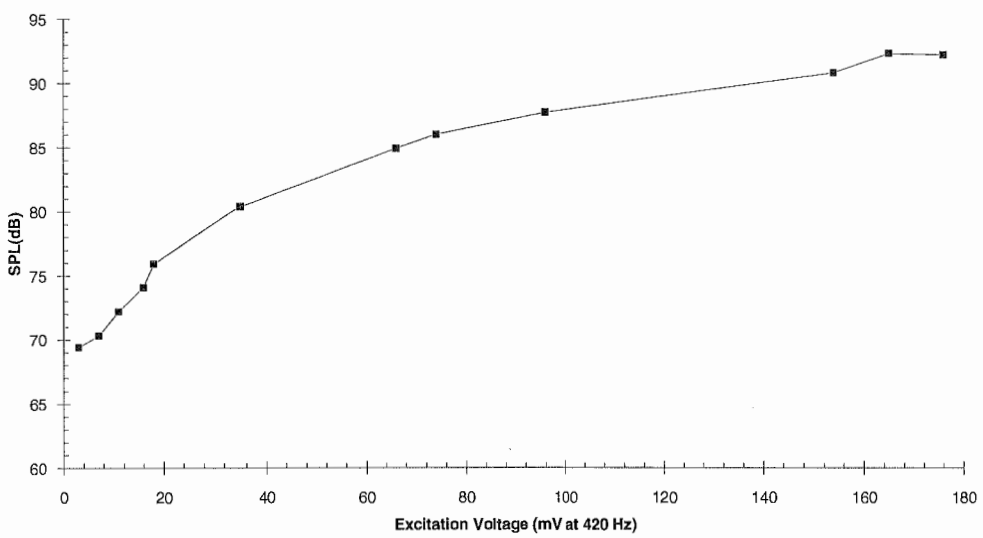

Figure 2.13 The SPL Calibration (using 420 Hz filter and exhaust fan off).

A. The SPL at the lower frequency excitation (files A35.xx, R35.xx, A70.xx & R70.xx): The excitation input signal is 0.012 V (at 40 Hz)

Table 2.3.1 The calibration of SPL (40 Hz).

SPL	Filtered levels(40 Hz)	Unfiltered levels
SPL (Background)	56.8 dB	64.0 dB
SPL (With flame on)	57.0 dB	69.0 dB
SPL (With extractor fan on)	61.8 dB	82.4 dB
SPL (Total)	61.0 dB	83.5 dB

Because the difference between SPL (Total) and SPL (With flame on) is only 4 dB, at 40 Hz excitation, a correction is necessary to determine the excitation component. That is

$$SPL(Ex) = SPL(Total) - \Delta L_n \qquad (2.3.4)$$

ΔL_n is 2.2 dB (ΔL_n was obtained from the appendant form of B&K Sound Level Meter use manual), and thus the SPL due to the excitation at 40 Hz is:

$$SPL(Ex) = 61 \text{ dB} - 2.2 \text{ dB} = 58.8 \text{ dB} \qquad (2.3.5)$$

B. The SPL at higher frequency excitation (files A35.xxx, R35.xxx, A70.xxx & R70.xxx): The excitation input signal is 0.045 V (at 420 Hz)

Table 2.3.2 The calibration of SPL (420 Hz).

SPL	Filtered levels(400 Hz)	Unfiltered levels
SPL (Background)	53.0 dB	64.0 dB
SPL (With flame on)	58.0 dB	69.2 dB
SPL (With extractor fan on)	77.5 dB	82.4 dB
SPL (Total)	82.0 dB	82.4 dB

Due to the substantial difference of 24 dB existing between SPL (Total) and SPL (With flame on). The SPL of excitation in effectively nearly equals SPL (Total).

2.3.4 Measurement of the convection velocity of the disturbances

In order to carry out the transformation from a set of values which are functions of time to values which are functions of axial displacement, it is necessary to know the convection velocity (V_c) of the turbulent flame. According to Taylor's "frozen turbulence" hypothesis, the turbulent flow is pictured as being composed of contiguous eddies acted on by the mean flow with a convection velocity of V_c. Within the time and length scales under consideration, the convection velocity is assumed constant and the eddies frozen, i.e. the flow field remains exactly the same at different times, except for a shift in the downstream direction. Based on this hypothesis, the convection velocity can be obtained by the space-time cross-correlation of the crossed-beam system which uses a second laser beam located orthogonally to the first but displaced in an axial direction by changing distances. Assuming the first beam is fixed in space and located at (x, y, z+ζ), and the second beam is traversed in the axial or ξ-direction and is located at (x+ξ, y+η, z). Then the first detector signal output is

$$\theta_\eta(x,z,t)=\int_{-\infty}^{\infty}\frac{\partial n(x,y+\eta,z,t)}{\partial\xi}d\eta \qquad (2.3.1)$$

and the deflection of the second beam is

$$\theta_\eta(x+\xi,y,t)=\int_{-\infty}^{\infty}\frac{\partial n(x+\xi,y,z+\zeta,t)}{\partial\xi}d\zeta \qquad (2.3.2)$$

From equations 2.3.1 and 2.3.2, we have the space-time cross-correlation of the two signals:

$$\overline{\theta_\eta(x,z,t)\theta_\zeta(x+\xi,y,t+\tau)}=\overline{\int_{-\infty}^{\infty}\frac{\partial n(x,y+\eta,z,t)}{\partial\xi}d\eta\int_{-\infty}^{\infty}\frac{\partial n(x+\xi,y,z+\zeta,t+\tau)}{\partial\xi}d\zeta} \qquad (2.3.3)$$

As can be seen from the above equations, the output signal of the second beam detection system is time delayed by an amount τ. Observation of the time delay of peak cross correlation (t) between the two beams thus indicates convection velocity

of the structures in the flow. When the two beams are at the same axial location, the peak of cross correlation will appear at the zero time delay point. If the distance (X) between two vertical beams is changed, the time delay (τ) will be changed as well. The convective velocity V_c can be obtained from flow equation:

$$\overline{V}_c = X/\tau_{max} \qquad (2.3.4)$$

where τ_{max} is peak time delay (Figure 2.14).

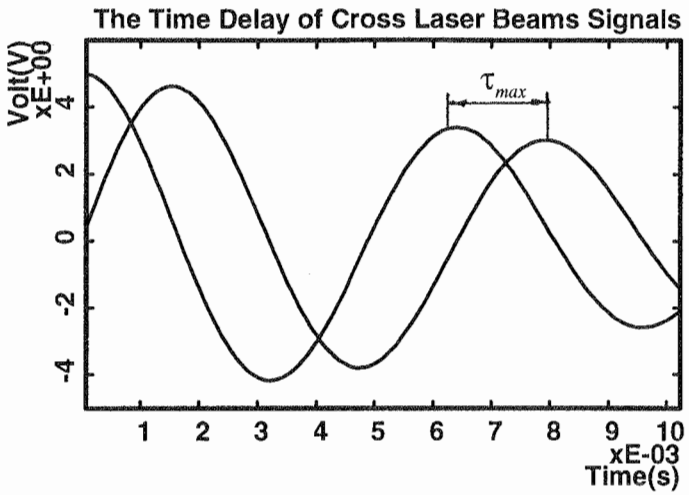

Figure 2.14 The cross laser beams signals.

As shown in Figure 2.15, the slope of these results gives a velocity of 2.07 m/s for the low frequency (40 Hz) structures and 2.7 m/s for the high frequency (420 Hz) structures. It is noted that the latter value is slightly higher than the nominal exit velocity of the central gas nozzle flow. The first reason for this may be the accuracy of the measurement. The laser light beam is 0.8 mm thick, but the spatial wavelength is about 52 mm for the 40 Hz excitation and 6.5 mm for the 420 Hz. This causes poor resolution of measurements at high frequency which also may affect the overall distribution results of refractive index of the diffusion flame as discussed later on. The second reason (probably the most important) is that the eddies are not frozen in a real turbulent flame. In fact they interact with each other and are stretched and distorted as they are being converted. This is reflected in the fact that the maximum value of the space-time covariance is dependent on the beam separation distance ξ, and furthermore the shape of the space-time covariance curve varies as ξ is varied (Figure 2.3.1). Since eddies are stretched and distorted, one can speak of an eddy life time, i.e. an interval of time during which the eddy may be

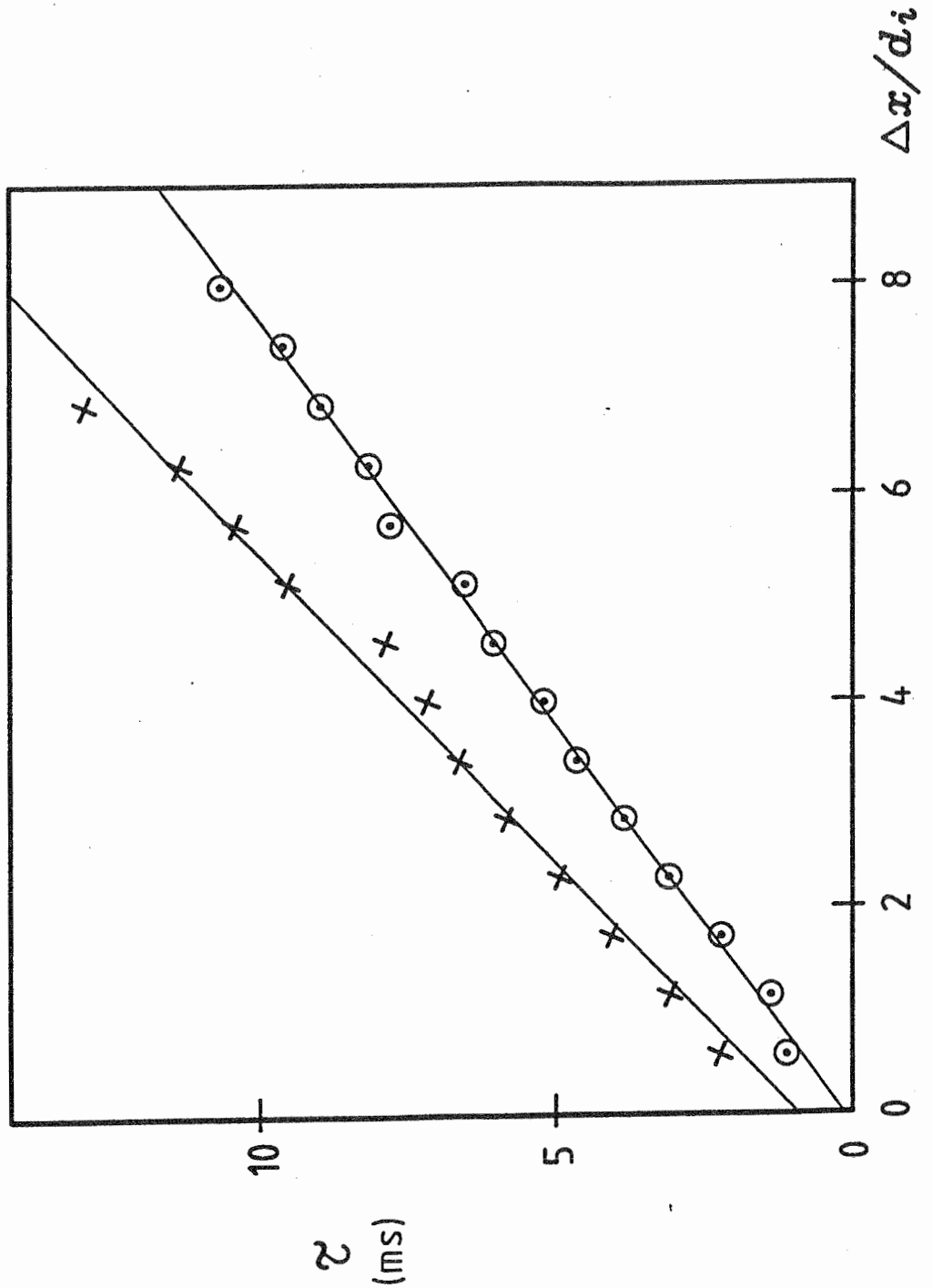

Figure 2.15 Convective motion of mixing structures as shown by time delay to peak correlation.
×: 40 Hz, slope = 2.07 m/s. ⊕: 420 Hz, slope = 2.7 m/s.

thought of as having a distinct identity, and during this period Taylor's frozen turbulence hypothesis is valid (see Tennekes and Lumley, 1972). Because the eddy life time is very short at high frequency compared to at low frequency, it is understandable that V_c is less accurate at high frequency than at low frequency.

2.4 Total image acquisition and fractal analysis

Flow visualisation is generally utilised in conjunction with quantitative measurements when studying complex fluid dynamic phenomena. A primary advantage of flow visualisation is rapid and usually simple acquisition of instantaneous and spatially dense, though usually provides excellent guidance for subsequent quantitative measurements of the flow. Given the large amount of information in a single photograph, it is not surprising that flow visualisation led to the discovery and conceptual formulation of the nature of large coherent structures in turbulent shear flows (Brown and Roshko, 1974). The concept of large scale structures in turbulent flow would have been quite difficult and time-consuming to develop on the basis of hot-wire anemometry, pressure measurements, or even laser Doppler velocimetry, since these methods only provide information about the temporal evolution of the flow at a limited number of spatial locations. Image-processing techniques appear to represent the next generation of measurements by combining the spatial presentation of flow visualisation with quantitative methods of data acquisition and by deducing velocity and other information directly from the optical images. Examples of such methods are found in water experiments where optically activated tracers are photographed over short time intervals. The resulting trajectories can then be converted digitally into the velocity vector field (Gharib, 1986).

The most common method of flow visualisation is the introduction of tracers, dye or smoke, into the flow at one or more points. Whenever the fluid considered has a density inhomogeneity, optical methods such as shadowgraph and schlieren, can be used to establish the location of the boundary of the inhomogeneity. Shadowgraph and schlieren techniques are most sensitive to gradients in the index of refraction which vary directly with the density, and schlieren images are sensitive to the first spatial derivative of the density (Merzkirch, 1987). When a shear flow consists of two fluids of different density, such as a helium jet in air or a hot jet in a cold

environment, the interface between the two fluids is clearly visible with an optical technique such as schlieren or shadowgraph. A schlieren picture integrates along the light rays and produces a 2-D projection of the interface between the two fluids. The interpretation of tracer or schlieren images in 3-D time dependent flows is not straightforward. For example, a harmonically perturbed plane shear layer produces streaklines that roll into an array of discrete eddies, giving the impression of wave breakdown, even though the flow may constitute a linear superposition of a weak harmonic motion with a steady velocity profile (Hama, 1962). Irrespective of the three-dimensionality of the turbulent motion, the free interface apparent in a schlieren image of a flow with Schmidt number (or Prandtl number in the case of temperature inhomogeneities) of approximately unity corresponds to the vorticity boundary, i.e. the interface between turbulent and potential flow.

The equipment used for studying the fractal dimension of the diffusion flame in the second part of this investigation consists of the same flame combustor system and an image capture system. The flame combustor system is the same as in the first experiment. In order to obtain a variety of flame images, several different flow conditions of the diffusion flame were used. The flame image capturing system is called *PIP image acquisition and processing system.* The measuring system was combined with an incandescent source lamp and slit, two mirrors, a knife edge, a high speed video camera, a stepper motor, a monochrome video monitor and a HP286 computer (see Figure 2.16). A PIP-MATROX 1024B frame grabber board is installed in the computer to run the software *PIP image acquisition and processing software package*, abbreviated *PIP*, which was written by Jumppanen (Department of Civil & Mechanical Engineering, University of Tasmania, 1993). The *PIP* program was written in 'Borland C++ ' and assembly language. It is a DOS based menu driven program with multiple functions such as image capture, file save and load, set image area, image processing, knife-edge adjustment (by stepper motor control) and light intensity calibration, image display and print, and fractal dimension calculation (for more detail see *PIP* operation manual, Jumppanen, 1993).

In the experimental configuration, the mirrors used were 7.2 inch (184 mm) diameter with a focal length of 60 inch (1524 mm) and were spaced 5.5 m apart. Light from the source was focused by a collimator lens on a 2 mm gap collimating slit. The knife edge, which is controlled by computer through the stepper motor, at the focal point of the second schlieren mirror was used to partially cut off the deflected rays.

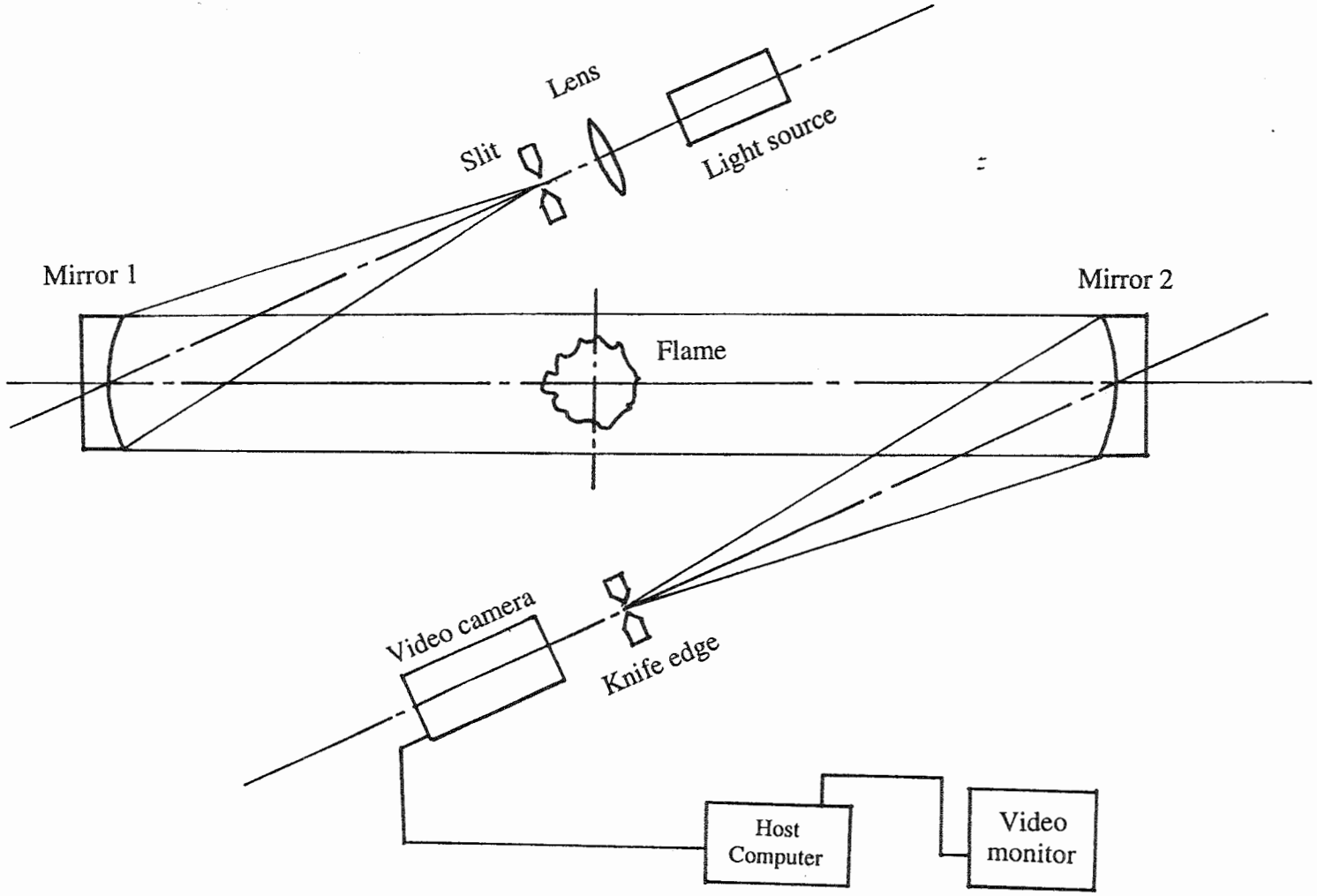

Figure 2.16 The image acquisition system as applied to the diffusion flame image.

During the experiment, light provided by the lamp, which is situated behind knife edge 1, was reflected by mirror 1 and passed through the flame. The second mirror reflected the image light to a video camera situated behind the knife edge. The schlieren images were captured electronically. The camera speed was set between 1/1000~1/2000 sec. For 2.5 m/s fuel flow, this gives a 1.3~2.5 mm resolution. The motorised knife edge, controlled by computer through the stepper motor, could be moved vertically to get an optional contrast image with a uniform mean light level as the whole field of view to ensure that situation (full light or 255 light level) did not occur.

Frame grabbing and subsequent digitisation of the diffusion flame image gives some advantages not available to other forms of pictorial storing of an image. It allows linearisation for the camera response, coordinate transformation as well as conventional image processing techniques such as contrast enhancement, convolution filtering, edge detection, pseudo colouring, image averaging, subtraction, addition, as well as many specialised processes. This allows many image artefacts to be enhanced and thus raised out of the general random appearance of an initial image. It is a very valuable technique for studying fluid flow situations.

Each flow image is recorded and stored in digital format for later analysis. Distortion and background noise due to illumination and the camera system is calibrated by *PIP* software. For the purpose of comparison of flame images and other images, there are four other images of leaves are recorded in the experiment. Those pictures are captured using a Nikon zoom lens in front of the camera. All images are shown in Figure 4.6.

2.5 Digital image enhancement

The original images of the turbulent flames taken by *PIP* image acquisition system contains information relating to the flame structure due to light passing through the flame. Each element of the image is the light intensity which corresponds to the local deflection angle of the light. The schlieren technique uses the change of refractive index caused by thermal and/or density gradients to deflect the probing light rays and thus form light and dark patterns which represent the large scale structures in the flame. In addition to the conventional schlieren technique, analysis of the detailed

information contained in the image by digital image processing is specially useful in extracting the patterns of the dynamic process. Some important signal image enhancement functions (e.g. Prewitt, Sobel, Laplacian, Horizontal and Vertical) in the *PIP* software can help to unveil the more detailed structure of a diffusion flame. The distinction between the digital image enhancement and digital image analysis is not immediately obvious, although it is an extremely important one. Image enhancement can be thought of as a transformation which transforms one image into another, i.e. it starts with an image and produces a modified (enhanced) image. On the other hand, digital image analysis is a transformation of an image into something other than an image, i.e. it produces some numerical information representing a description of the image field.

There are, broadly speaking, three distinct classes of enhancement operations: point operation, neighbourhood operation, and geometric operations. We are here only discussing the principle of the Prewitt operator (the images shown in Figure 2.4 are processed by the Prewitt Operator).

Differentiation is the most commonly used method of image enhancement and is based on evaluation of the gradient. Given an image function *f(x, y)*, the gradient of *f(x, y)* at coordinates *(x, y)* is defined as the vector

$$\mathbf{G}[f(x,y)] = \begin{bmatrix} G_x \\ \\ G_y \end{bmatrix} = \begin{bmatrix} \dfrac{\partial f}{\partial x} \\ \dfrac{\partial f}{\partial y} \end{bmatrix} \tag{2.5.1}$$

Two important properties of the gradient are: (1) the vector $\mathbf{G}[f(x,y)]$ points in the direction of the maximum rate of increase of the function *f(x, y)*; and given by

$$\alpha(x,y) = \tan^{-1}\left(G_x / G_y\right) \tag{2.5.2}$$

where the angle is measured with respect to the *x* axis (this is useful tool for linking edge points that have been detected by using the gradient).

(2) the magnitude of $\mathbf{G}[f(x,y)]$, denoted by $G[f(x,y)]$, and given by

$$G[f(x,y)] = \text{mag}(\mathbf{G}) = \left[(\partial f/\partial x)^2 + (\partial f/\partial y)^2\right]^{1/2} \qquad (2.5.3)$$

equals the maximum rate of increase of *f(x, y)* per unit distance in the direction of **G**.

X1	X2	X3
X4	X5	X6
X7	X8	X9

Figure 2.17 General 3 ×3 subimage region.

Equation (2.5.1) is the basis for a number of approaches to image differentiation. It is noted that this expression is in the form of a two-dimensional derivative function and that it is always positive. In practice, the scalar function $G[f(x,y)]$ is commonly referred as the gradient of *f*.

Note that from Equation (2.5.1) that computation of the gradient is based on obtaining the partial derivatives $\partial f/\partial x$ and $\partial f/\partial y$ at every pixel location. There are a number of ways to do this. One approach is using the first-order differences in a 3×3 neighbourhood about point (x, y) which can be formulated as follows. Consider the subimage area shown in Figure 2.17, let *w1, w2, ..., w9* represent the coefficients of the 3 × 3 mask shown in Figure 2.17, and let *x1, x2, ..., x9* represent the grey levels of pixel under the mask when the mask is in an arbitrary position in the image. The coefficients and corresponding grey levels can be expressed as column vectors; that is,

$$W = \begin{bmatrix} w_1 \\ w_2 \\ \cdot \\ \cdot \\ \cdot \\ w_9 \end{bmatrix} \tag{2.5.4}$$

and

$$X = \begin{bmatrix} x_1 \\ x_2 \\ \cdot \\ \cdot \\ \cdot \\ x_9 \end{bmatrix} \tag{2.5.5}$$

After convolving **W** and **X**, we have:

$$WX = w_1 x_1 + w_2 x_2 + \cdots + w_9 x_9 \tag{2.5.6}$$

The WX is general and applies to a mask of arbitrary size. For example, for an $n \times n$ mask, we would work with n^2 dimension vectors.

According to Equation (2.5.6), the component of the gradient vector in the x and y directions can be defined as

$$G_x = \boldsymbol{W}_1 \boldsymbol{X} \tag{2.5.7}$$

$$G_y = \boldsymbol{W}_2 \boldsymbol{X} \tag{2.5.8}$$

where $\boldsymbol{W}_1$ and $\boldsymbol{W}_2$ are the vectors containing the coefficients of the masks for the x and y directions, respectively. Then, the right side of Equation (2.5.3) can be expressed as the inner product of **W** and **X**:

$$G|f(x,y)| = \left|(W_1 X)^2 + (W_2 X)^2\right|^{1/2} \tag{2.5.9}$$

There two masks are commonly referred to as the Prewitt Operators in Figure 2.18. The responses of these two operators at any point (*x, y*) are combined using Equation (2.5.6) to obtain the gradient at that point. Convolving these masks with an image *f(x, y)* yields the gradient at all points in image, the result often being referred to as a gradient image.

$$\begin{vmatrix} -1 & -1 & -1 \\ 0 & 0 & 0 \\ 1 & 1 & 1 \end{vmatrix} \qquad \begin{vmatrix} -1 & 0 & 1 \\ -1 & 0 & 1 \\ -1 & 0 & 1 \end{vmatrix}$$

(a) (b)

Figure 2.18 Prewitt Operator Mask. (a) W_1 Mask used to compute G_x at centre point of the 3×3 region; (b) W_2 Mask used to compute G_y at that point.

The component of the gradient vector in the *x* direction G_x, as given in Equation (2.5.7), can be computed by using the mask shown in Figure 2.18a.

$$G_x = (x_7 + x_8 + x_9) - (x_1 + x_2 + x_3) \qquad (2.5.10)$$

Similarly in the *y* direction, G_y can be computed by using the mask shown in Figure 2.18b.

$$G_y = (x_3 + x_6 + x_9) - (x_1 + x_4 + x_7) \qquad (2.5.11)$$

The Prewitt window applies a (-1, 0, 1) weighting to pixels successively in the two coordinate directions, and effectively compounds the image density gradients in the image. The effectiveness of the Prewitt signal enhancement filter algorithm is shown in Figure 2.4 which clearly delineates the structures embedded in the original schlieren image, offering a substantially better definition of these structures than the original image.

Chapter 3 INDUCED STRUCTURES IN THE DIFFUSION FLAME

3.1 Numeral analysis of schlieren signals

According to Weinberg (1963), there is a unique relationship between the density and refractive index. A major feature of the laser schlieren measurements is that for the position close to the nozzle the flows are expected to contain significant or even dominant induced (coherent) structures. Making use of the Abel transform and with integration of Abel transform results, the complete distribution of the density functions can be formed.

The averaged time function of the schlieren signal records $\overline{\theta_i}(t, Y)$, which were measured in the first experiment, are recorded at different positions Y and form the basis for reconstruction of the structure in the flow due to periodic upstream acoustic excitation as sensed by the optical detection system. The recovered averaged signals $\overline{\theta_i}(t, Y)$ were measured with the beam deflection angle transverse to the axis of the nozzle (i = t) or parallel to the axis (i = a). The beam deflection is determined by standard optical refraction as

$$\theta_i = -\int \frac{\partial \delta}{\partial x_i} dy \qquad (3.1.1)$$

where $x_i = \xi$ or $x_i = \zeta$ for the axial and transverse deflection measurements respectively and the local refractive index in the flame is δ. Since the acoustic excitation to be applied emanates from within the upstream nozzle system in a symmetrical form we now assume that the distribution of δ is an axisymmetric function of radial distance from the nozzle axis (r) and of time (t) referenced to the excitation signal. It follows that the measured signal $\overline{\theta_i}(t)$ can be expressed as:

$$\overline{\theta_i}(Y,t) = 2\int_Y^\infty \frac{\partial \delta(r,t)}{\partial x_i} \frac{dr}{\left(1-(Y/r)^2\right)^{1/2}} \qquad (3.1.2)$$

where Y is the perpendicular distance from the sensing beam to the axis of the nozzle system. In the case where axial beam deflections (i = a) are sensed, Equation 3.1.2 becomes:

$$\overline{\theta_a}(Y,t) = 2\int_Y^{\infty} \frac{\partial \delta(r,t)}{\partial \xi} \frac{dr}{\left(1-(Y/r)^2\right)^{1/2}} \qquad (3.1.3)$$

It is clear that Equation 3.1.3 is an Abel integral equation at any particular time (t) for the radial distribution of the axial gradient of the refractive index and can be solved from the measured distribution $\overline{\theta_a}(Y,t)$ with traverse distance. Minerbo and Levy (1963) gave details of techniques for numerical solution of the Abel integral equation in terms of polynomial representations of the solution which were used here.

3.2 Inversion of the Abel integral equation

The inversion of the Abel integral equation is a widely used technique in the study of the radial function distributions under axially symmetric conditions where the quantities measured are the integration of property derivatives along the path of measurement.

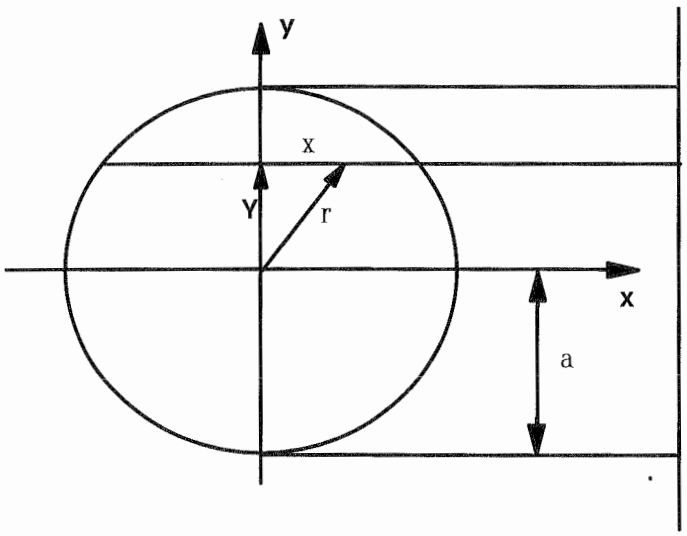

Figure 3.1 Cross section of Abel's integral routine.

With the help of Figure 3.1, the expression of Abel's integral equation can be generally written in the form below:

$$E(Y) = 2\int_y^a \frac{R(r)r}{\sqrt{r^2 - Y^2}} dr \qquad (3.2.1)$$

where

r = radius

y = position of measurement path

a = outside radius

$E(Y)$ = experimental data

Here $E(Y)$ can be, for instance, the radiance that is a function of the lateral coordinate x and can be measured spectroscopically. Since $R(r)$ is the unknown function in the present case, it must be removed from the integrand by a suitable assumption or by inverting Equation 3.2.1. The inversion of this equation is known exactly as :

$$R(r) = -\frac{1}{\pi}\int_r^a \frac{E'(Y)}{\sqrt{Y^2 - r^2}} dY \qquad (3.2.2)$$

However, the inversion procedure to obtain $R(r)$ presents many problems. The problem with the inversion is caused by the fact that many methods have a high noise amplification, especially methods which are equivalent to differentiation such as the direct solution using finite difference methods. There are a variety of numerical methods for performing the inversion. Nestor and Olsen (1960) and many others developed methods for inversion by using the numerical integration which use interpolation formulae. Freeman and Katz (1960) might have been the first to suggest a least square fit of all data by a polynomial whose inverse is known exactly. The method of orthogonal polynomial least square was successfully developed by Minerbo and Levy (1969). A more recent method based on spectral differentiation was proposed by Anderssen (1973).

When the experimental data distribution is simple, the choice between the direct numerical method and the least square method can be based on the noise amplification. However, the Minerbo and Levy method has the disadvantage of the uncertainty involved in selecting the polynomial order. The Anderssen method has to deal with more data (50 points) to obtain a good result and it is a much more complicated method. Since the experimental data in the present work is quite simple, we can assume the experimental data $E(Y)$ do not contain a constant component and have a unique continuous solution with $E(a)=0$, it is more convenient to use the

Minerbo and Levy method. If the data model is too complicated to use the Minerbo and Levy method, the experimental data should be smoothed by the cubic spline interpolation before direct numerical integration.

To construct the inversion process, Minerbo and Levy assumed that the solution does not contain a constant component and has a zero value at the tail (r = a). The experimental data are represented by a smooth orthogonal polynomial, and the noise values in the data are assumed independent of each other and random. They also suggested that the experimental data should approach zero smoothly by manual fitting and by subtraction of any background level that may be present.

We suppose that *E(y)* is specified by data $E(y_n)$ at y_n, $n = 0,1,2,3,...,N$ with $y_0 = 0$ and $y_n = a$. The intervals do not have to be equal. The numerical inversion of the equation is:

$$R_k(r_i) = \frac{1}{a}\sum_{n=0}^{N} T_{in}^{k} E(Y_n) \tag{3.2.3}$$

where

N = number of data points

K = polynomial degree

$E(Y_n)$= experimental data

and

$$T_{in}^{k} = \sum_{m=0}^{k} q_m(u_i)\frac{p_m(v_n)}{\sum_{n=0}^{N} p_m^2(v_n)} \tag{3.2.4}$$

in Equation 3.2.4, where

$$u = 1 - \frac{r^2}{a^2} \tag{3.2.5}$$

$$v = 1 - \frac{Y^2}{a^2} \tag{3.2.6}$$

$$p_{m+1}(v)=(v-\alpha_m)p_m(v)-\beta_m p_{m-1}(v) \tag{3.2.7}$$

$$p_0=1$$

$$p_{-1}=0$$

In Equation 3.2.7, the α_m and β_m are calculated by formulae:

$$\alpha_m=\frac{\sum_{v=0}^{a} W(v)v\,p_m^2(v)\nabla V}{\sum_{v=0}^{a} W(v)\,p_m^2(v)\nabla V} \tag{3.2.8}$$

$$\beta_m=\frac{\sum_{v=0}^{a} W(v)v\,p_m(v)\,p_{m-1}(v)\nabla V}{\sum_{v=0}^{a} W(v)\,p_m^2(v)\nabla V} \tag{3.2.9}$$

From Equation 3.2.4, we have then

$$q_m=\sum_{j=0}^{m}\lambda_j c_j^m u^{j-1/2} \tag{3.2.10}$$

where

$$\lambda_j=\frac{j!}{p[(j-1/2)(j-3/2)\cdots 1/2]} \tag{3.2.11}$$

$$\lambda_0=0$$

$$C_j^{m+1}=C_{j-1}^m-\alpha_m C_j^m-\beta_m C_j^{m-1} \tag{3.2.12}$$

$$C_0^0=0$$

$$C_j^m=0 \qquad \text{if } j>m \text{ or } m<0 \text{ or } j<0$$

More detail about the Abel inversion can be found in Minerbo and Levy (1969) and Rerkshanandana (1989).

3.3 Estimated errors of the Abel transform

The Minerbo and Levy method is a least square method of orthogonal polynomial fitting. Any wrong measurement will greatly distort the results because in the squaring process large residuals play a dominant part.

If the data structure is too complex, the errors of inversion will also be more complex. Because our experimental data is simple, the data structure suits the assumption of Abel's inversion, which is that the data has no constant. The errors of inversion can be separated into absolute errors and noise errors which are discussed as follows.

(1) The absolute errors of Abel transform

The absolute errors of Minerbo and Levy method were carried out with theoretical curves having known inverse results (Minerbo and Levy, 1963) and the errors can be obtained by comparing the theoretical results with inversion results. Two functions were chosen to test the accuracy of inversion.

A. The first function is

$$Y(y)=-\frac{2}{3}\left(\frac{1}{4}-y^2\right)^{1/2}(1+8y^2)+\frac{4}{3}(1-y^2)^{1/2}(1+2y^2)-4y^2\log\left\{\left[1+(1-y^2)^{1/2}\right]\Big/\left[\frac{1}{2}+\left(\frac{1}{4}-y^2\right)^{1/2}\right]\right\}$$

$$\text{when } 0\le y\le\frac{1}{2} \qquad (3.3.1a)$$

or

$$Y(y)=\frac{4}{3}(1-y^2)^{1/2}(1+2y^2)-4y^2\log\left\{\left[1+(1-y^2)^{1/2}\right]/y\right\}$$

$$\text{when } \frac{1}{2}\le y\le 1 \qquad (3.3.1b)$$

The inversion of Equation 3.3.1 is

$$R(r) = 1 - 2r^2 \qquad \text{when } 0 \le y \le \frac{1}{2} \qquad (3.3.2a)$$

and

$$R(r) = 2(1-r)^2 \qquad \text{when } \frac{1}{2} \le y \le 1 \qquad (3.3.2b)$$

Table 3.3.1 shows the difference between calculated value (by the program used in this research) and the theoretical values of $R(r)$ for $N = 20$ equally spaced points.

Table 3.3.1 Accuracy test of Minerbo & Levy method applied to function A.

	1	2	3	4	5
	Position	$Y(r)$	$R(r)_{Theor.}$	$R(r)_{Calc.}$	*Differences*
	(y or r)	*(input)*	*(Theoretical)*	*(Calculated)*	*Vol.4- Vol.3*
1	0.00	1.000	1.000	1.0014	0.0014
2	0.05	0.9931	0.9950	0.9960	0.0010
3	0.10	0.9724	0.9800	0.9801	0.0001
4	0.15	0.9384	0.9550	0.9543	-0.0007
5	0.20	0.8915	0.9200	0.9194	-0.0006
6	0.25	0.8327	0.8750	0.8751	0.0001
7	0.30	0.7631	0.8200	0.8209	0.0009
8	0.35	0.6842	0.7550	0.7558	0.0008
9	0.40	0.5979	0.6800	0.6794	-0.0006
10	0.45	0.5069	0.5950	0.5930	-0.0020
11	0.50	0.4151	0.5000	0.5003	0.0003
12	0.55	0.3292	0.4050	0.4071	0.0021
13	0.60	0.2527	0.3200	0.3199	-0.0001
148	0.65	0.1861	0.2450	0.2436	-0.0014
15	0.70	0.1300	0.1800	0.1796	-0.0004
16	0.75	0.0845	0.1250	0.1261	0.0011
17	0.80	0.0495	0.0800	0.0806	0.0006
18	0.85	0.0247	0.0450	0.0438	-0.0012
19	0.90	0.0092	0.0200	0.0202	0.0002
20	0.95	0.0017	0.0050	0.0074	0.0024
21	1.00	0.0000	0.0000	0.0000	0.0000

B. The second function is

$$Y(y) = \frac{\sqrt{\pi}}{\beta}\left(1 - y^2\right)^{-1/2} \exp\left[\beta^2\left(1 - \frac{1}{1-y^2}\right)\right] \qquad (3.3.3)$$

The inversion of Equation 3.3.3 is known exactly as

$$R(r)=(1-r^2)^{-3/2}\exp\left[\beta^2\left(1-\frac{1}{1-r^2}\right)\right] \qquad (3.3.4)$$

The difference between calculated values (by the program used in this thesis) and the theoretical values of $R(r)$ is shown in Table 3.3.2.

Table 3.3.2 Accuracy test of Minerbo & Levy method applied to function B.

	1	2	3	4	5
	Position	$Y(r)$	$R(r)_{Theor.}$	$R(r)_{Calc.}$	*Differences*
	(y or r)	*(input)*	*(Theoretical)*	*(Calculated)*	*Vol.4- Vol.3*
1	0.00	1.6113	1.0000	0.9994	-0.0006
2	0.05	1.6085	1.0007	1.0004	-0.0003
3	0.10	1.5998	1.0029	1.0030	0.0001
4	0.15	1.5850	1.0063	1.0067	0.0004
5	0.20	1.5637	1.0109	1.0111	0.0002
6	0.25	1.5352	1.0163	1.0162	-0.0001
7	0.30	1.4986	1.0220	1.0219	-0.0001
8	0.35	1.4528	1.0275	1.0276	0.0001
9	0.40	1.3962	1.0315	1.0318	0.0003
10	0.45	1.3270	1.0327	1.0328	0.0001
11	0.50	1.2430	1.0286	1.0284	-0.0002
12	0.55	1.1416	1.0157	1.0157	0.0000
13	0.60	1.0198	0.9889	0.9892	0.0003
148	0.65	0.8749	0.9402	0.9405	0.0003
15	0.70	0.7055	0.8585	0.8585	0.0000
16	0.75	0.5141	0.7293	0.7295	0.0002
17	0.80	0.3125	0.5387	0.5391	0.0004
18	0.85	0.1310	0.2930	0.2932	0.0002
19	0.90	0.0231	0.0694	0.0707	0.0013
20	0.95	0.0001	0.0004	0.0054	0.0050
21	1.00	0.0000	0.0000	0.0000	0.0000

As shown in Tables 3.3.1 and 3.3.2, the Minerbo and Levy method has a good accuracy. Since the errors only increase at the tail part of the curve, this will not affect the results in the processing. The average errors are less than 0.4 %.

(2) Random noise amplification of inversion

The final accuracy of the inversion is limited by the growth of noise errors rather than by the absolute accuracy of the inversion method. The amplification of inversion noise errors is:

$$A_i^k = \left[\sum_{n=0}^{N}\left(T_{in}^N\right)\right]^{1/2} = \left[\sum_{m=0}^{K}\frac{q_m^2(u_i)}{N_m}\right]^{1/2} \qquad (3.3.5)$$

$$A^k = \left[\frac{1}{N}\sum_{i=0}^{N}\sum_{i=0}^{N}\left(T_{in}^k\right)^2\right]^{1/2} = \left[\frac{1}{N}\sum_{m=0}^{K}\frac{\|q_m\|^2}{N_m}\right]^{1/2} \qquad (3.3.6)$$

The factor A^k varies with the change of k and the number of data points. For any type of data, A^k provides an absolute bound for error amplification. The value of K will lie in a range where the absolute errors are still decreasing and the noise errors are increasing steadily with K.

Table 3.3.3 A_i^k - error amplification of Abel transform (radial distance from axis, i = 1, ..., 13) .

	A35.xx	A35.xxx	A70.xx	A70.xxx	R35.xx	R35.xxx	R70.xx	R70.xxx
i	K = 4	K = 5	K = 5	K = 4	K = 5	K = 5	K = 5	K = 4
1	1.8946	1.8135	2.3302	1.8946	2.4485	2.3302	2.4485	1.8135
2	1.6665	1.6329	2.0321	1.6665	2.0001	2.0321	2.0001	1.6329
3	1.1090	1.1720	1.3232	1.1090	1.3928	1.3232	1.3928	1.1720
4	0.6648	0.7045	0.8152	0.6648	0.8367	0.8152	0.8367	0.7045
5	0.7766	0.6681	0.9568	0.7766	0.8503	0.9568	0.8503	0.6681
6	0.8294	0.8041	0.9711	0.8294	0.9666	0.9711	0.9666	0.8041
7	0.6631	0.7208	0.7571	0.6632	0.8182	0.7571	0.8182	0.7208
8	0.8155	0.6341	0.8388	0.8155	0.7173	0.8388	0.7173	0.6341
9	0.8673	0.8329	0.8939	0.8673	0.8597	0.8939	0.8597	0.8329
10	0.7925	0.7665	0.8321	0.7925	0.8139	0.8321	0.8139	0.7665
11		0.8373	1.1841		0.8581	1.1841	0.8581	0.8373
12			0.8712		1.1185	0.8712	1.1185	
13					0.8883		0.8883	
A^k	1.0869	1.0854	1.2860	1.1449	1.1993	1.2504	1.1993	1.0367

Table 3.3.3 shows the noise error amplification of the Abel transform varies with the change of i (which represent measurement position, low i means closer to the exit nozzle, i = *1* is the laser light point on the centre of the nozzle) in this thesis. Comparison of the amplification factor A_i^k shows the superiority of the polynomial method, not only at the middle of the range of distance from nozzle axis (i = 1, ..., 13) where the difference is striking, but also in the range i = 4 to 10 where the variation is flat and close to unity. The factors A_i^k increase when data is near to the nozzle axis or far from the nozzle axis but remain at a tolerable level. Because the data measured at

or near the nozzle have a very important influence in the whole data transform and A_i^k has a squared effect (if the error at one point is 10 times bigger than most of the other, it will have the same effect on the sum of squares as will 100 other smaller values), the increase of A_i^k at $i=1, 2, 3$ will affect the results of the Abel transform. Particularly with high frequency excitation, the signal will contain much more noise than with low frequency (Tables 2.3.1 and 2.3.2). However the polynomial method is clearly preferable for application to experimental data that contain appreciable random errors or short range fluctuations as this method has much less noise error than other transform methods (Minerbo and Levy, 1963).

3.4 Abel transform of the flame signal records

The set of averaged time records is denoted by the function $Q_j(t, Y)$, where t is the time from the reference datum in the excitation signal, $j = 0, 1, 2, ..., N$, N is the number of set records. If the disturbances propagate across the detection beam at velocity V_c then $t = X/V_c$, where X is the streamwise coordinate in the convecting coherent structure. The direction of the deflection sensed by the schlieren system (n) can be varied from the axial direction ($n = a$) to the radial (transverse) direction ($n = r$).

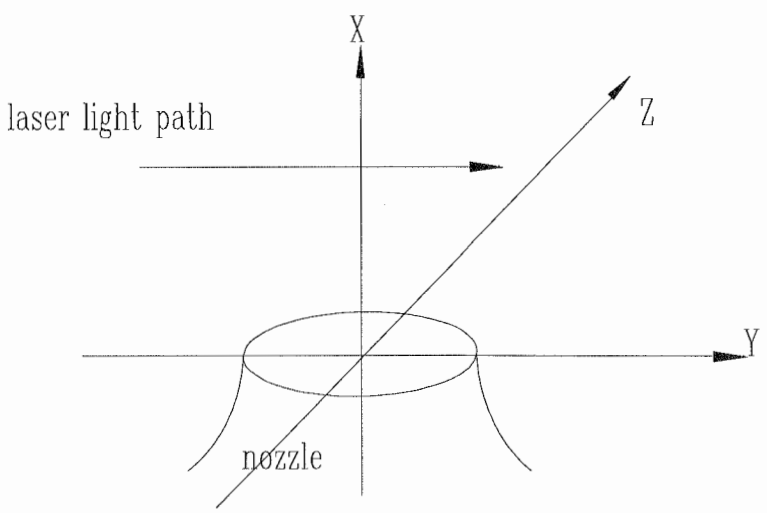

Figure 3.2 Arrangement of schlieren measuring system.

If the refractivity index of the coherent structure in the flow is δ then the schlieren signal is given by:

$$\theta_n(t,Y) = A\int(\frac{\partial\delta}{\partial\xi})d\eta \qquad (3.4.1)$$

where A is the constant relating beam bending to refractive index gradient and η is the coordinate along the measuring beam path, ξ is the direction perpendicular to the light path, $d\eta = rdr/\sqrt{r^2 - Y^2}$.

The most important factors influencing the accuracy of the Minerbo-Levy method are:
(1) random noise characteristics on the measured distribution *E(Y)*.
(2) a suitable order(k) of the polynomial of transform data.
(3) number of experimental data points.

The random noise of the data should be minimised by means of averaging random data over a thousand points. The order of the polynomial, according to the Minerbo-Levy method for adequate accuracy, can be obtained by using the following: $K = 4$ for $N = 10$ data points, $K = 8$ for $N = 20$, and $K = 11$ for $N = 30$.

In the present case, the data points number between 11 and 13, which is sufficiently accurate for Abel's inversion of order 4 in the polynomial for 11 data points and order 5 for 13 points.

(A) The axial density gradient:

When the beam deflection in the axial deflection is sensed, then at time t_i the averaging output signal is given as follows:

$$\theta_a(t_i, y) = -\int_y^r \left[\frac{\partial\delta}{\partial x}\right]_{t_i} dy \qquad (3.4.2)$$

Since $\dfrac{\partial\delta}{\partial x}$ is axisymmetric, the above equation can be modified by the following procedure:

Because

$$r = \sqrt{Y^2 + z^2}$$

$$y = \sqrt{r^2 - z^2}\ ,$$

we have

$$\frac{dr}{dy} = \frac{y}{r}$$

$$dy = \frac{rdr}{\sqrt{r^2 - z^2}}$$

Therefore Equation 3.4.2 becomes,

$$\theta_a(t_i, z) = -2\int_z^r \left[\frac{1}{2}\frac{\partial \delta}{\partial x}\right]_{t_i} \frac{rdr}{\sqrt{r^2 - z^2}} \qquad (3.4.3)$$

This is a Abel type equation, corresponding to Equation 3.1.3

$$E(Y_n) = \theta_a(t_i, z_n) \qquad (3.4.4)$$

$$R_k(r_i) = \left[\frac{1}{2}\frac{\partial \delta}{\partial x}\right]_{t_i} \qquad (3.4.5)$$

The inversion process can be completed by Equation 3.2.3

(B) The radial density gradient:

The radial deflection angle $\theta_r(t_i, y)$ obtained by averaging the transverse component output signal from the schlieren system is expressed as

$$\theta_r(t_i, y) = -2\int_y^r \left[\frac{1}{2}\frac{\partial \delta}{dz}\right]_{t_i} dy \qquad (3.4.6)$$

We have assumed that refractivity distribution of the flow from the circular nozzle is axisymmetric, and this leads to the axial asymmetry of the radial gradient distribution. The modification of Equation 3.4.6 to an Abel type equation can be shown below

Because

$$r = \sqrt{y^2 + z^2}$$

and

$$z = \sqrt{r^2 - y^2}$$

we have

$$\frac{dr}{dz} = \frac{z}{r}$$

and

$$dy = \frac{rdr}{\sqrt{r^2 - z^2}}$$

Equation 3.4.6 can be rewritten as

$$\theta_r(t_i, z) = -2\int_z^r \left[\frac{1}{2}\frac{\partial \delta}{\partial r}\right]_{t_i} \left[\frac{dr}{dz}\right] \frac{rdr}{\sqrt{r^2 - z^2}} \qquad (3.4.7)$$

or

$$\theta_r(t_i, z) = -2\int_z^r \left[\frac{1}{2}\frac{\partial \delta}{\partial r}\right]_{t_i} \left[\frac{z}{r}\right] \frac{rdr}{\sqrt{r^2 - z^2}} \qquad (3.4.8)$$

The above equations need further modification to the form of Abel's integral equation:

$$\frac{\theta_r(t_i, z)}{z} = -2\int_z^r \left[\frac{1}{2r}\frac{\partial \delta}{\partial r}\right]_{t_i} \frac{rdr}{\sqrt{r^2 - z^2}} \qquad (3.4.9)$$

This is a Abel type equation, corresponding to Equation 3.2.1

$$E(Y_n) = \theta_r(t_i, z_n) / z_n \qquad (3.4.10)$$

$$R_k(r_i)=\left[\frac{1}{2r}\frac{\partial\delta}{\partial r}\right]_{t_i} \tag{3.4.11}$$

If we let $z = y$, then the solution of this equation is:

$$R(r)=\left[\frac{1}{2r}\frac{\partial\delta}{\partial r}\right]_{t_i}=-\frac{1}{\pi}\int_r^a\frac{\partial}{\partial y}\left[\frac{\theta_r(t_i,Y)}{y}\right]\frac{dy}{\sqrt{Y^2-r^2}} \tag{3.4.12}$$

It is clear that $E(y_n)$ can not be obtained directly at $y = 0$. However, the radial deflection angle $\theta(0)$ should here always equate zero in theory, even if this assumption is disturbed by noise in the data. Thus L'Hospital's rule can be used here:

$$\lim_{y\to 0}\frac{\theta_r(y)}{y}=\frac{\dfrac{d\theta_r(y)}{dy}}{\dfrac{dy}{dy}}=\frac{d\theta_r(y)}{dy} \tag{3.4.15}$$

$$\frac{d\theta_r(y_0)}{dy_0}=\frac{\theta_r(y_1-y_0)}{y_1-y_0}-\frac{1}{3}(y_1-y_0)\theta_r''(y_0) \tag{3.4.16}$$

Here $\theta_i''(y_0)$ is always equal to zero, and we have:

$$\frac{d\theta_i(y_0)}{dy_0}=\frac{\theta_i(y_1)-\theta_i(y_0)}{y_1-y_0} \tag{3.4.17}$$

By the above method, all $R(t_i,r)$ at t_i *(i = 0, 1, 2, 3, ...)* distribution can be obtained.

All pre-Abel transform and after Abel transform functions are given in Figures 3.3~10. The pre Abel transform functions show clear trends in general. The functions after the Abel transform are smooth and also show certain characteristics. We shall consider the reconstruction of the detected structure from both axial and radial results in the next section, as both the pre and post Abel transform results are difficult to interpret physically at this stage of the analysis.

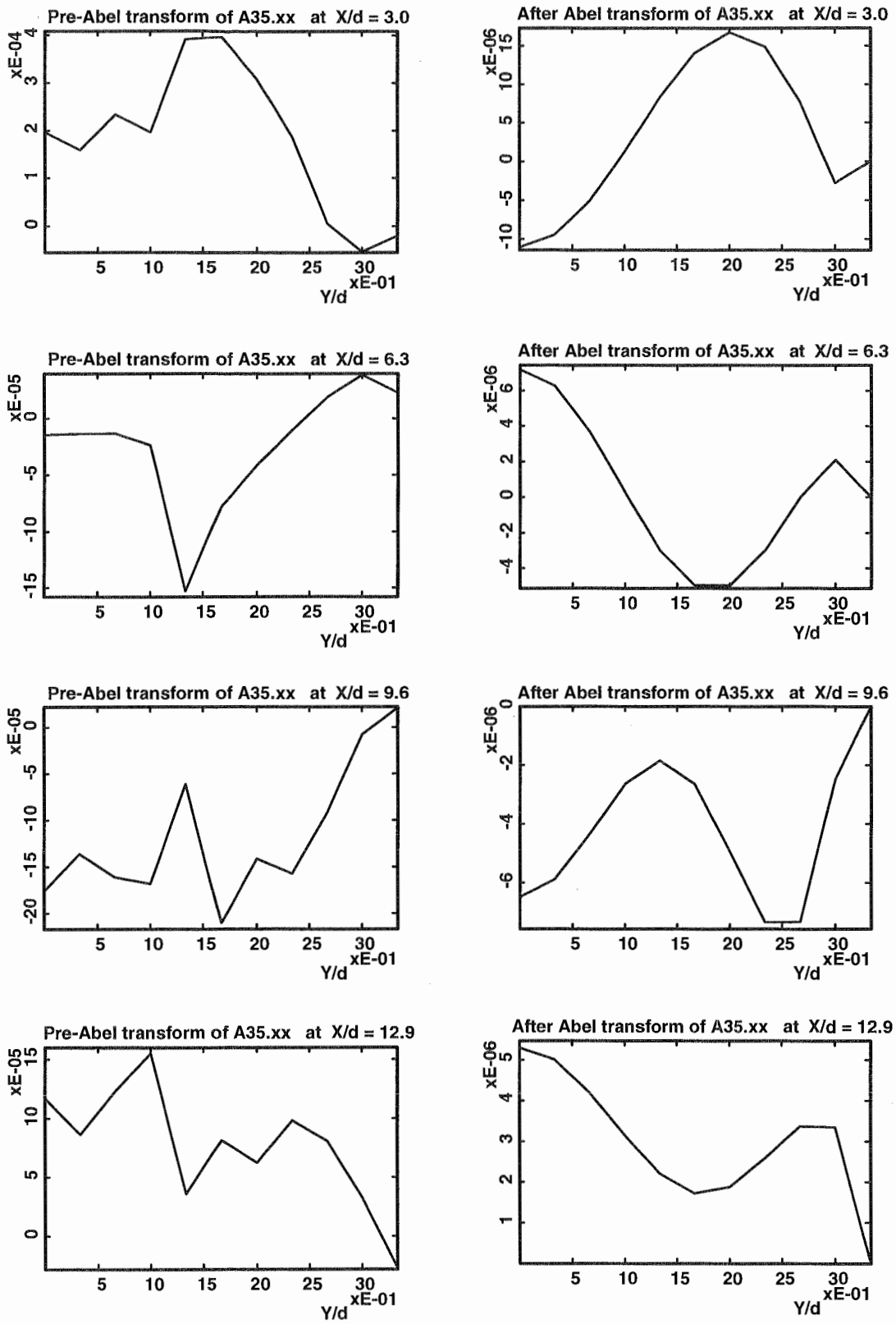

Figure 3.3 Selected data of A35.xx before and after Abel integral transform using Minerbo and Levy method (1969). Vertical ordinate radian, horizontal ordinate Y/d, Y = distance from axis, d = diameter of nozzle. Marked value X/d, X = distance from laser beam plane (evaluated from record time from datum and convection velocity).

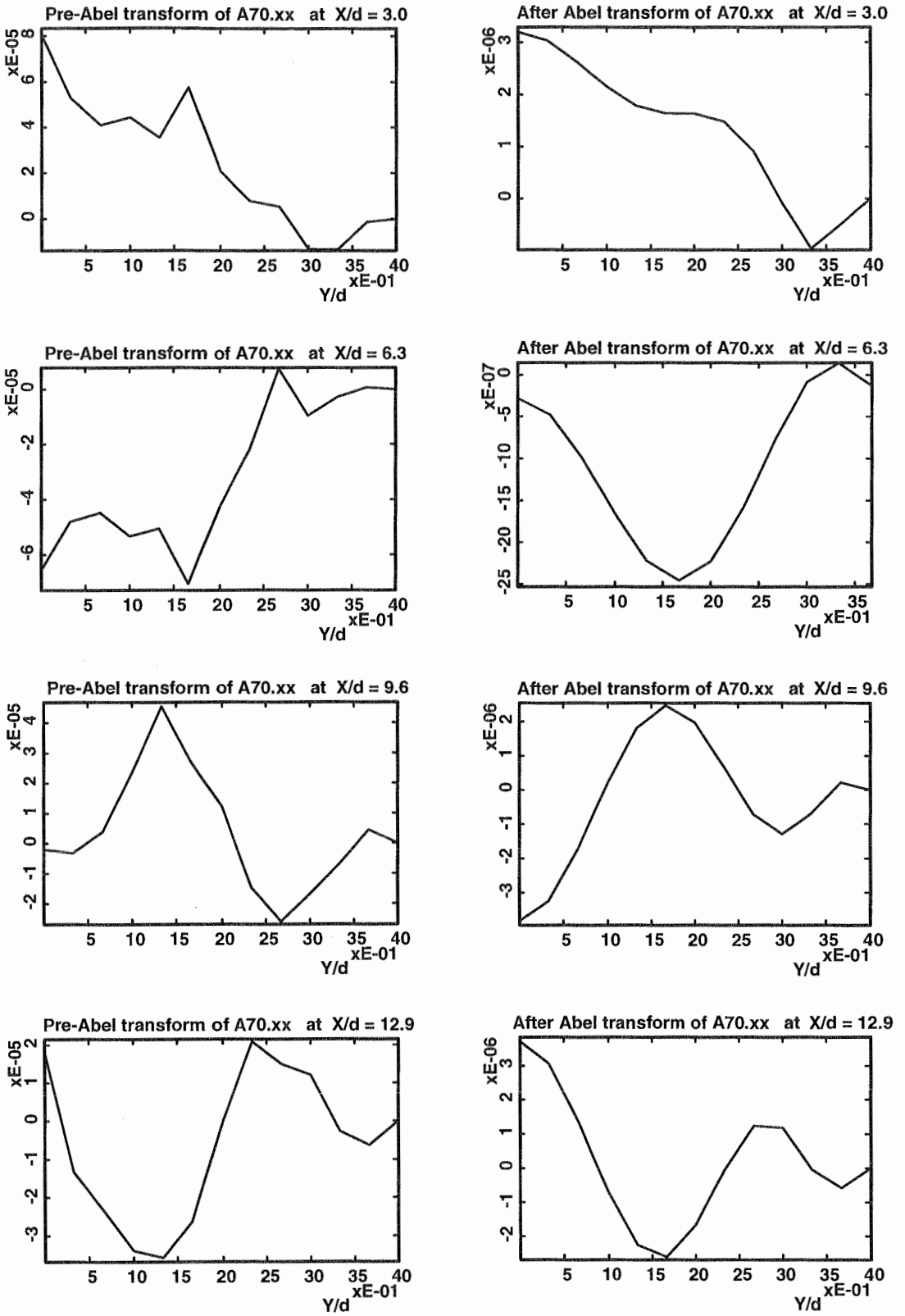

Figure 3.4 Selected data of A70.xx before and after Abel integral transform using Minerbo and Levy method (1969). Vertical ordinate radian, horizontal ordinate Y/d, Y = distance from axis, d = diameter of nozzle. Marked value X/d, X = distance from laser beam plane (evaluated from record time from datum and convection velocity).

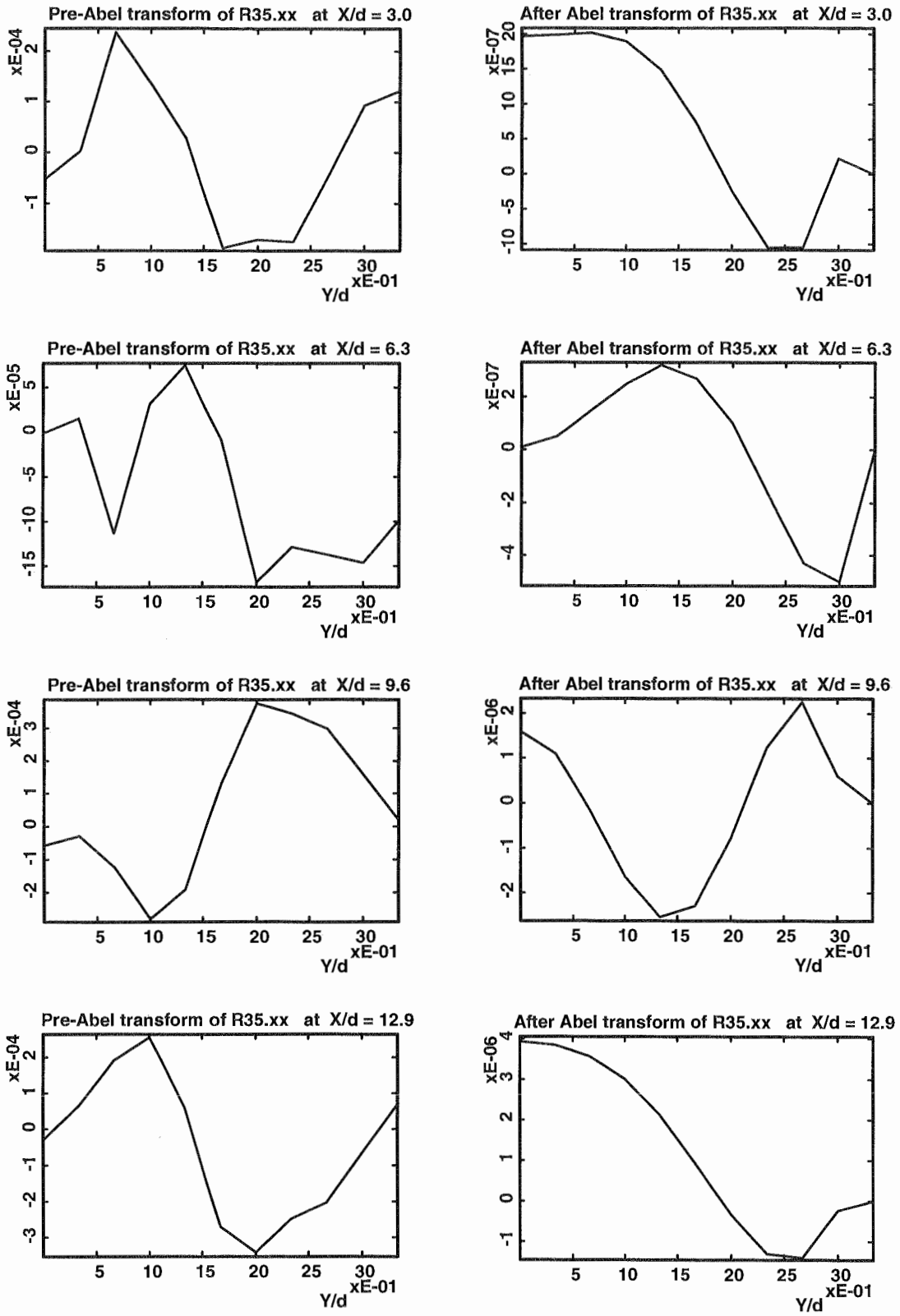

Figure 3.5 Selected data of R35.xx before and after Abel integral transform using Minerbo and Levy method (1969). Vertical ordinate radian, horizontal ordinate Y/d, Y = distance from axis, d = diameter of nozzle. Marked value X/d, X = distance from laser beam plane (evaluated from record time from datum and convection velocity).

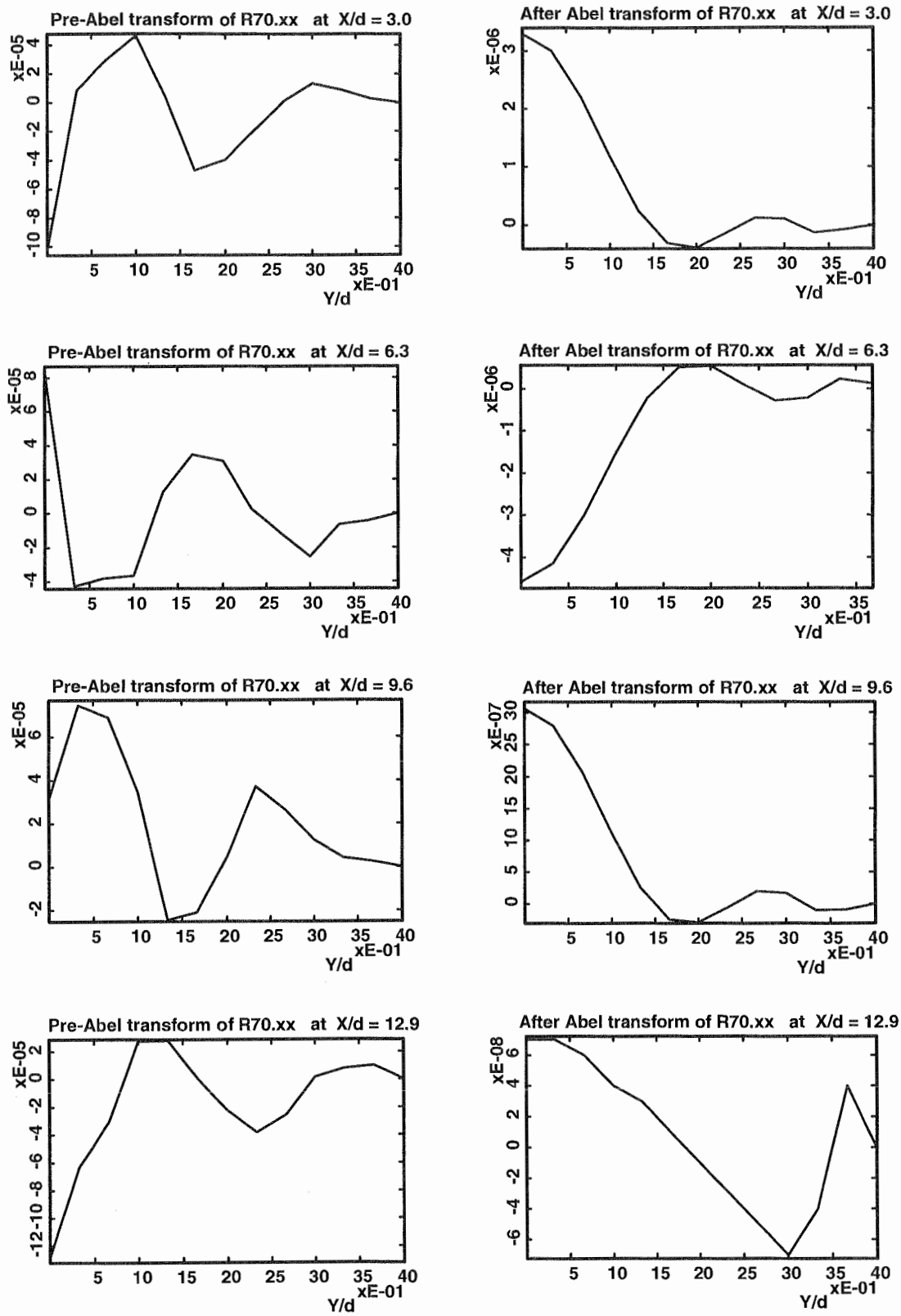

Figure 3.6 Selected data of R70.xx before and after Abel integral transform using Minerbo and Levy method (1969). Vertical ordinate radian, horizontal ordinate Y/d, Y = distance from axis, d = diameter of nozzle. Marked value X/d, X = distance from laser beam plane (evaluated from record time from datum and convection velocity).

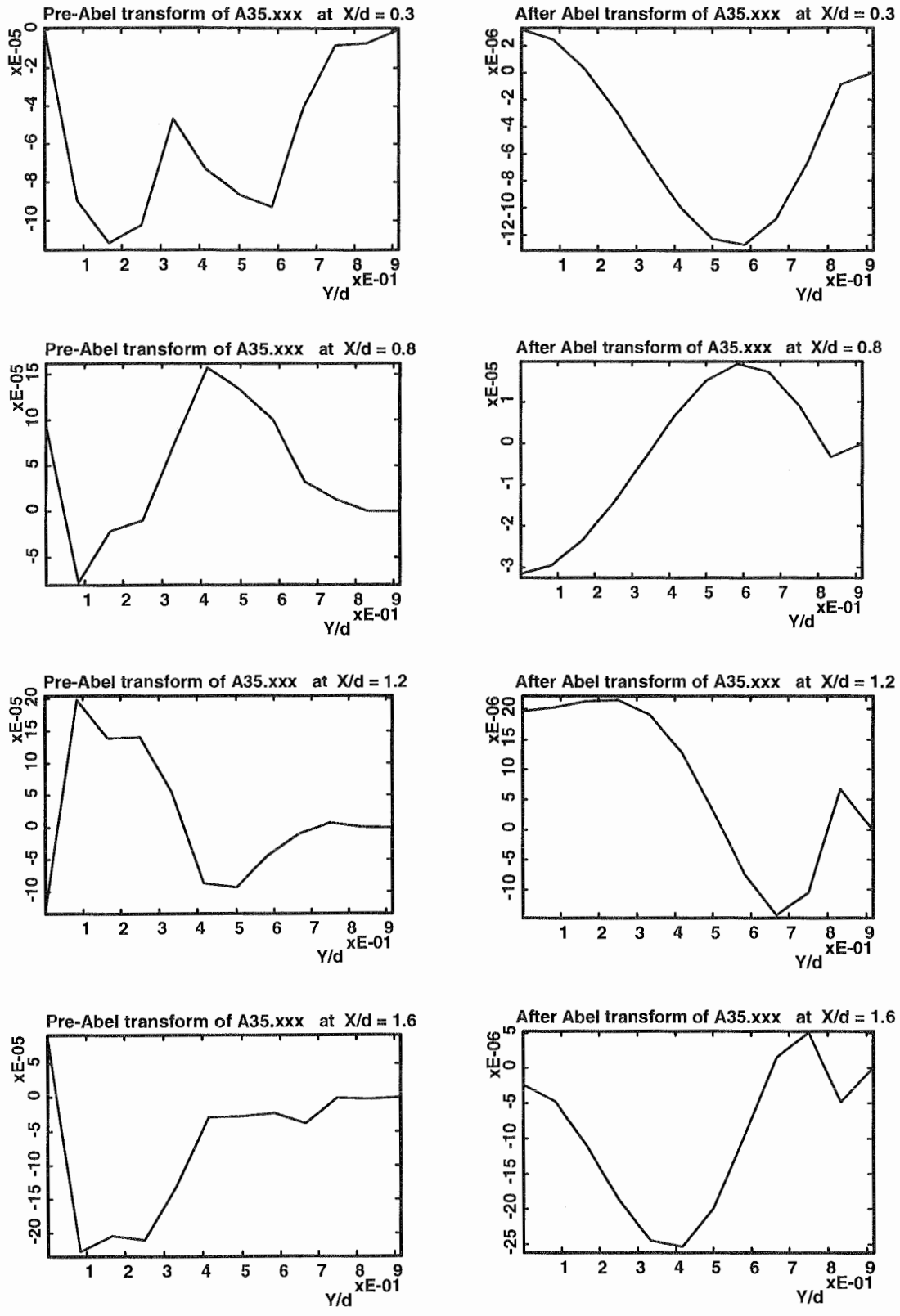

Figure 3.7 Selected data of A35.xxx before and after Abel integral transform using Minerbo and Levy method (1969). Vertical ordinate radian, horizontal ordinate Y/d, Y = distance from axis, d = diameter of nozzle. Marked value X/d, X = distance from laser beam plane (evaluated from record time from datum and convection velocity).

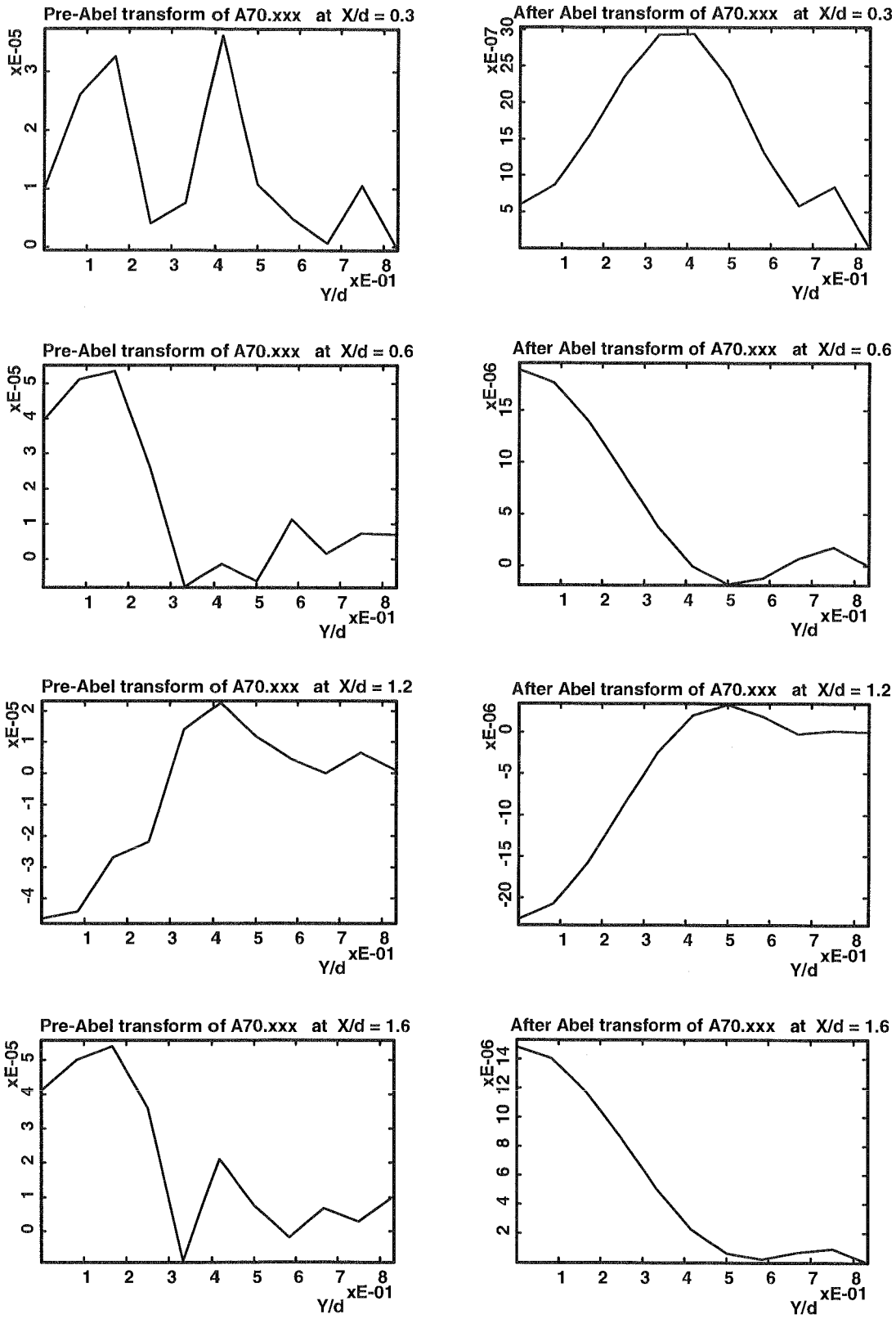

Figure 3.8 Selected data of A70.xxx before and after Abel integral transform using Minerbo and Levy method (1969). Vertical ordinate radian, horizontal ordinate Y/d, Y = distance from axis, d = diameter of nozzle. Marked value X/d, X = distance from laser beam plane (evaluated from record time from datum and convection velocity).

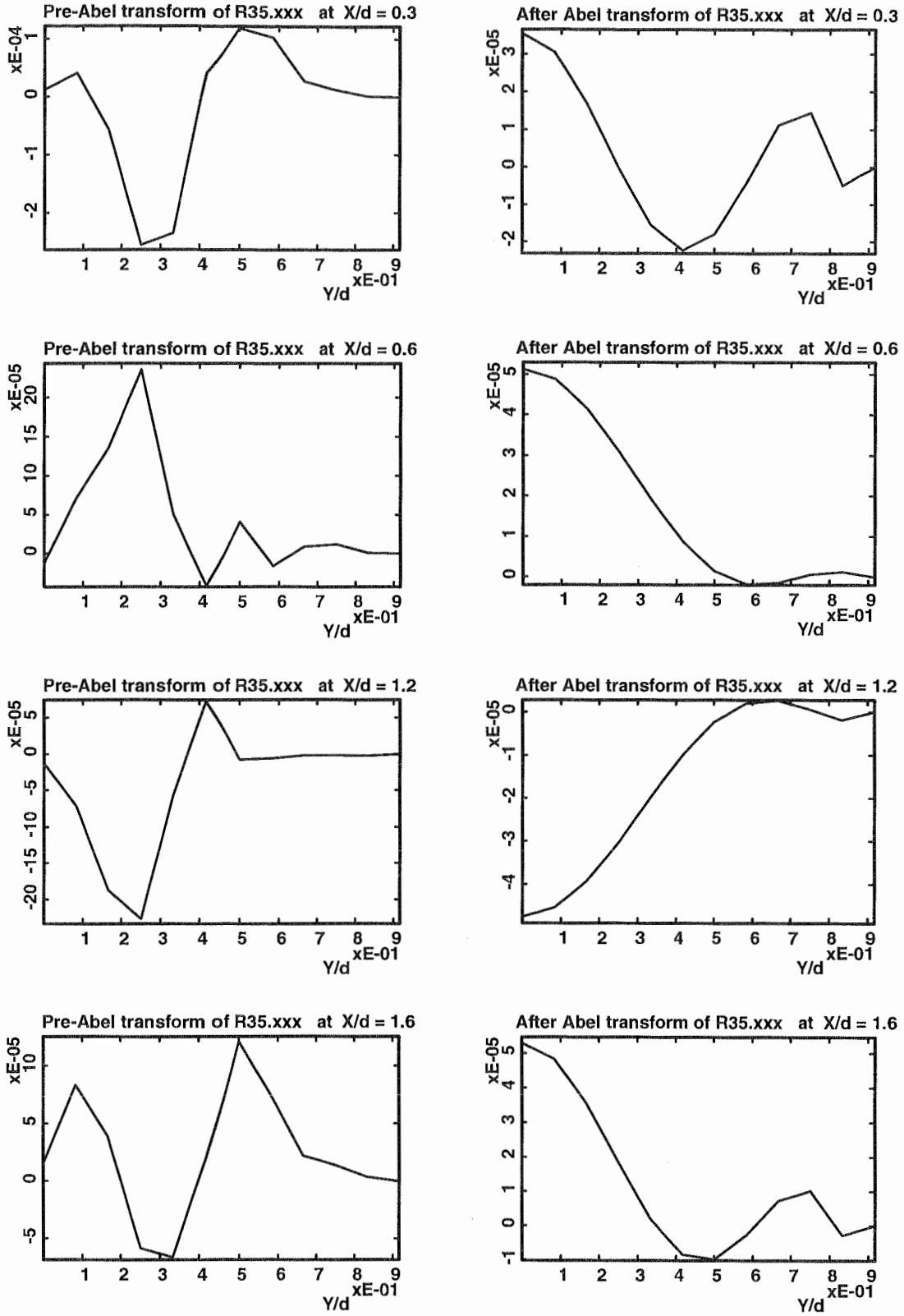

Figure 3.9 Selected data of R35.xxx before and after Abel integral transform using Minerbo and Levy method (1969). Vertical ordinate radian, horizontal ordinate Y/d, Y = distance from axis, d = diameter of nozzle. Marked value X/d, X = distance from laser beam plane (evaluated from record time from datum and convection velocity).

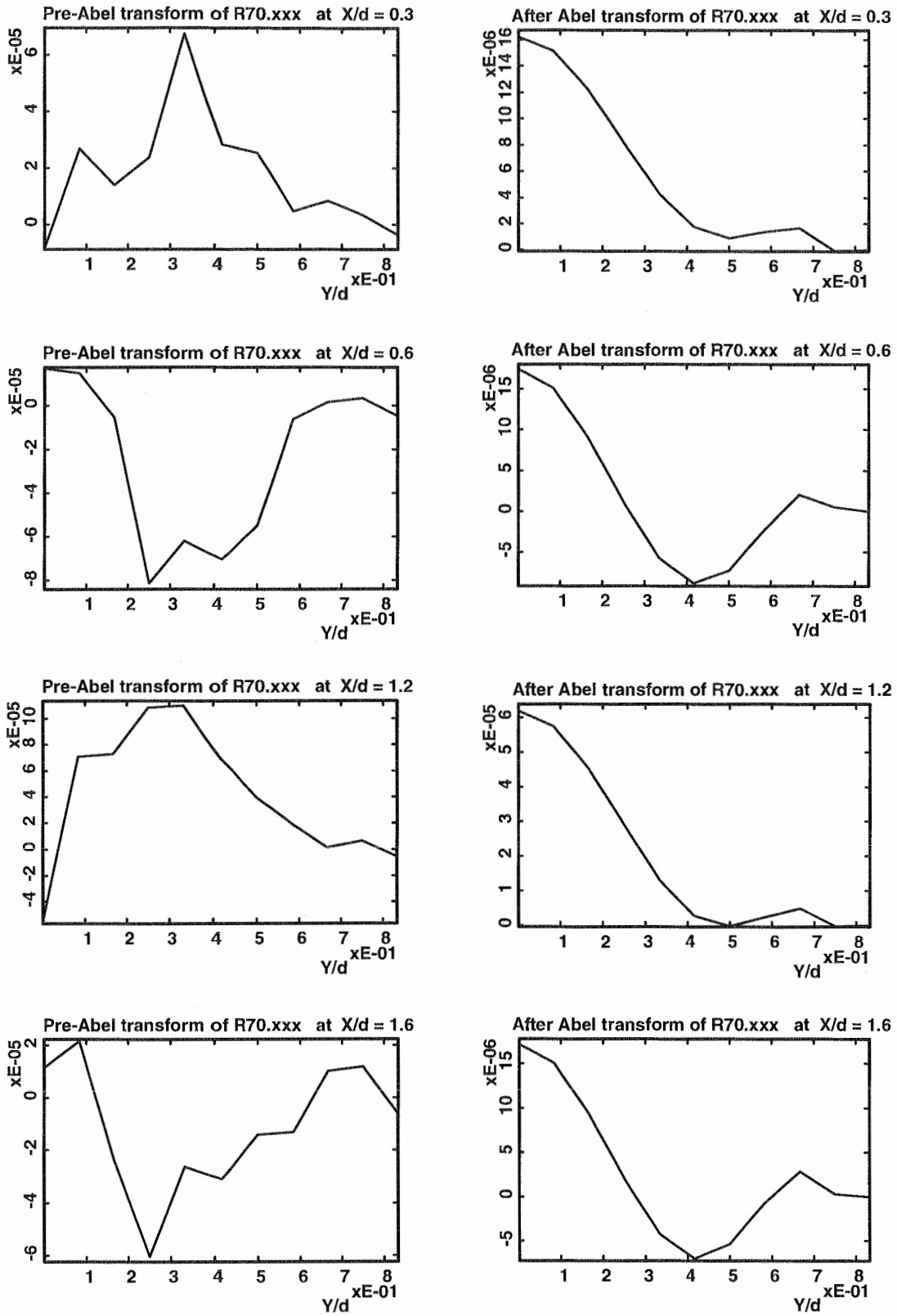

Figure 3.10 Selected data of R70.xxx before and after Abel integral transform using Minerbo and Levy method (1969). Vertical ordinate radian, horizontal ordinate Y/d, Y = distance from axis, d = diameter of nozzle. Marked value X/d, X = distance from laser beam plane (evaluated from record time from datum and convection velocity).

3.5 Integration of transform results

From the foregoing results, the radial distribution of the axial refractive index gradient as a function of time $\frac{\partial \delta(r,t)}{\partial x}$ and the radial distributions of the radial refractive index gradient as a function of time $\frac{\partial \delta(r,t)}{\partial r}$ can be determined. If the structure in the mixing region is moving at a convection velocity V_c then the time and axial coordinates are related simply by $x = V_c t$. This relationship (sometimes called the frozen pattern hypothesis) has been generally found to be a reasonable representation of turbulent mixing regions as the rate of deformation of the mixing structures is usually found to take place relatively slowly compared with the dominant convective motion with the flow. We may thus identify two approaches to the determination of the excited structure $\delta(r, \xi = V_c t)$ from the experimental data.

Firstly, according to Equation 3.4.11, at each time step the radial gradient data may be integrated from a point outside the flow ($r = a$) to give:

$$\delta_i(r) = -\int_a^r R_i(r) r dr + \delta(a) = -\sum_{j=0}^{m} R_k(r_j) r_j (r_{j+1} - r_j) + \delta(a) \tag{3.5.1}$$

where $\delta(a)$ is the mean refractivity index at $r = a$, which should equate to zero. Now

$$\delta_i(r) = -\int_a^r R_i(r) r dr = -\sum_{j=0}^{m} R_k(r_j) r_j (r_{j+1} - r_j) \tag{3.5.2}$$

where $i = 0, 1, 2, 3, \ldots, n$ are data points along X-direction and cover more than one period of data points; $j = 0, 1, 2, 3, \ldots, m$ are data points along the transverse direction (Y-direction) which represent the number of laser measurement positions. After repeating the processing of Equation 3.5.2 at each time step, we may form the complete distribution of the convecting refractive index $\delta(r, \xi = V_c t)$ in the flow at that time step.

The second approach, according to Equation 3.4.5, is to work from the axial deflection data on the basis of the frozen pattern hypothesis and integrate in the axial direction from the data,

$$\delta_j(a) = \int_0^{x_p} R_j(a)dx + \delta(0) = \sum_{i=0}^{n} R_k(r_i)(x_{i+1} - x_i) + \delta(0) \tag{3.5.3}$$

where $\delta(0)$ is mean refractivity index at $i = 0$. This integration from the data is then performed at each radial position to form the complete distribution $\delta(r,\xi)$. The constant of integration $\delta(0)$ is determined on the basis that the disturbance induced by the excitation represents a perturbation about a zero average value. Therefore at each radial position $\delta(0)$ was adjusted iteratively until:

$$\delta(a) = \int_{X_a}^{X_b} (R(a) + \delta(0))dx = 0 \tag{3.5.4}$$

so

$$\delta(0) = -\int_{X_a}^{X_b} R(a)dx \tag{3.5.5}$$

Where X_a and X_b are the start and end points of periodic convecting distance Xp. The periodic data length is approximately 300 points. For a full scale investigation of the density structure of flames, we used 450 data points, which are about one and a half times the period of the data. The data period expressed as a streamwise distance, Xp, is 52 mm for 40 Hz data and 6.5 mm for 420 Hz data. This represents 8.5 times the inner nozzle diameter for low frequency and 1.1 times for high frequency. Obviously the low frequency case has a much larger distribution scale than high frequency which suggests that the former distribution is more easily measured than in the latter case.

The results of the preceding analysis forms the basis for computation of the refractive index distribution field in the X-R plane (i.e. on the basis of downstream convecting flow and radial distance from the nozzle axis). Visualisation of the resulting distribution was achieved by using the software "Graph tools" which shows distributions in the form of contour diagrams as in Figures 3.11 to 3.14.

Tables 3.5.1 and 3.5.2 summarise the results of maximum and minimum refractive index of the observed diffusion flame fluctuation. At the higher excitation frequency (Figure 3.13), the refractive index has quite small size disturbances near the flow axis with alternating maximum and minium values. The overall wavelength is approximately the same as the inner (fuel) nozzle diameter. At the observation point (6 times the inner nozzle diameter from the nozzle exit) the distribution has a

transverse diameter which is approximately twice the fuel nozzle diameter, and is of alternating sign along the flow axis. The magnitude of the alternating peaks and minima in the refractive index give an overall range of variation of 0.00011 from the axial defection data and 0.00018 from the transverse deflection data, an average 0.00014.

Table 3.5.1 Range of refractive index at low excitation frequency.

File name	A35.xx	R35.xx	A70.xx	R70.xx
Maximum	0.00019	0.00021	0.00007	0.00009
Minimum	-0.00015	-0.00016	-0.00005	-0.00008

Table 3.5.2 Range of refractive index at high excitation frequency.

File name	A35.xxx	R35.xxx	A70.xxx	R70.xxx
Maximum	0.00005	0.00015	0.00007	0.00009
Minimum	-0.00004	-0.00013	-0.00003	-0.00003

The discrepancy of refractive index disturbance between the two methods of analysis from axial or transverse deflection records can be attributed to the relatively small diameter of the inner fuel nozzle system (6 mm), the finite size of the measuring beam (~0.8 mm) and problems associated with lack of symmetry of the excitation. However, subject to these limitations due to resolution, the results of the two sets of analysis indicate fluctuations which are ± 23% of the refractive index of the ambient air or ± 6.5% of the refractive index of the propane fuel when cold. The refractive index depends on the extent of the combustion reaction and the relative concentration of the mixture. For the complete combustion of a stoichiometric mixture the refractive index can be reduced to 10% of the refractive index of cold air at ambient conditions. This indicates the potential for combustion to contribute a maximum reduction of refractive index by 90% of that of cold air. Hence the present observations with fluctuations of ±23% of the refractivity of cold air indicate quite severe fluctuations of conditions along the flow axis, but nevertheless fluctuations which are well within (± 5.1%) the overall maximum possible range (0.00137) set by the lower limit of complete stoichiometric combustion and the upper limit of cold, unreacted propane.

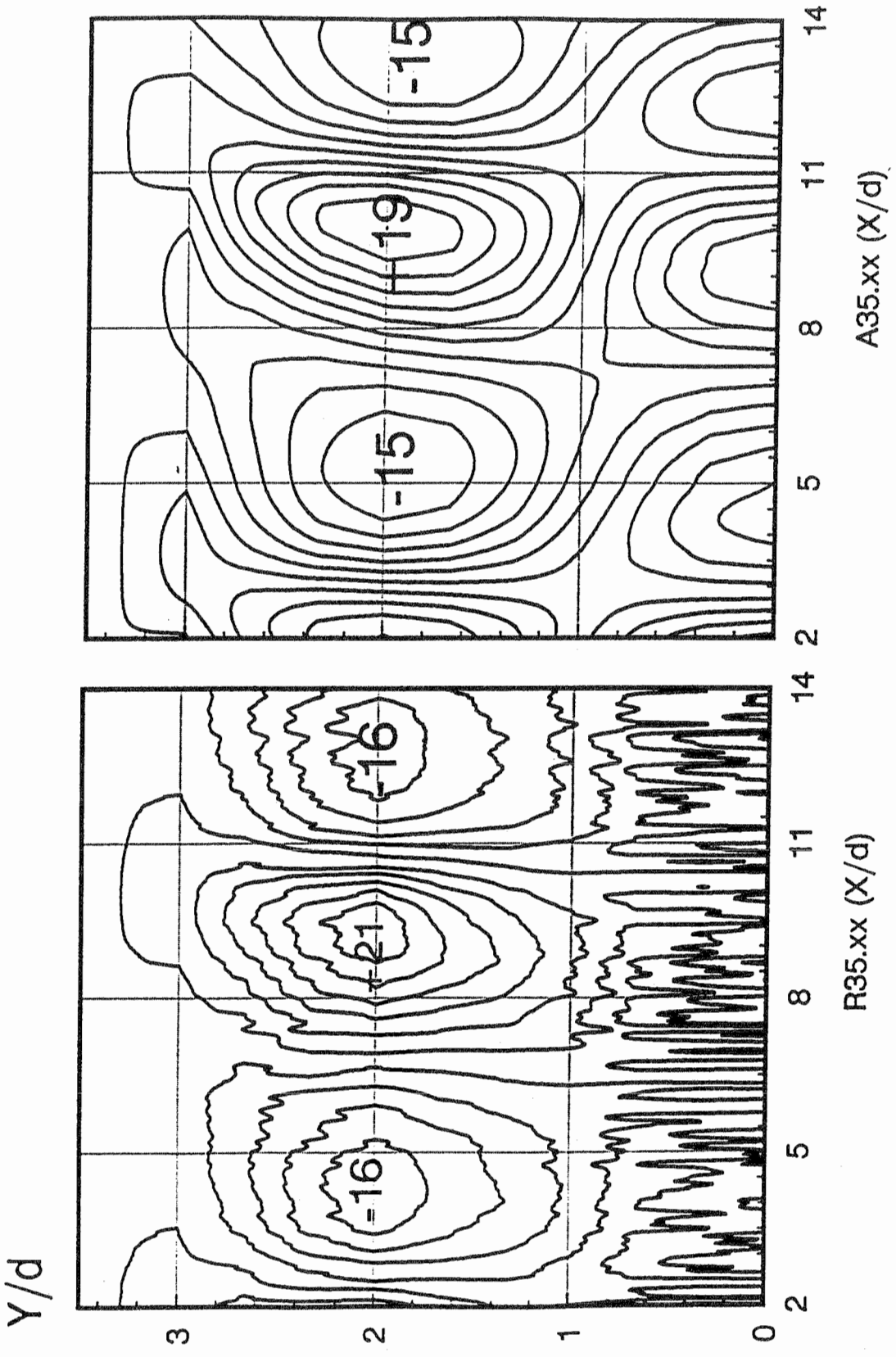

Figure 3.11 Refractive index structures induced by excitation of flame at Sti = 1.01 (f = 40 Hz). Figures marked indicate extremes of 10^{-5} (Y = Distance from nozzle axial, X = 35 mm: Distance from nozzle plane, d: nozzle diameter).

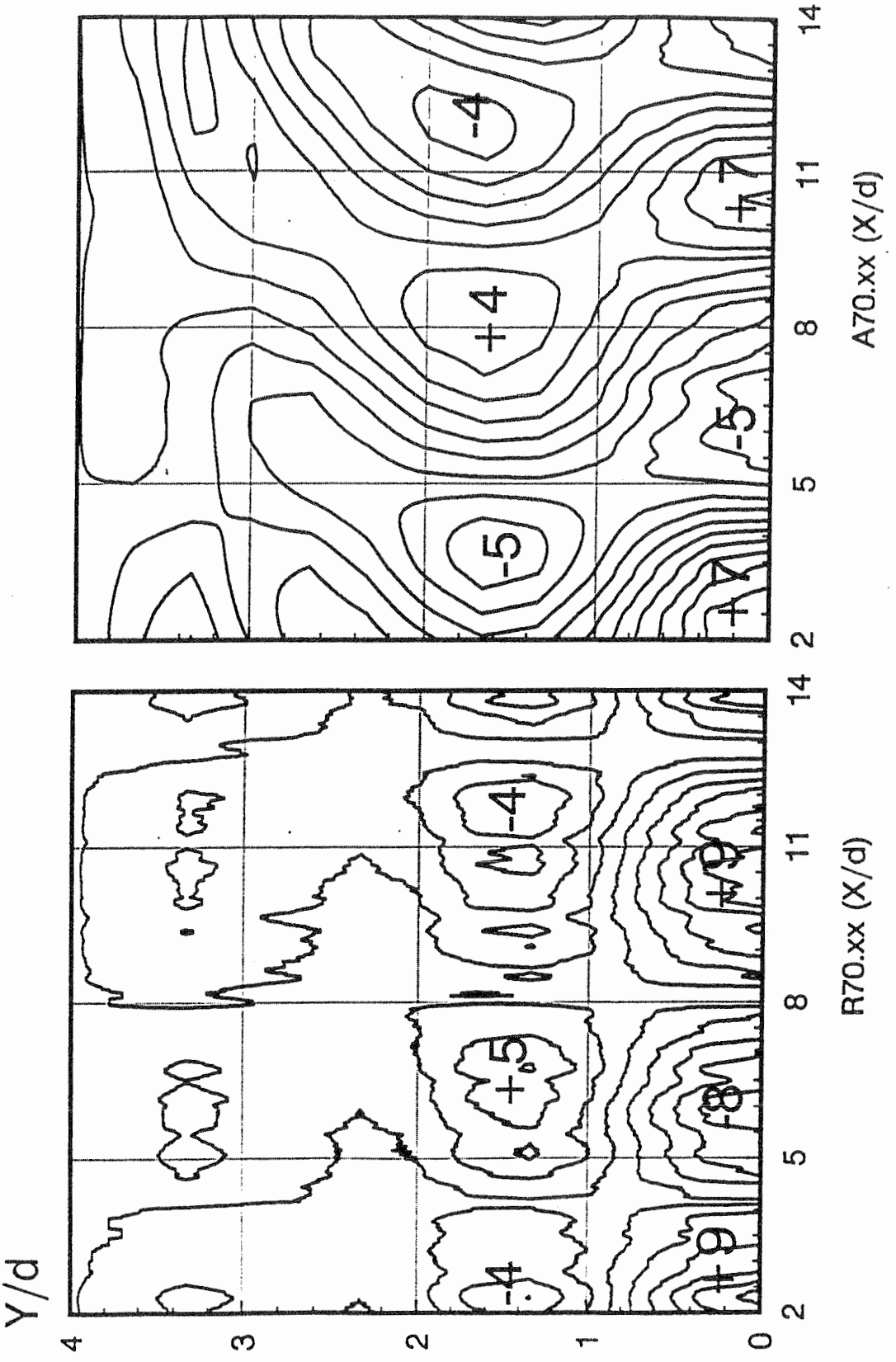

Figure 3.12 Refractive index structures induced by excitation of flame at Sti = 0.38 (f = 40 Hz). Figures marked indicate extremes of 10^{-5} (Y = Distance from nozzle axial, X = 70 mm : Distance from nozzle plane, d: nozzle diameter).

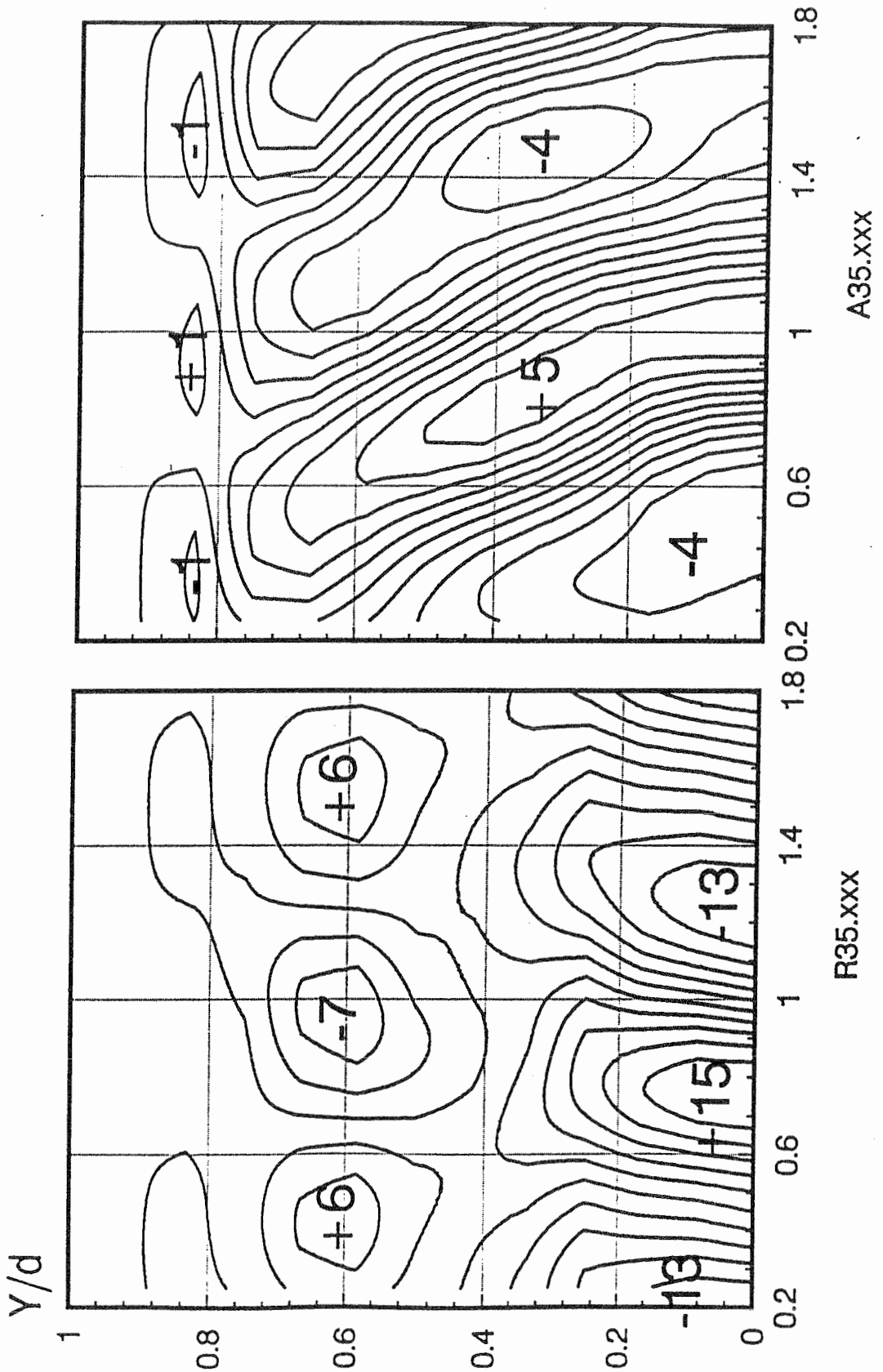

Figure 3.13 Refractive index structures induced by excitation of flame at St = 1.01 (f = 420 Hz). Figures marked indicate extremes of 10^{-5}. Y/d and X/d same as figure 3.11.

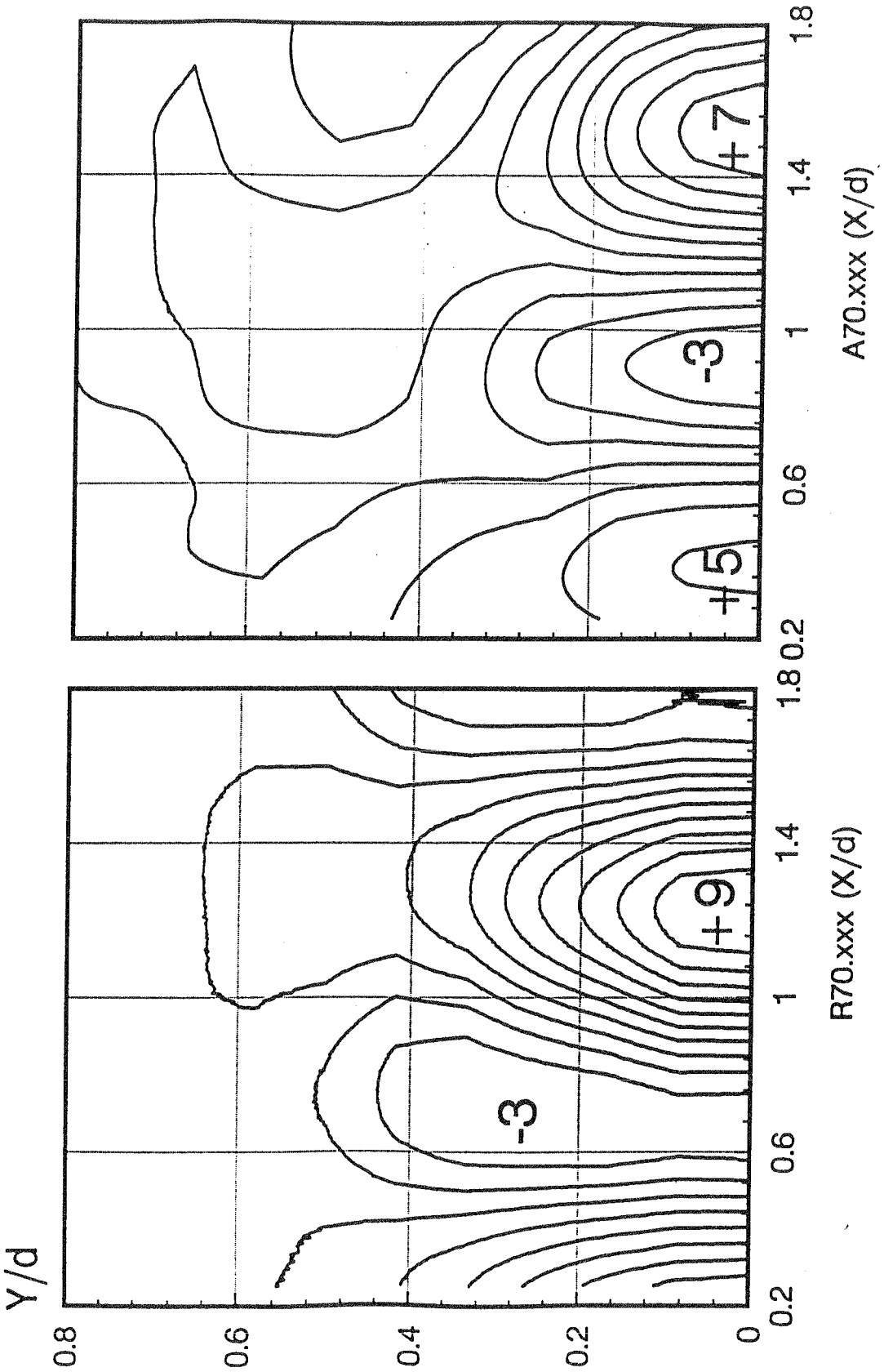

Figure 3.14 Refractive index structures induced by excitation of flame at Sti = 0.38 (f = 420 Hz). Figures marked indicate extremes of 10^{-5}. Y/d and X/d same as figure 3.13.

3.6 The refractive index and the flame properties

From the distribution of $\delta(r,\xi)$, we can further consider the distribution of flame properties. In general, the refractive index changes depending on variations of temperature, composition pressure and wave length of the light beam used. The variation of refractive index according to the wave length is usually very small (1.8% for air, Weinberg, 1963) and there is no need to consider further the change of refractivity caused by the optical wavelength. In a single component gas, it is sometimes more advantageous to transform refractive index fields into density fields (ρ). The basic relationship is the empirical law of Gladston and Dale which is usually stated as

$$M(N-1)/\rho = M\delta/\rho = R_{gd} \qquad (3.6.1)$$

Where R_{gd} is Gladston and Dale molecular refractivity taking the value of $M \times 0.2256 \times 10^{-3}\left[m^3/kg-moles\right]$ for the laser beams of this experiment (see Winarto, 1979), and M is the molecular weight of the gas.

The most commonly used theory to investigate the response of the schlieren system and refractive index to the physical characteristics of diffusion flames is based on the Lorenz and Lorentz relationship (Weinberg, 1963), which states that

$$M(N^2-1)/\rho(N^2+1) = R_{LL} \qquad (3.6.2)$$

where R_{LL} is Lorenz - Lorentz molar refractivity, N is refractivity, M is molecular Weight and ρ is density. The Lorenz - Lorentz molar refractivity is related to the Gladston - Dale constant (R_{gd}) by the relation

$$R_{LL} \approx 2R_{gd}/3 \qquad (3.6.3)$$

From Equation 3.6.1,

$$\delta = 3\rho R_{LL}/2M = 6.7 \times 10^{-5} \sum_j R_{LL_j} = \rho R_{gd}/M \qquad (3.6.4)$$

The value of R_{LL} of the various component gases can be generally found. In some situations, the association and dissociation of the gas molecules may also need to be

considered in the summation of R_{LL} for a complicate mixture (Weinberg, 1963). We will not consider this dissociation effect further because temperature changes have a much stronger effect in most cases at the relatively moderate temperatures which occur in the turbulent diffusion flame.

In general, combustion processes involve a large amount of heat release. At constant pressure, the variation of temperature causes the change in refractivity (Weinberg, 1963), that is

$$\delta = \delta_0 T_0 / T \tag{3.6.5}$$

Where the suffix *0* denotes the reference state where δ and T are known. Equation 3.6.5 indicates a greater sensitivity of δ at low temperature conditions, and at high temperatures the converse is true. Differentiating Equation 3.6.5 gives

$$d\delta = -\delta_0 T_0 dT / T^2 \tag{3.6.6}$$

This indicates that a given change in δ will correspond to an inverse proportional change to the square of the absolute temperature and to the temperature change. The effect of pressure on refractive index can be expressed as follows (Weinberg, 1963):

$$\delta = \delta_0 \left(P / P_0 \right)^{1/\gamma} \tag{3.6.7}$$

γ is specific heat ratio. The suffix *0* again denotes the known reference state. It is clear that no sensitivity effect of comparable magnitude to those related to temperature variations occurs due to pressure changes since in general the relative absolute pressure variation in open flames with low Reynolds number is very small and can be neglected.

Using the summation basis for compounding the refractivity of gas components in the Lorenz and Lorentz relationship, the refractive index of a multicomponent gas at a given pressure and temperature can be written as

$$\delta = \sum f_i \delta_i \tag{3.6.8}$$

where f_i and δ_i denote, respectively, the volume fraction and refractivity of the iTh component. When intermixing of gases is followed by the chemical reaction, the

variations of volume fraction caused by changes in the number of moles and bond rearrangement (new type of gases or radicals) will, dynamically, affect the total refractivity as shown in Equation 3.6.9. Mixing conditions at the interface between gas elements thus influence the change of refractivity.

For the two gas components diffusion flame used in this experiment, the total refractivity variation caused by the changes of temperature and composition can therefore be written by substituting Equation 3.6.5 into 3.5.8. we have

$$\delta = \left[f\delta_a + (1-f)\delta_b \right] T_0 / T \qquad (3.6.9)$$

where f is the volume fraction of gas a.

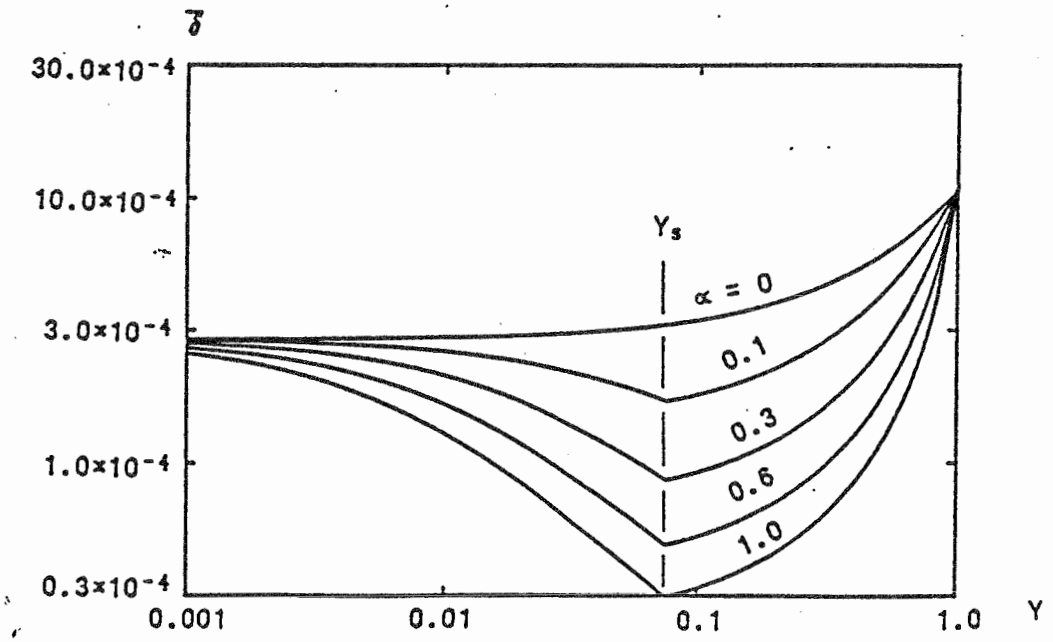

Figure 3.15 Variation of refractivity ($\bar{\delta}$) for coannular propane/air diffusion flame.
α = proportion of possible reaction which is completed,
Y_s = stoichiometric mass fraction.

The variations of refractivity index in association with the reacted fraction of combustible mixture are shown in Figure 3.15 for the coannular propane/air diffusion flame case. The parameter α is the proportion of the reactants available for

combustion which have reacted stoichiometrically. The mixture refractive index of each gaseous component was calculated from the molecular weight and density in terms of the Lorenz-Lorentz molar refractivity (Weinberg, 1963), and the overall refractive index was determined on a weighted basis for the mixture in proportion to the volume fraction of each component gas. It can be seen that in the absence of any reaction (α = 0) the refractive index increases monotonically with propane mass fraction, while increasing levels of reaction introduce a minimum refractive index at the stoichiometric ratio when temperatures of the resulting mixture are the highest and density the lowest. The refractive index variation is dominated by the temperature effect (Equation 3.6.9) which is the strongest at the stoichiometric fuel mass fraction (Y_s). For mixing reactions which are complete and determined only by the fuel mass fraction (Y_s) attained, the refractive index represents a variable which indicates the progress of reaction in the mixture as mixing proceeds either on the lean or rich side of stoichiometric. We thus expect the refractive index to be related to the local mixing progress within a turbulent combustion zone.

By relating the refractive index fluctuations directly to the density disturbance, the crossed beam schlieren technique has been developed to resolve the turbulent density field, integral scale and convection speed satisfactorily, especially for high Reynolds number flows (Wilson, 1970; Davis, 1971, 1972, 1975, 1993; Winarto, 1984).

3.7 Concluding discussion

Figures 3.11~3.14 show the comparison of the refractive index contour diagram obtained from the axial and transverse signal of schlieren system. The results of the measurements and computation at the low excitation frequency and high frequency are shown for two locations of the measuring system at approximately 6 and 12 times inner nozzle diameters from the nozzle exit. The physical scale of the disturbances is much larger at low frequency, compared with high frequency, the outer train of ringlike structures having a diameter 3.25 times the inner nozzle diameter or 1.15 times the outer nozzle outer diameter. Clearly these outer ring structures are centred on the shear layer between the outer (air) flow and the surrounding ambient air. The axial scale of the disturbances is also much larger, the periodic length begins 5.2 times the outer nozzle outer diameter or 7.5 times the inner fuel nozzle diameter. The results show a tendency for axial length to increase and diameter to decrease with distance from the nozzle exit. These outer structures have alternating maximum and minimum

refractive index, the range of variation diminishing sharply from ±0.00017 at 6 inner nozzle diameters from the nozzle exit to ±0.0004 at 12 inner nozzle diameters from the nozzle exit. This represents a reduction from ±12% to ±3% of the refractive index differential between the propane fuel and that of a fully reacted stoichiometric mixture. These disturbances are strong but within the range limitation set by the extremes of the refractive index of fuel and stoichiometric reacted mixture. The rapid reduction of the observed strength of the disturbance with distance from the nozzle is consistent with the initial formation of very regular ring-like structures which undergo rapid distortion and fragmentation as they move downstream. Observing the inner ringlike structures which are induced in the outer shear layer by the lower frequency excitation, we can also identify evidence of an inner chain of disturbances on the flow axis (Figures 3.11 and 3.12). Owing to some residual noise in the averaged signal records (Figures 2.6 and 2.8) near the flow axis which appears to be associated with the inner flow mixing structures as discussed, the transverse deflection results gave erratic results at the inner position (x/di = 6) near to the nozzle. However the axial deflection records and all results at the outer position (x/di = 12) were not subject to this problem, and the inner structures were fairly clearly resolved (Figures 3.11 and 3.12). The inner structures have the same axial length scale as the outer structures and are also of alternating sign but in the opposite sense to the sign of the outer structures at the same axial position. There is a tendency for the inner disturbances (of opposite sign) to precede the outer structures very slightly in all cases. Nearer to the nozzle (x/di = 6) the strength of inner and outer disturbances was similar, but further away from the nozzle exit (x/di = 12) the outer structures weakened more rapidly and the inner structures were then somewhat stronger. The form of the inner structures was of alternating sign, there being no evidence of a ringlike form but rather a form with a maximum disturbance strength on the flow axis.

There are quite different conditions at the higher excitation frequency (Figures 2.13 and 2.14). As mentioned before, the physical scale of the disturbances is much less than in the low frequency, the outer train of ringlike structures only have a diameter similar to the inner nozzle diameter. These outer ring structures are actually quite similar to those observed under low frequency excitation. The axial scale of the disturbances is however less, but the periodic length is still approximately equal to the inner fuel nozzle diameter. The disturbances obtained from axial and transverse results appear to have somewhat different structure and magnitude at 6 inner nozzle diameters from the nozzle exit (Figure 2.13) but quite similar form at 11.67 inner

nozzle diameters from the nozzle exit (Figure 2.14). The probable reason for this difference is discussed below.

(A). The diffusion flame and flow is not truly axi-symmetric: The Abel transform is based on the axi-symmetry of the diffusion flame and flow. However, the evidence shows the flow is not truly axi-symmetric. Figure 2.5 shows that the excitation signals are not symmetric for both low and high frequency excitation due to the error of the signal generator. The variations of the signal are -0.12~0.11 (V) at low frequency and -0.5~0.42 (V) at high frequency. These excitation signal errors will ultimately influence the laser beam signals (Figures 2.6~9) as also will asymmetric acoustic effects associated with the nozzle and feed pipe system. Theoretically, the radial laser deflection signal at exit nozzle centre position (R35.00, R70.00, R35.00 and R70.000) should equate to zero. However the situation at the downstream position (x/d = 11.6, Figures 2.7 and 2.9) shows that R70.00 and R70.000 are unsymmetrical. This is due to the fact that the flow does not keep its symmetric character as it moves downstream. Close to the nozzle (x/d = 5.8), Figure 2.6 shows that R35.00 has a maximum of about 15% of the A35.00 maximum signal and Figure 2.8 also shows that R35.000 has almost 25% of A35.000 magnitude error signal. According to the results of Table 3.3.3, the noise error amplification factor A_i^k at the centre of nozzle (i = 1) is almost 2.5 times greater than at other positions. This will significantly influence the Abel transform results for radial direction and indicates that the asymmetry indicated by the non-zero radial deflections on the axis will lead to significant discrepancies in the final results due to this effect.

(B). The resolution accuracy of measurements: At high excitation frequency, there are 12 points measurements on a 6 mm range (0.5 mm steps). Considering that the laser beam has a 0.8 mm thickness and the distance from the nozzle centre was measured by a traverse scale, the errors due to measurement resolution will certainly be expected to affect the results of refractive index distribution which are deduced. Obviously, to overcome these problems, further improvement of analysis at high frequency is required to be achieved by using a higher resolution laser position determination, high quality signal generator and probably most importantly, careful design to eliminate acoustic asymmetry from the excitation obtained near the nozzle.

Chapter 4 THE FRACTAL CHARACTER OF TURBULENT SCHLIEREN IMAGES

4.1 Introduction to fractal analysis

The mathematics of fractals is a broad subject which has been developed in recent years, primarily by Mandelbrot (1983). In the last decade interest in the subject has grown rapidly and many diverse applications have been found (Batty, 1985). A primary motivation in the development of fractals has been the desire to provide tools for a geometric, statistical description of highly contorted and roughened surfaces and curves (Mandelbrot, 1983).

The introduction of fractals relates to the now classic question (Mandelbrot, 1983): how long is the coastline of Great Britain? Since the coastline is rough on any practical measurement scale, it is found that the length of the coastline depends upon the measurement scale and tends to be infinity as the measurement scale approaches zero. To perform this measurement imagine the island of Great Britain to be inscribed at sea level by a polygon of N sides of equal length ε. Then the coastline length is $N\varepsilon$, a quantity which in practice is found to increase as ε decreases. The reason for this odd behaviour is that for any ε considered the coastline is, on that scale, rough, and thus the polygon is never an accurate representation of the coastline.

In addition, it is found that when the measured lengths are plotted versus ε on a log-log scale a straight line results. Fractal character thus exhibits two distinctive features: (1) the measured length of a curve (or the area of a surface) depends on the measurement scale and (2) this is in accordance with a power law dependence, ε^{1-D} for curves (and ε^{2-D} for surfaces). D represents the fractal dimension and is non integer for a fractal curve or surface, while for a smooth curve $D = 1$ and for a smooth surface $D = 2$.

More germane than a curve to the combustion problem is the fractal character of a surface or dimensional field in the turbulent flow. Mandelbrot (1975) considered a constant property surface (e.g. an isothermal surface) in homogeneous, isotropic

turbulence. To define fractal character in this context Mandelbrot considers a volume, L^3, filled uniformly (in a statistical sense) with a wrinkled, roughened surface, the scales of wrinkling being self-similar. If the volume L^3 is split into cubic cells of side ε, on average the number of cells touched by the surface is proportional to $(L/\varepsilon)^D$. If the surface is smooth the fractal dimension, D, will approach 2; while if it is rough, D will approach 3 and the surface will appear to fill the volume in L^3. Thus the surface area A in L^3 measured with a scale ε^2 is given by

$$A \sim \varepsilon^{2-D} L^D \qquad (4.1.1)$$

The measured surface area behaviour given by Equation 4.1.1 is fractal because (1) the measured area depends on ε and (2) this dependence is given by a power law. The variation in measured A is due to surface roughness, while the regularity of this variation can be quite attributed to the self-similarity of the scales of surface roughness.

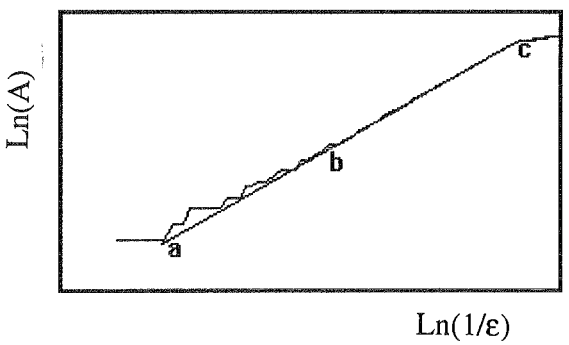

Figure 4.1 The fractal behaviour of surface.

Due to molecular diffusion and dissipation at small scales one would expect there to be a minimum scale below which fractal behaviour is suppressed and, intuitively, that as ε approaches zero A approaches a finite limit (c in Figure 4.1). An appropriate length for this minimum scale or inner cutoff would appear to be the Batchelor length scale or the Kolmogorov scale, η, if the Prandtl or Schmidt number is one. Similarly, if there is a maximum length scale of surface wrinkling, i.e. the turbulence integral scale l, which is less than L, one would expect A to be independent of ε if ε is greater than this maximum scale (a in Figure 4.1). The possible presence of upper and lower

bounds to fractal behaviour of the surface is recognised by Mandelbrot (1983), who referred to them as inner and outer cutoffs (Figure 4.1, c and b). Later the limits of fractal behaviour were observed by Sreenivasan and Meneveau (1986) and were found to be equal approximately to η and l.

It is important to emphasise that A in Equation 4.1.1 is the measured surface area and not the actual surface area. If the surface is rough on all possible scales including the molecular scale, then the surface area is undefined. If there is an inner cutoff, then the surface area exists and is defined as the limit of the measured area as ε approaches zero. The value of this limit is given, to within a multiplicative constant, by Equation 4.1.1 with ε = inner cutoff.

Mandelbrot (1975) suggested two possible values for the fractal dimension of turbulence: $D = 2\frac{2}{3}$ for Gauss-Kolmogorov turbulence or $D = 2\frac{1}{2}$ for Gauss-Bergers turbulence. Mandelbrot's results (1975) were based on statistical arguments and the assumption of Gaussian random fields. During the 1980s the fractal character of homogeneous turbulence was studied by the measurement of fractal dimension of clouds (Lovejoy, 1982) and by the analysis of turbulent dispersion (Herntschel and Procaccia, 1984), Both studies suggest a fractal dimension of approximately 2.35~2.40. In addition, the measurements in turbulent shear flows indicate that the constant property surface in the flows is fractal with a D between 2.35~2.6 (Sreenivasan and Meneveau, 1986). However, Takeno and Murayama (1990) studied the fractal dimension of premixed flames which were visualised by a laser tomography technique. They found that the flame surface does exhibit a self-similarity behaviour and the fractal dimension depends on the orientation of the flame section but with a magnitude 2.12~2.26, significantly less than observed for turbulent mixing fields.

A variety of analysis methods are available for determining the fractal parameters from digitized flame images. Among them are the box counting method and the circle method (Mandelbrot, 1982). Although they are equivalent and ideally will give the same results, the box counting method is more convenient and has been used in this investigation. The formal definition of box counting method is based on the Box Counting Theorem (Barnsley, 1988.): Let $A \in \Re(R^m)$, where R^m is an Euclidean metric space and $\Re(R^m)$ denotes the space whose points are the compact subsets of R^m. Cover R^m by just touching closely the square boxes of side length ($1/2^n$). Let

$N_n(A)$ denote the number of boxes of side length ($1/2^n$) which intersects the fixed point $A \in \Re(R^m)$. If

$$D = \underset{n\to\infty}{Lim}\left\{\frac{ln(N_n(A))}{ln(2^n)}\right\} \qquad (4.1.2)$$

then A has a fractal dimension D. Equation 4.1.2 will be the basis of fractal calculation in this thesis.

4.2 Analysis of the fractal dimension of schlieren images

The aim of this chapter is to analyse the fractal dimension distribution of turbulent images and to establish the fractal relationship between the turbulent flow density field and its schlieren image. The first target can be achieved by using the box counting method to calculate the fractal dimension of diffusion flame images under different flow conditions. Since it is difficult to find a general function to identically represent the flame field, the second target only can be achieved by a numerical simulation method based on a variety of simulated fields. There is in fact no general relation between the fractal dimension of the schlieren image and that of the original three dimensional field, and therefore numerical simulation of the represented field can only provide a general indication of this relation.

The flame images used for fractal analysis are grabbed by the *PIP* system (as described in Chapter 2). The images are then digitized by *PIP* to give 512 x 512 pixel images with 256 gray scales of light intensity resulting in horizontal and vertical resolutions of 0.4 and 0.33 mm/pixel respectively and are stored as text file which consists of a series of ASCII integers separated by spaces. The first four entries in each file describe the co-ordinates of the image space (*x1, y1, x2, y2*). Following the co-ordinates are the pixel values read in the order from left to right and top to bottom. This ASCII data is portable and can be processed in any computer.

Figure 4.2 shows the turbulent flow image being used to estimate the fractal dimension. To begin the fractal analysis, we select a rectangular area (window) within the image. The marked scale (pixel) in Figure 4.2 is used to show the size and position

of the window. The marked values (1, 2, 3.....) represent the position of the window centre. The greater the value, the closer the centre is to the flow nozzle (the nozzle is at 485 pixel height). Both the height and width of the window are symmetrical to the centre of the window. The determination of the fractal dimension of the turbulent flame images firstly requires that we perform box counting on the selected image area. Considering the light intensity of the image in this area to be a surface in space, the image element and light intensity can be combined to form an incremental volume.

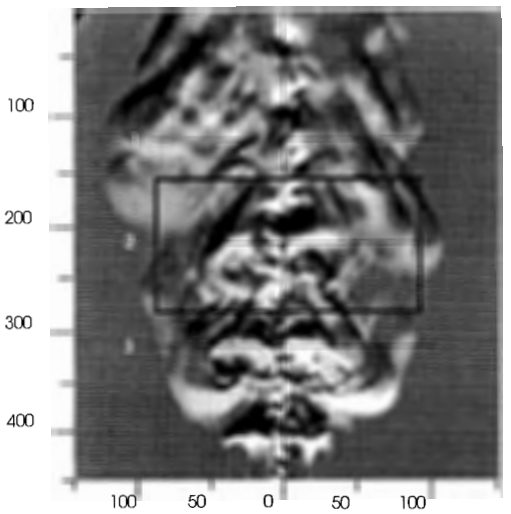

Figure 4.2 The turbulent images and work window used for fractal analysis. No excitation natural diffusion flame (Velocity of gas = 2.5 m/s, Velocity of air = 2 m/s). The work window has 180 pixel width and 120 pixel height and been located at centre position 2 (1 pixel equal 0.37 mm in horizontal direction and 0.27 mm in vertical direction of flame size).

If we place a cube box of side size ε to fill the total space, then the space volume $V(\varepsilon)$ can be measured by counting the number of boxes $N(\varepsilon)$ in the space, which is

$$V(\varepsilon) = N(\varepsilon)\varepsilon^3 \qquad (4.2.1)$$

Repeating the process with varying ε we determine the variation of $N(\varepsilon)$ with respect to ε. If the image is a fractal object, $V(\varepsilon)$ will increase with decreasing ε according to the relation

$$N(\varepsilon) = K\varepsilon^{-D_3} \qquad (4.2.2)$$

or

$$LogN(\varepsilon) = \log K - D_3 \cdot \log \varepsilon \qquad (4.2.3)$$

where K is a constant. Thus the fractal dimension of image D_3 can be determined by finding the slope between two points (an inner cutoff point and an outer cutoff point) on the curve that is the log of the inverse box size versus the log of the box counting numbers (Figure 4.3). In the present study more than 24 values of ε (box size) were used for each image to deduce D_3 by finding the regression line through these data points by the method of least squares. The outer cutoff corresponds to the bigger box size limit and the inner cutoff to the smaller box size limit.

As mentioned earlier, the outer cutoff and inner cutoff generally correspond to the integral scale (or flame size) and the Kolmogorov scale respectively. In our situation the three sides of the cube (box) which is used to calculate the fractal dimension represent three different factors: one is the horizontal direction of the monitor (from 1 to 512 pixels, one pixel being equal to 0.4 mm), the second is the vertical direction of the monitor (from 1 to 512 pixels, one pixel being equal to 0.33 mm) and the third represents the light intensity (from 1 to 255, 1 representing dark and 255 representing white). The physical size of flame and the size of image window play an important role in the determination of the outer cutoff and the inner cutoff, but the contrast of light intensity which is mainly affected by flow properties (temperature, pressure and density) also influences the selection of two cutoff points.

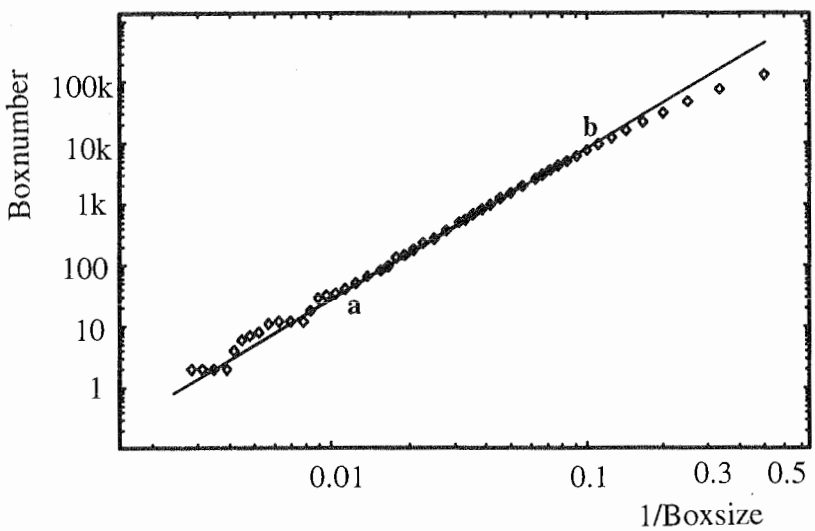

Figure 4.3 Fractal analysis result of image shown in Figure 4.2.

Figure 4.3 shows a typical fractal analysis result of the diffusion flame schlieren images. The box counting in three dimensions produced a straight region between a and b in the log-log plot. According to equation 4.1.1, this suggests that the schlieren image of diffusion flames do exhibit fractal character in the region. The slope of

straight line gives a fractal dimension of D_3=2.37 to the schlieren image. The inner cutoff b of D_3 is around box size of 8 which corresponds to 3.6 mm on the horizontal flow scale, 2.7 mm on the vertical flow scale and 3% of the light intensity. The inner cutoff is one order of magnitude larger than η. The outer cutoff a is strongly linked to the window and flame size: when the window is smaller than the flame size, the outer cutoff usually is the shorter side of the window. If the size of the window work area is bigger than the flame, then the outer cutoff is limited to the flame size (about 125 pixel, which corresponds to 46 mm in the horizontal, 34 mm in the vertical and 50% of the light intensity). Therefore, we may say that the cutoff scales in this experiment were determined by the Kolmogorov scale and the burner size.

The standard variance in the fractal dimension calculation can be used to give an indication of the accuracy of the results. The degree of deviation from the regression line may be represented by standard deviation c, defined by

$$c = \left[\frac{1}{n} \sum_{i=1}^{n} \left\{ L_i - (A + B \log \varepsilon_i) \right\}^2 \right]^{1/2} \qquad (4.2.4)$$

where n = 24~44 is the number of points depending on the size of the window, and A and B are constants. The deviation c can represent a simple measurement of the fractal degree. If c is zero, every point is exactly on the line, and we may think that the data exhibit truly fractal character in the given scale range. In this investigation, all the fractal dimensions were thus evaluated with a higher than 0.95 correlation and less than 0.1 variance by adjustment of the cutoff point. The box counting method has been calibrated by calculating the fractal dimension of white images. The calculated values for uniform white images give a fractal dimension varying from 1.97~2.04. This demonstrates that the adopted method of analysing the fractal character of diffusion flame images has a standard deviation of 0.04.

For comparison, we can also use another fractal dimension calculation method which measures the length of a curve border to obtain the fractal dimension. This is explained as follows: give a threshold to the image and at each pixel of the image if the light intensity is less than the threshold set it to dark, otherwise set it to white. Now a border between the dark and white appears as shown in Figure 4.4.b. The length of the border $L(\varepsilon)$

$$L(\varepsilon) = N(\varepsilon)\varepsilon \qquad (4.2.5)$$

where the ε is the length scale used to measure the border and $N(\varepsilon)$ is the count number which is required to cover the whole border. If the image is a fractal object, $L(\varepsilon)$ will increase with decreasing ε according to the relation

$$N(\varepsilon) = K\varepsilon^{-D_2} \qquad (4.2.6)$$

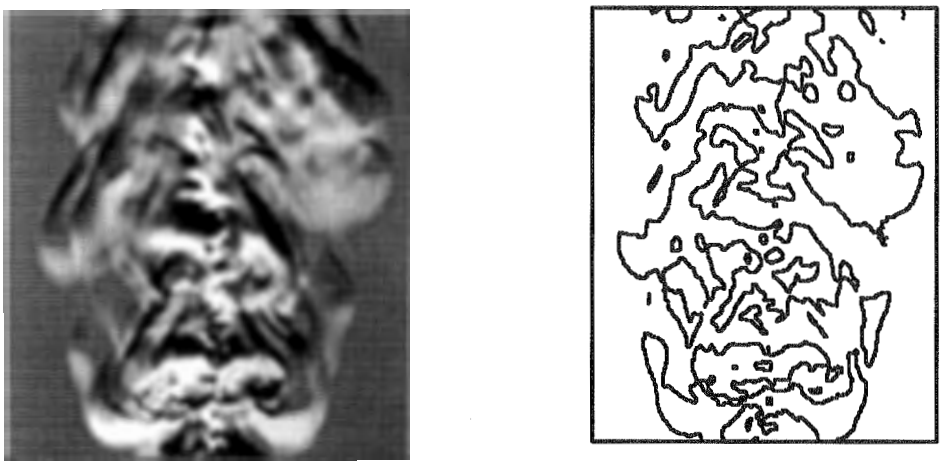

(a) (b)

Figure 4.4 The diffusion flame image and it's image threshold border.

The fractal dimension of image D_2 can be determined by the regression line which is the log of the inverse box size versus the log of the box counting numbers (similar to the method to obtain D_3). According to Mandelbrot (1983), D_2 should be one less than D_3. In Figure 4.4, D_2 = 1.32, and for the same image D_3 = 2.35. The two methods have a good corresponding result within the expected deviation range. This demonstrates that the fractal dimension calculation procedure is quite reliable. The border method can only be used to calculate for an image which has adequate size and an obvious border (e.g. a whole flame image). The box counting method can be used for all sorts of images and image segments.

4.3 Spectral analysis of fractal images

In addition to the fractal dimension analysis of turbulent images, we may also estimate the power-spectral-density of turbulent images. Pentlad (1984) considered the image intensity surface as a fractal Brownian function (*fBf*) and estimated the fractal dimension from Fourier Power Spectrum Density (*PSD*) of *fBf*. The *PSD* is a nonegative function of frequency and gives an estimate of mean square fluctuations at frequency *f*. Consequently the variations are described over a time scale of order *1/f*.

According to Peitgen (1988) there is a direct relationship between the fractal dimension of *fBf* and the logarithmic slope of the *PSD*. The connection between three equivalent characteristics, *D*, *H*, and β, of an *fBf* function with an Eulerian space dimension E is given as below

$$D = E + 1 - H = E + \frac{3-\beta}{2} \qquad (4.3.1)$$

The fractal dimension *D* lies in the range $E<D<E+1$, and β is the slope of the log of inverse frequency *f* versus the log of the *PSD* curve in the range $1<\beta<3$. *H* is a special parameter. The scaling behaviour of the different images is characterised by the parameter *H* in the range $0<H<1$. When *H* is close to 0 the traces are the roughest while those with *H* close to 1 they are relatively quite smooth.

The *PSD* of images are estimated by averaging the *PSD* of each pixel line in the image field. The reason for this primarily relates to the reduced numerical calculation required as a two dimensional spectral estimation would require a much more complicated numerical calculation than this one dimensional spectral average estimation.

The random functions in time $X(t)$ are often characterised by their spectral densities $P_x(f)$. Given a random function *X(t),* which is random variable of time (*t*) in a finite time interval $0 < t < T$, $X(t,T) = X(t)$, otherwise $X(t)=0$, thus we have

$$X(t,T) = \int_{-\infty}^{\infty} F(f,T) e^{2\pi i f t} df \qquad (4.3.2)$$

where *F(f,T)* is the Fourier transform of *X(t,T)*

$$F(f,T) = \int_0^T X(t) e^{-2\pi i f t} dt \qquad (4.3.3)$$

Now $|F(f,T)|^2 df$ is the contribution to the total energy of $X(t,T)$ from those components with frequencies between *f* and *f+df*. The average power of *X(t)* contained in the interval [0, *T*] is then given by

$$\frac{1}{T}\int_{-\infty}^{\infty} |F(f,T)|^2 df \qquad (4.3.4)$$

and the power spectrum density of $X(t,T)$ is

$$P(f) = \lim_{T\to\infty} \frac{1}{T} |F(f,T)|^2 \qquad (4.3.5)$$

During the Fourier transform *X(t)* is being decomposed into a sum of infinitely many sine and cosine terms of frequencies *f* whose powers (and amplitudes) are determined by the spectral density $P(f)$. The interpretation of $P(f)$ is as follows: $P(f)df$ is an average of the contribution to the total power from components in *X(t)* with frequencies between *f* and *f+df*. $P(f)$ is a nonegative and even function. If the random function *X(t)* contains equal power for all frequencies *f*, this process is termed white noise by analogy with the white light made up of radiation of all wave lengths. If $P(f)$ is proportional to $1/f^2$ it is termed *X(t)* Brown noise or Brownian motion. In general, a process *X(t)* with a *PSD* proportional to $1/f^{\beta}$ corresponds to *fBf* with $H = \frac{\beta - 1}{2}$. Choosing β between 1 and 3 will generate a graph of *fBf* with a fractal dimension (Peitgen, 1988) of:

$$D_f = 2 - H = \frac{5 - \beta}{2} \qquad (4.3.6)$$

It is one task of this thesis to check if Equation 4.3.6 (or Equation 4.3.1) exists in diffusion flame images.

In the practical algorithm, the *PSD* of *X(t)* can be obtained by Parseval's Theorem (William *et al.*, 1989). Suppose that the function *x(t)* is sampled at *N* points to produce values $x_0 \ldots x_{N-1}$, and that these points span a range of time *T*, that is $T = (N-1)\Delta$, where Δ is the sampling interval. The Power Spectrum Density can be estimated by the periodogram method. If we take an *N*-point sample of the function *x(t)* at equal intervals and use the *FFT* to compute its discrete Fourier transform, then we have

$$D_k \equiv \sum_{j=0}^{N-1} x_j w_j e^{2\pi ijk/N} \qquad k = 0, \ldots, N\text{-}1 \qquad (4.3.7)$$

where w_j is a window function, that is "Parzen window",

$$w_j = 1 - \left| \frac{j - \frac{1}{2}(N-1)}{\frac{1}{2}(N+1)} \right| \qquad (4.3.8)$$

Thus the Power Spectrum Density $P(f_k)$ is defined at $N/2+1$ frequencies as

$$P(0) = P(f_0) = \frac{1}{W_{ss}}|D_0|^2$$

$$P(f_k) = \frac{1}{W_{ss}}\left[|D_k|^2 + |D_{N-k}|^2\right]^2 \qquad k = 1, 2, \ldots, \left(\frac{N}{2} - 1\right)$$

$$P(f_{N/2}) = \frac{1}{W_{ss}}|D_{N/2}|^2 \qquad (4.3.9)$$

where W_{ss} stands for "window squared and summed,"

$$W_{ss} \equiv N\sum_{j=0}^{N} w_j^2 \qquad (4.3.10)$$

Using Parseval's theorem, Equation 4.3.9 is normalised so that the sum of $N/2+1$ value of P is equal to the mean squared amplitude of the function x_j.

Before performing any spectral analysis, we should first set the window length L to suit the characteristics of the signal under analysis. The primary purpose of the window in the time-dependent Fourier transform is to limit the extent of sequence to be transformed so that the spectral characteristics are reasonably stationary over the duration of the window. The more rapidly the signal characteristics change, the shorter the window should be. As the window becomes shorter, frequency resolution decreases. On the other hand, as the window length increases, the ability to resolve gradual changes with time increases. Consequently, the choice of window length becomes a tradeoff between frequency resolution and gradual time change resolution. According to Oppenheim (1989), the spectral estimate fluctuates more rapidly as the window length L increases. For large L, the periodogram estimate tends to vary rapidly with the frequency. We would prefer to obtain a smooth spectrum estimate without random variations resulting from the estimation process. To reduce the variability while keeping the record length constant, we can use shorter windows and average over more sections. As more sections are used, the variance of the spectral estimate decreases. But so does the amplitude of the peak due to the cosine. If the length is any shorter, spectral leakage from the negative frequency component would cause no distinct peak in the low-frequency region. Our data length is in the range 320~512 for which the window length L = 32 or 64 (64 used in the thesis) is generally

a good choice (Oppenheim, 1989). The *PSD* distribution of various images will be shown and discussed in a latter part of chapter.

4.4 The relationship between the fractal dimension of the image field and its derivative field and the line integrated function

Due to the difficulty in making direct measurements of the fractal dimension of real turbulent flow, the investigation of fractal dimension of turbulent density is achieved by observing its schlieren image. However, we must now consider what is the corresponding fractal dimension in the actual diffusion flame field. This question is approached by using a numerical simulation to establish the fractal relationship between the turbulent flow and its schlieren image. It must be realised that there is no simple universal relation between the fractal dimension of the schlieren image and that of the actual spatial field which gave rise to the image. This can be illustrated by considering two simple cases where differentiation (which is essentially the function of the density field derived by the schlieren system) is applied. For a simple sinusoidal numerical field, differentiation merely produces a phase shift but with no consequent change in fractal or spectral character of the result. However, for broad band random field differentiation will modify the spectral character by increasing the relative magnitude of higher frequency components of the spectrum with a consequent change of the fractal dimension of the differentiated field by comparison with the original field according to Equation 4.3.1 or similar (Peitgen, 1986). From these two simple results we see that no simple general relation can exist between the fractal dimension of a function and that of its derivative. Therefore our approach is more pragmatic, that is to examine this and similar relationships for different types of function, including those of interest (i.e. turbulent mixing and combustion fields), in order to gain a better insight into the relationship between the fractal dimension of a schlieren image and that of the flow field which gave rise to the image. According to Equation 2.1.1, the relationship between the optical path and the refractive field is presented as

$$\theta = -\int \frac{1}{N}\frac{\partial N}{\partial \xi} d\eta \qquad (4.4.1)$$

Based on this and assuming the turbulent flow function over the x-y plane is $f(x,y)$, then we have its derivative function in x direction as

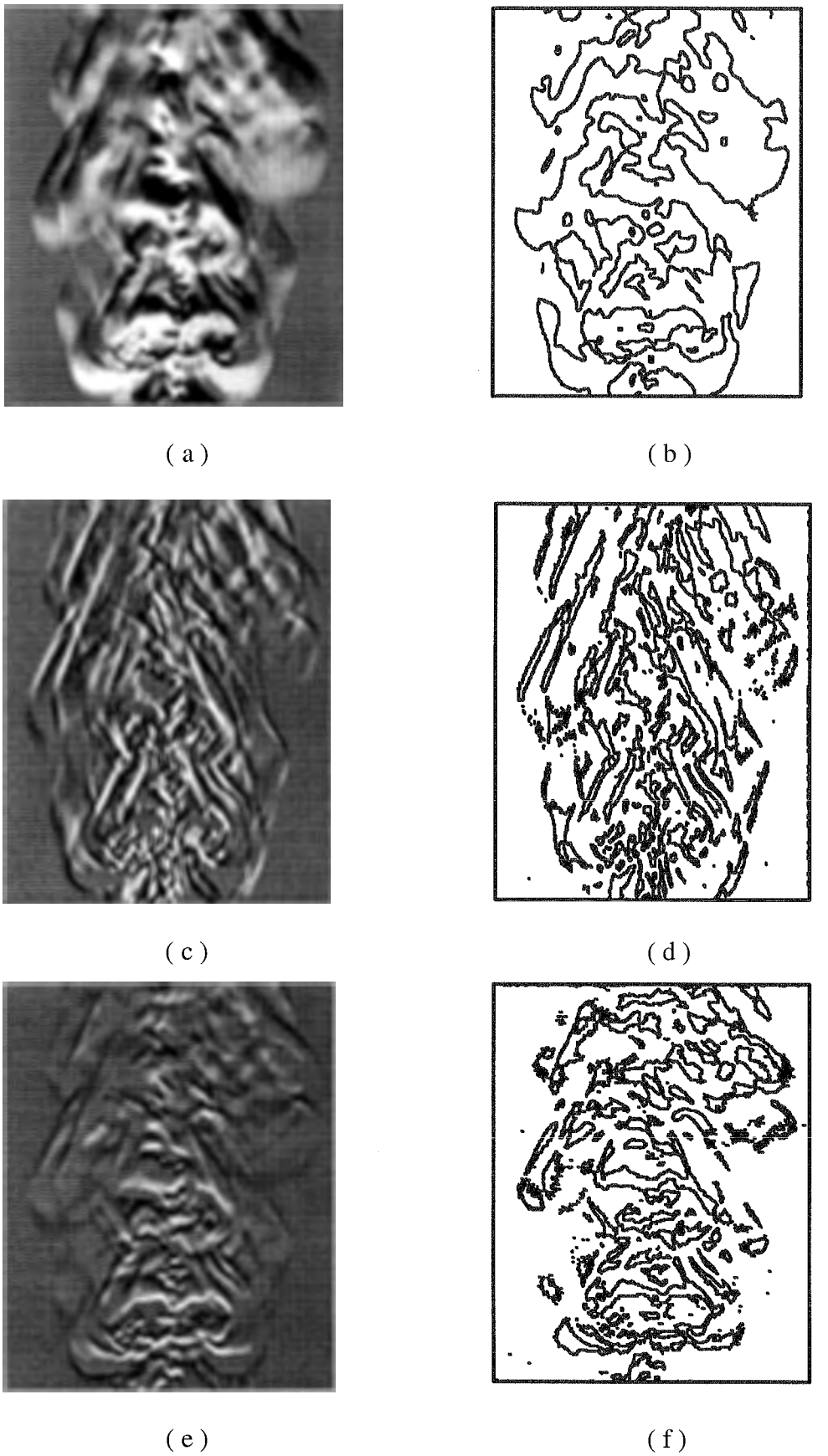

Figure 4.5 The diffusion flame image and the image threshold border.
(a) flame image (V_a=2.0 m/s, V_f=2.5 m/s, no excitation). (b) border for (a).
(c) derivative image (x direction). (d) border for (c).
(e) derivative image (y direction). (f) border for (e).

$$DX(x, y) = \frac{df(x, y)}{dx} \tag{4.4.2}$$

The resulting schlieren image function *IX(x)* can be obtained by Equation (4.4.1)

$$IX(x) = \int DX(x, y)dy \tag{4.4.3}$$

Similarly in the y direction

$$DY(x, y) = \frac{df(x_i, y)}{dy} \tag{4.4.4}$$

and its consequent schlieren image function

$$IY(y) = \int DY(x, y)dx \tag{4.4.5}$$

The derivation of *f(x,y)* is estimated by differentiating along each pixel image line in the simulated field. Another reason for calculating the image PSD by averaging the one dimension PSD is that the effect of differentiation on the PSD as evaluated here can be investigated. Figure 4.5 shows (a) the original image, (b) its x differential and (c) its y differential. Both differential images show clear structures embedded in the diffusion flame. After calculating the fractal dimension of *f(x,y)*, *DX(x,y)*, *DY(x,y)*, *IX(x)* and *IY(y)*, the differences between them can be observed. Although *IX(x)* and *IY(y)* are one dimensional functions, their fractal dimension D_2 should be one less than the fractal dimension D_3 of the corresponding two dimensional images *DX(x,y)* and *DY(x,y)* (Mandelbrot, 1983).

Essentially we are investigating by numerical simulation the relationship between the fractal and spectral properties of a field and its schlieren image by considering a physical slice plane through the field and the consequent schlieren image along a single line in the image plane. Clearly this reduces the computational demand on computation considerably by comparison with evaluation of complete three dimensional field properties and the complete two dimensional flame image properties. However, using the result that the fractal dimension should in each case be reduced by one, this approach will give us the essential perspective on the relationship between the field and its schlieren image properties that we are seeking.

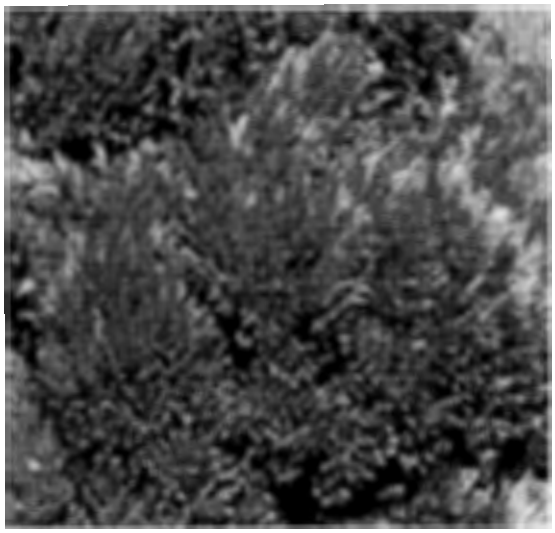

(a) leaves image

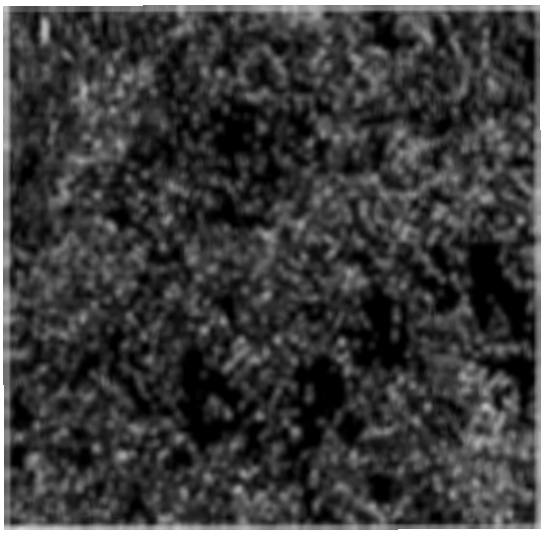

(b) leaves image

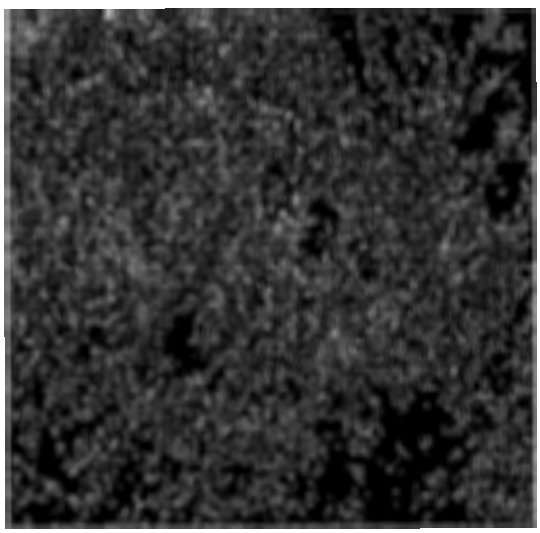

(c) leaves image

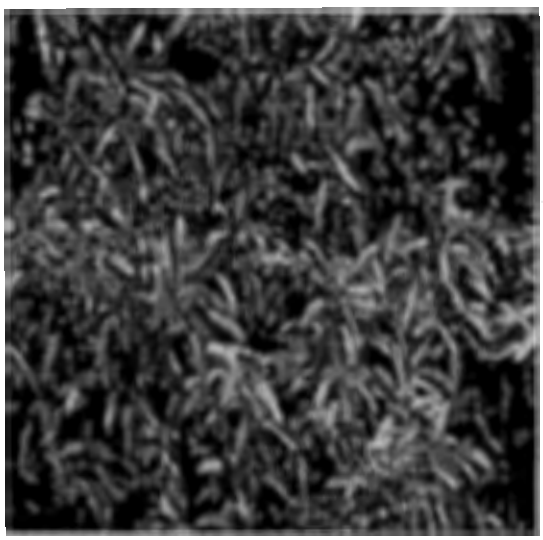

(d) leaves image

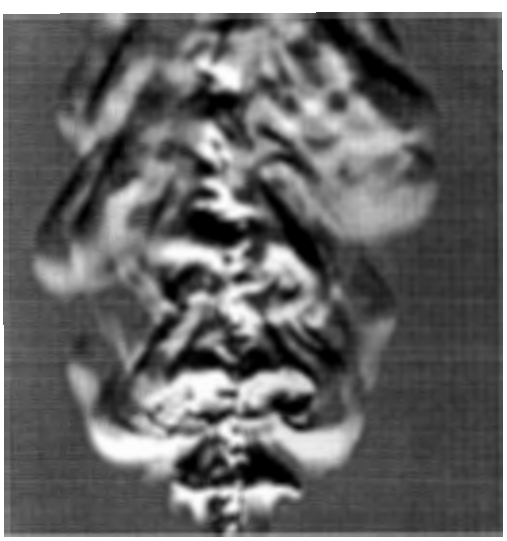

(e) flame image (no excitation)

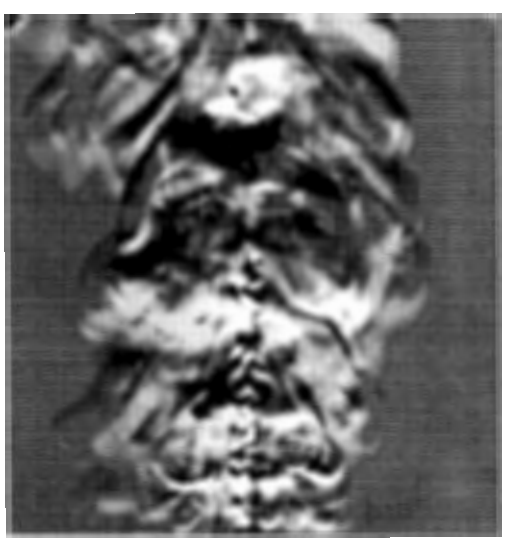

(f) flame image (40 Hz excitation)

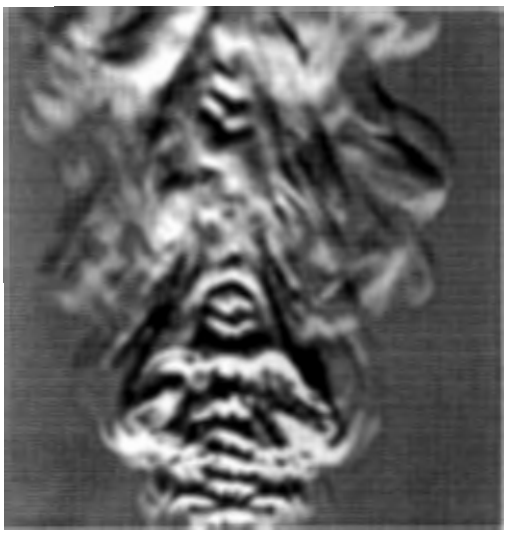

(g) flame image (420 Hz excitation)

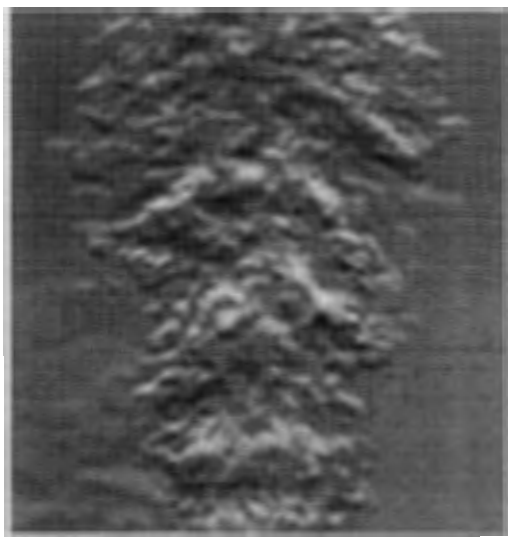

(h) heated jet image

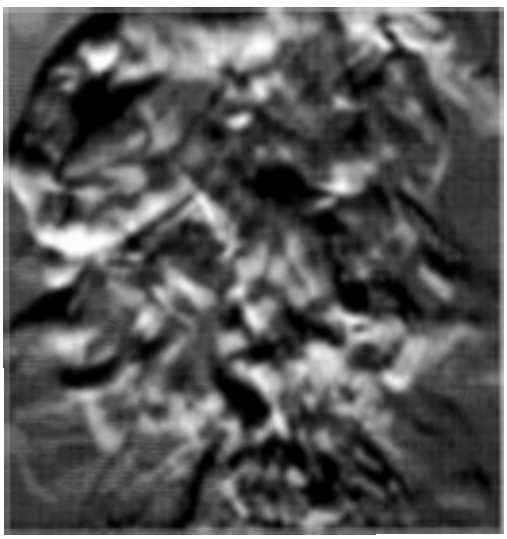

(i) more homogenous flame image

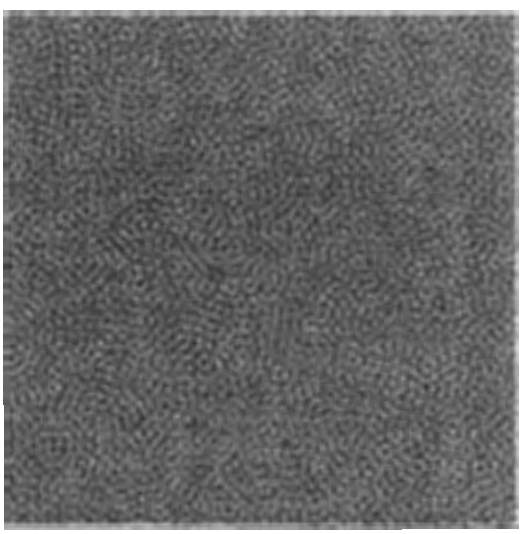

(j) band limited image $\Delta f/f = 0.4$

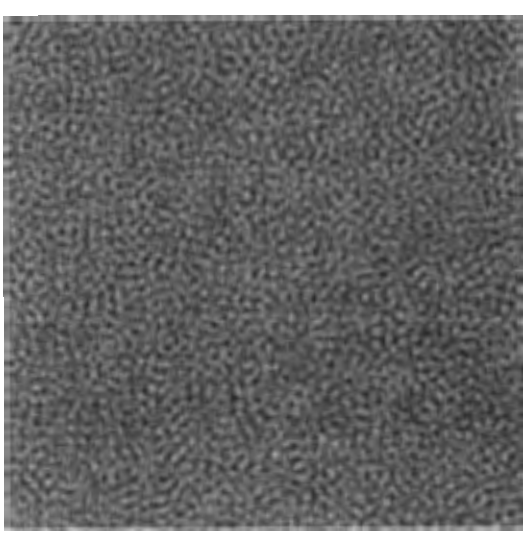

(k) band limited image $\Delta f/f = 0.8$

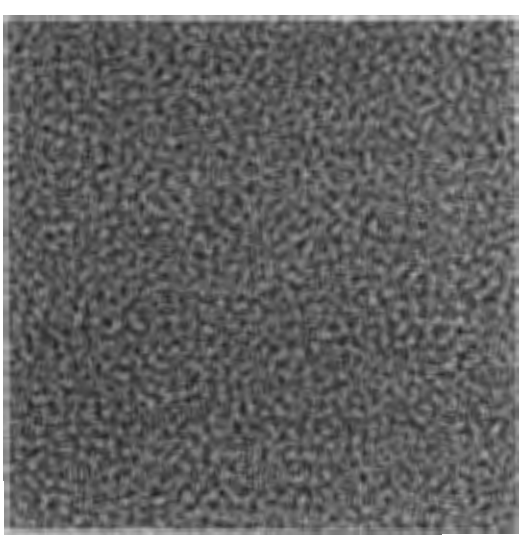

(l) band limited image $\Delta f/f = 1.2$

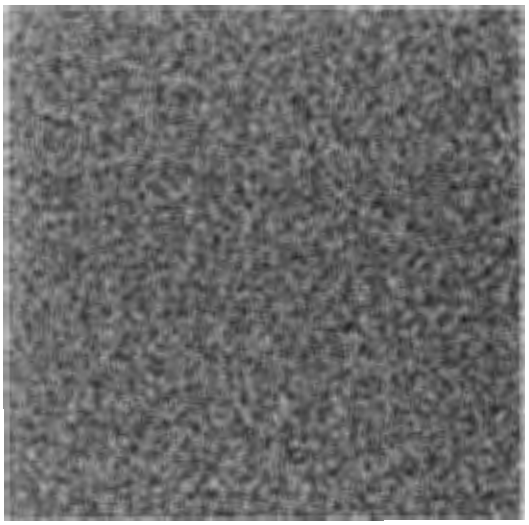

(m) band limited image $\Delta f/f = 1.8$

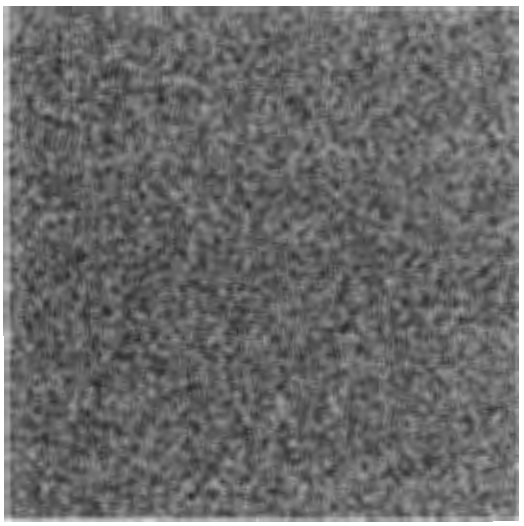

(n) band limited image $\Delta f/f = 1.93$

Figure 4.6 The images used as simulate turbulent flow.

Before any numerical processing is commenced (e.g. differentiation and integration) we must select appropriate functions to simulate the turbulent flow field. These should be continuous functions, otherwise it would be impossible to evaluate the relationship between the fractal dimension of turbulent flow density and its schlieren image. Secondly the function should be as homogenous as possible, and thirdly it should have suitable fractal and spectral character. In this analysis, the schlieren image of the turbulent flow, natural tree leaves and band limited random images have been used to simulate various types of random and turbulent flow image fields. To investigate the role of PSD on the fractal character, five random band limited images are introduced. The band limited images were generated by program BPIMAGE, which was written by Jumppanen (Department of Civil & Mechanical Engineering, University of Tasmania, 1994). These images are shown in Figure 4.6.

The experimental conditions for the images are shown as follow:

(1) Figure 4.6.a~d: Leaves images.
Camera speed = 1/1000 sec.

(2) Figure 4.6.e: Diffusion flame image.
Temperature of ambient air = $18^{o}C$
Gas nozzle diameter = 6 mm
Velocity of gas = 2.5 m/s
No excitation
Camera speed = 1/2000 sec.
Air nozzle diameter = 20 mm
Velocity of air = 2 m/s

(3) Figure 4.6.f: Diffusion flame image.

Temperature of ambient air = 20°C — Camera speed = 1/2000 sec.

Gas nozzle diameter = 6 mm — Air nozzle diameter = 20 mm

Excitation frequency = 40 Hz — Excitation strength = 0.125 V

Velocity of gas = 2.5 m/s — Velocity of air = 2 m/s

(4) Figure 4.6.g: Diffusion flame image.

Temperature of ambient air = 20°C — Camera speed = 1/2000 sec.

Gas nozzle diameter = 6 mm — Air nozzle diameter = 20 mm

Excitation frequency = 420 Hz — Excitation strength =0.679V

Velocity of furl = 2.5 m/s — Velocity of air = 2 m/s

(5) Figure 4.6.h: Hot jet image.

Temperature of ambient air = 19 °C — Re = 19000

Camera speed = 1/2000 sec. — Nozzle diameter = 20 mm

Temperature of heated gas = 55 °C — Temperature of unheated air = 15 °C

(6) Figure 4.6.i: Diffusion flame image.

Temperature of ambient air = 24 °C — Camera speed = 1/1000 sec.

Gas nozzle diameter = 6 mm — Air nozzle diameter = 20 mm

Velocity of gas = 3.7 m/s — Velocity of air = 2.5 m/s

Lower edge of image is 65 mm from nozzle — No excitation

(7) Figure 4.6.j: Band limited image.

Centre frequency $f = 15$ — Bandwidth ratio $\Delta f / f = 0.4$

(8) Figure 4.6.k: Band limited image.

Centre frequency $f = 15$ — Bandwidth ratio $\Delta f / f = 0.8$

(9) Figure 4.6.l: Band limited image.

Centre frequency $f = 15$ — Bandwidth ratio $\Delta f / f = 1.2$

(10) Figure 4.6.m: Band limited image.

Centre frequency $f = 15$ — Bandwidth ratio $\Delta f / f = 1.8$

(11) Figure 4.6.n: Band limited image.

Centre frequency $f = 15$ — Bandwidth ratio $\Delta f / f = 1.93$

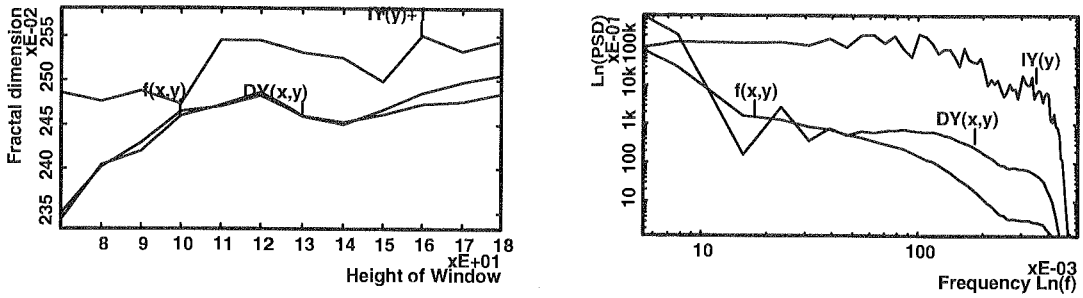

(a) from Figure 4.6.a

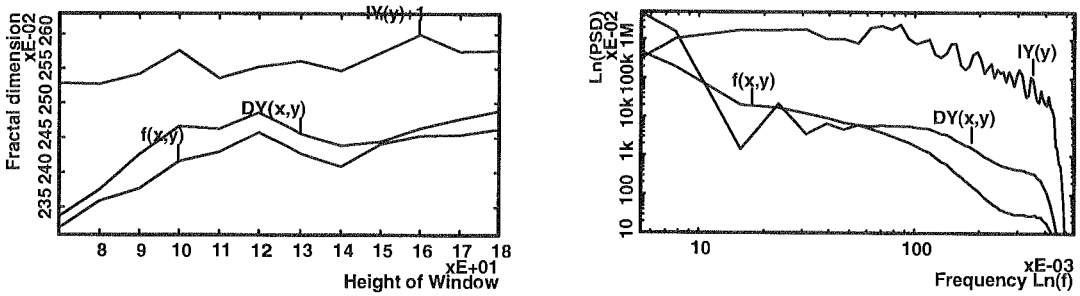

(b) from Figure 4.6.b

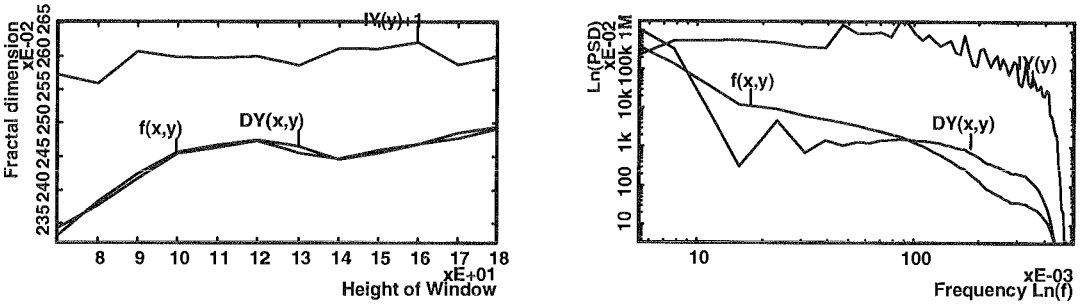

(c) from Figure 4.6.c

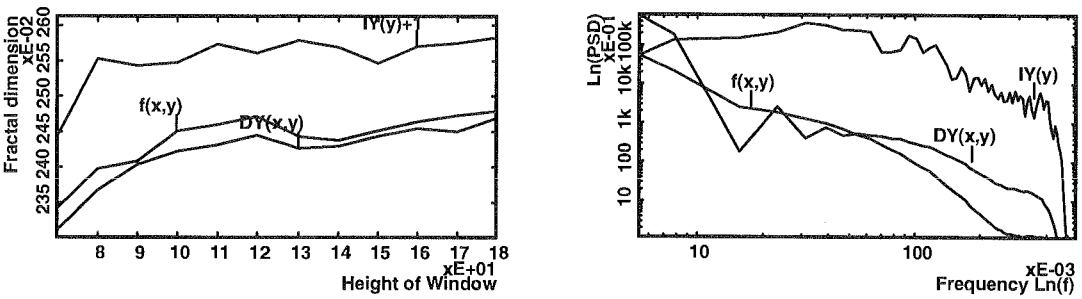

(d) from Figure 4.6.d

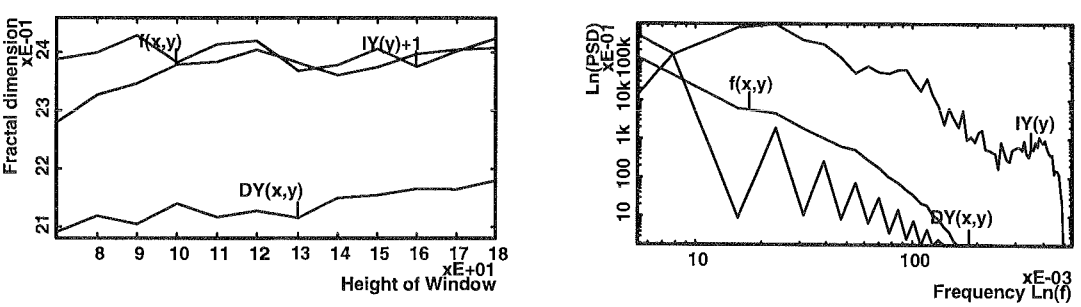

(e) from Figure 4.6.e

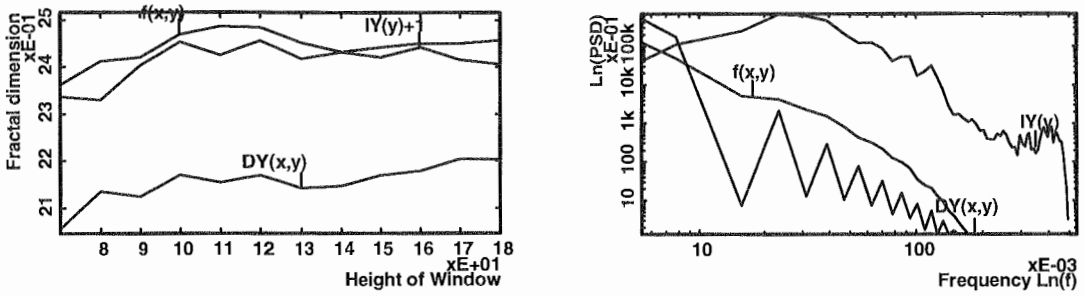

(f) from Figure 4.6.f

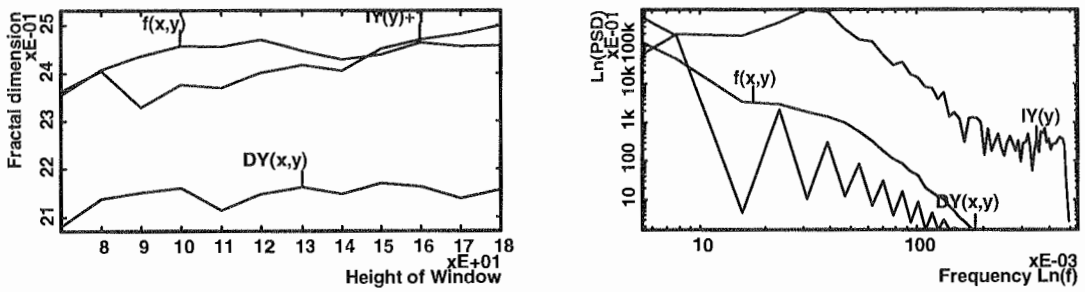

(g) from Figure 4.6.g

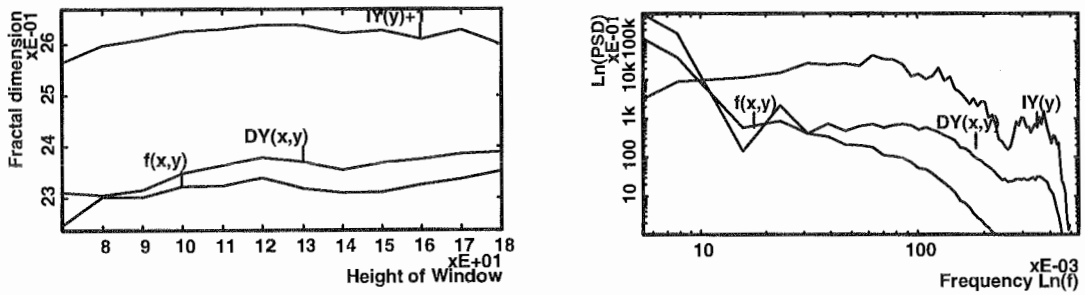

(h) from Figure 4.6.h

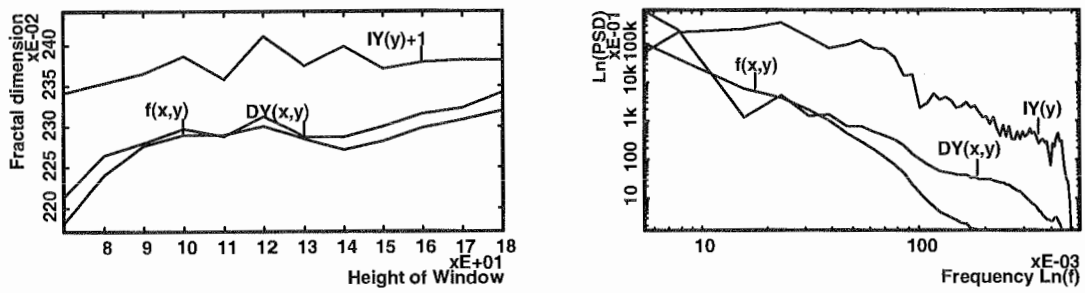

(i) from Figure 4.6.i

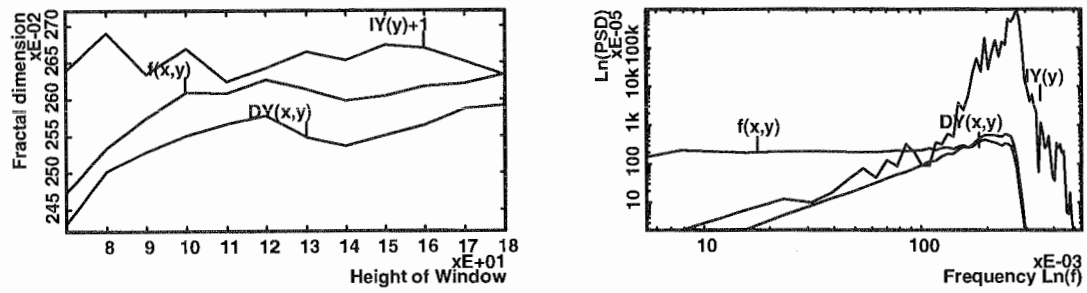

(j) from Figure 4.6.j

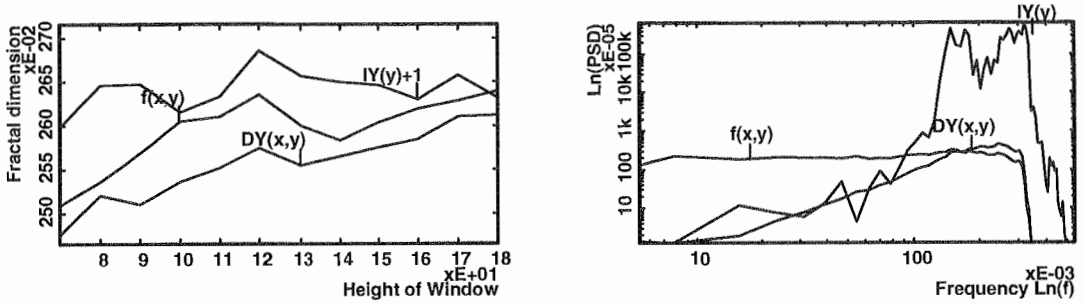

(k) from Figure 4.6.k

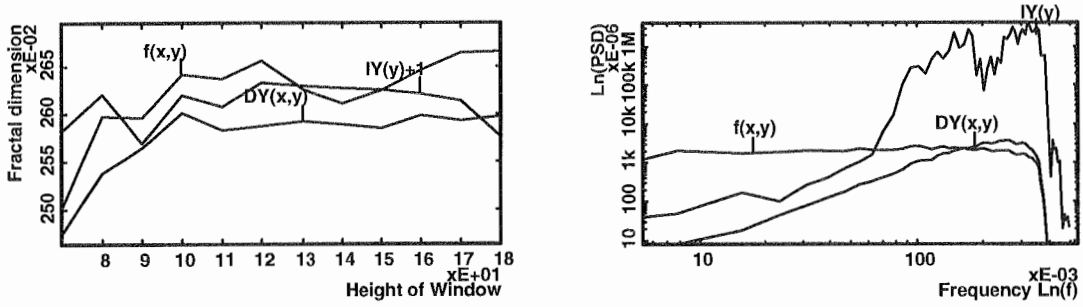

(l) from Figure 4.6.l

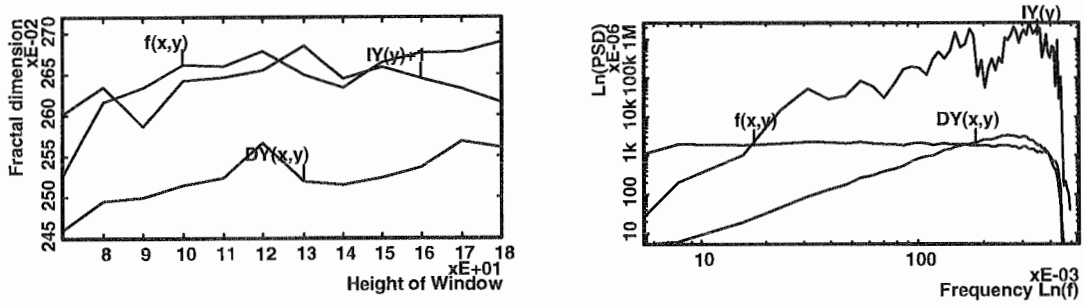

(m) from Figure 4.6.m

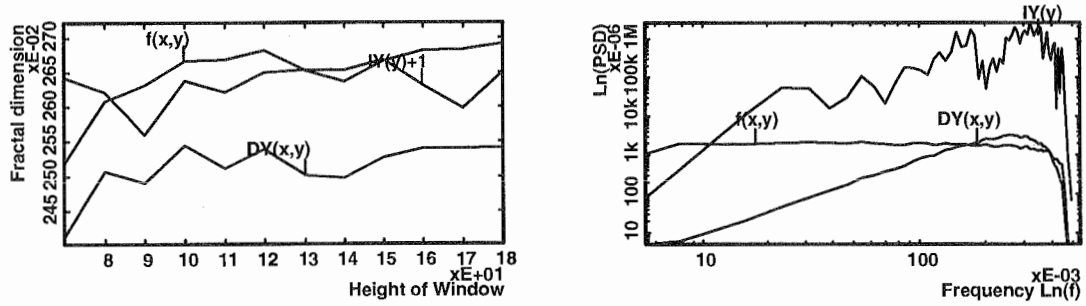

(n) from Figure 4.6.n

Figure 4.7 PSD and fractal dimension comparison of example iamges with height of windows (Centre = 130, Window width =180 pixel).

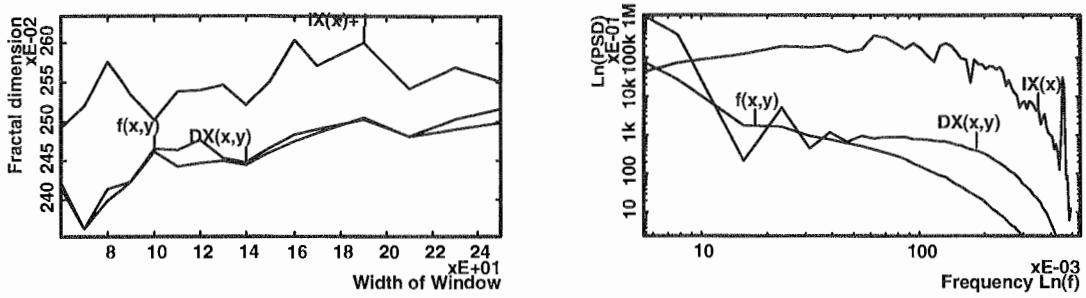

(a) from Figure 4.6.a

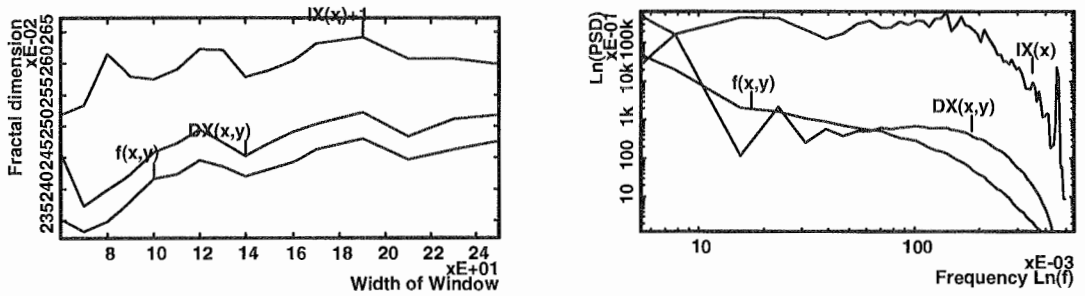

(b) from Figure 4.6.b

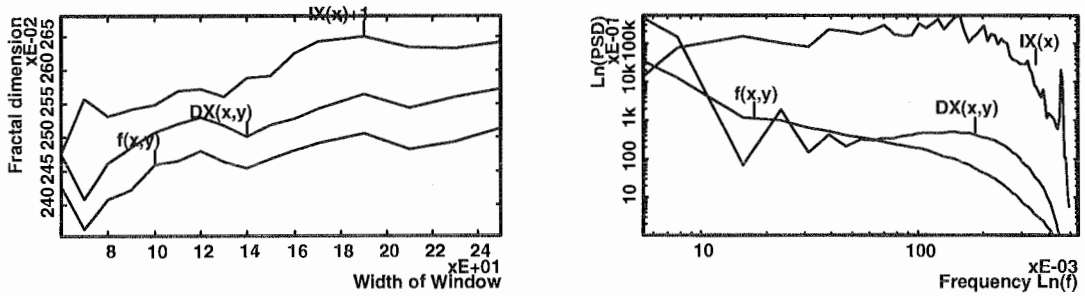

(c) from Figure 4.6.c

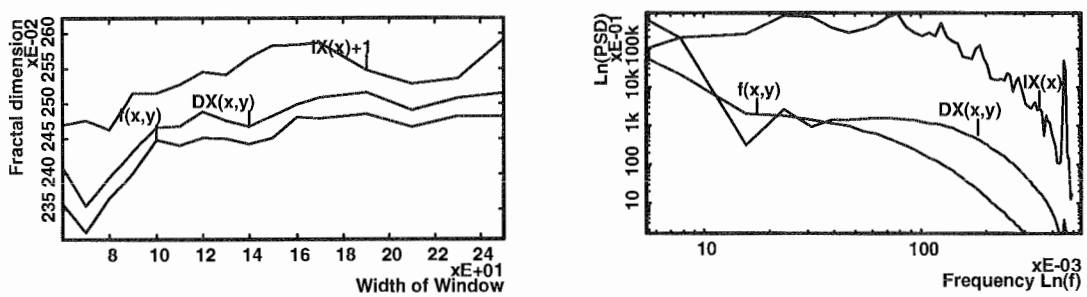

(d) from Figure 4.6.d

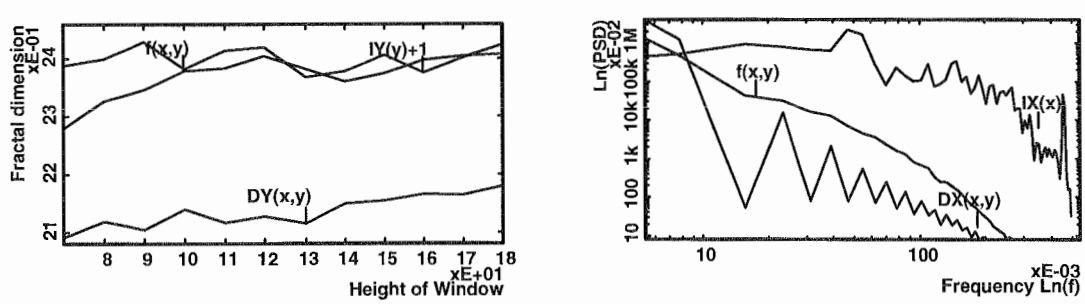

(e) from Figure 4.6.e

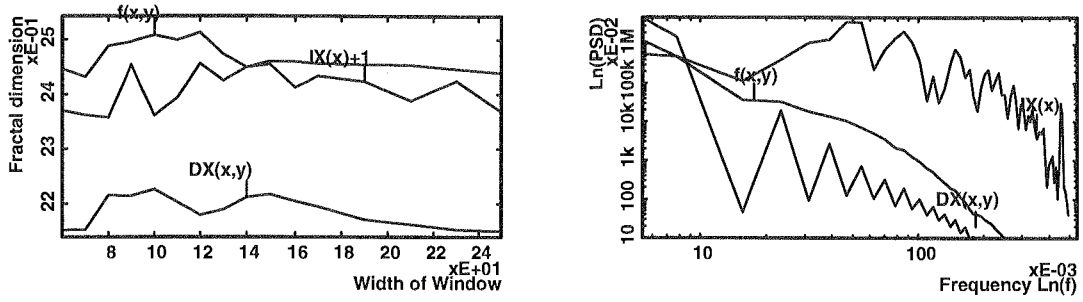

(f) from Figure 4.6.f

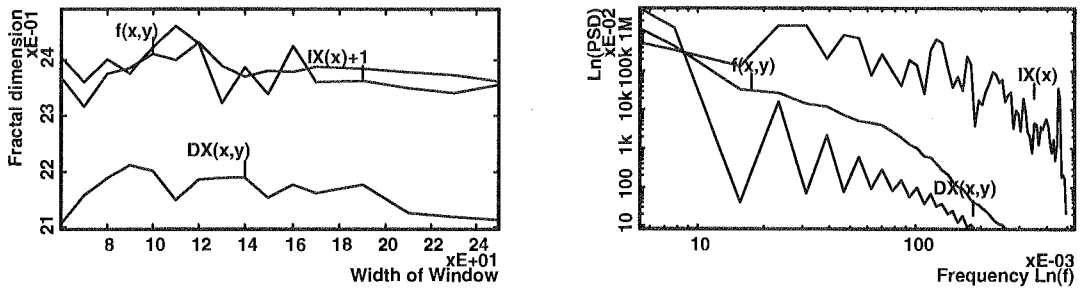

(g) from Figure 4.6.g

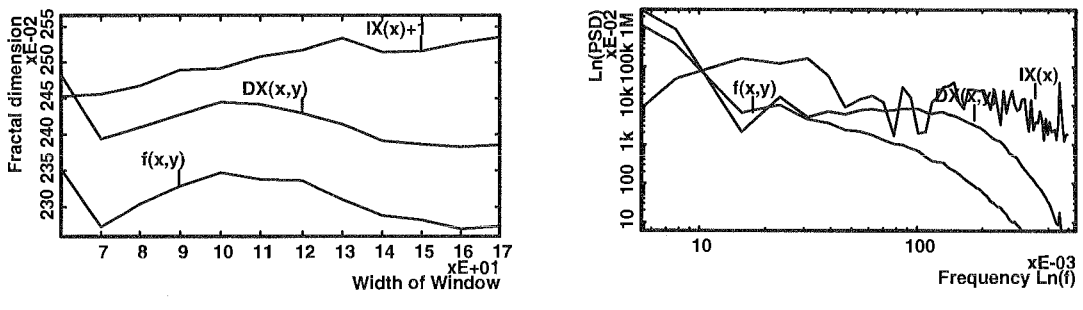

(h) from Figure 4.6.h

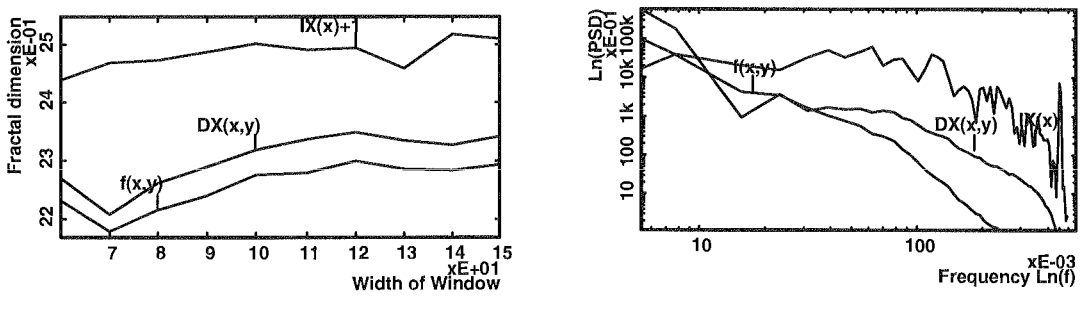

(i) from Figure 4.6.i

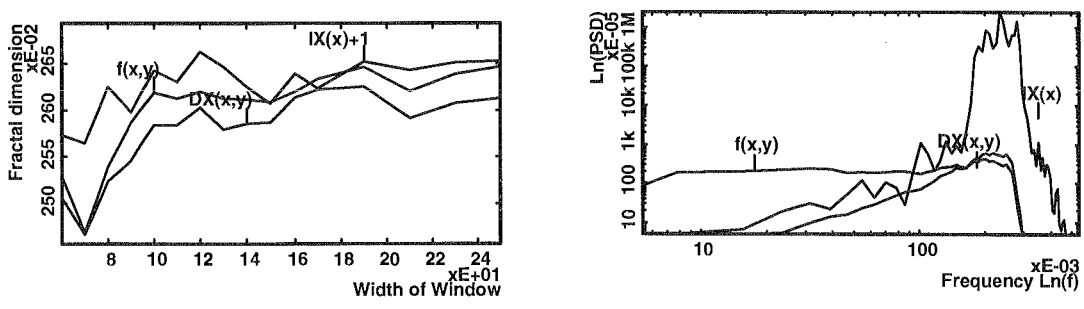

(j) from Figure 4.6.j

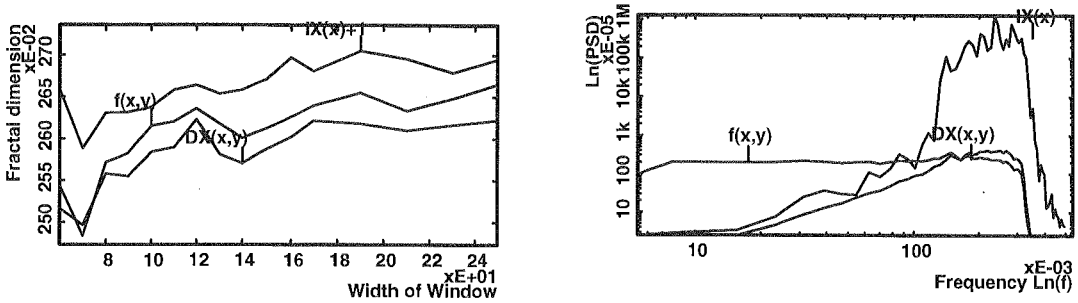

(k) from Figure 4.6.k

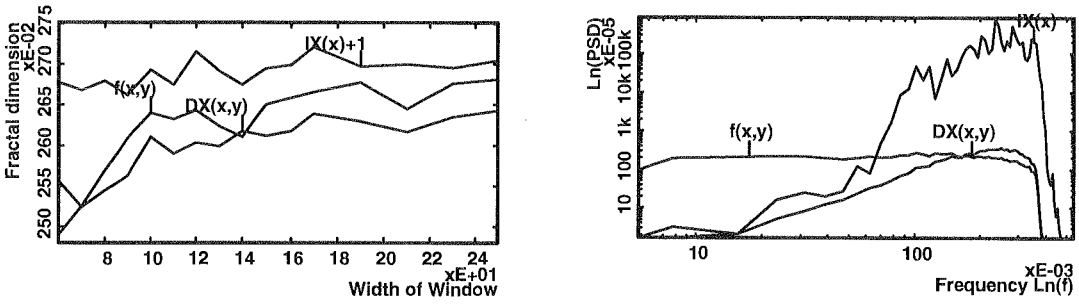

(l) from Figure 4.6.l

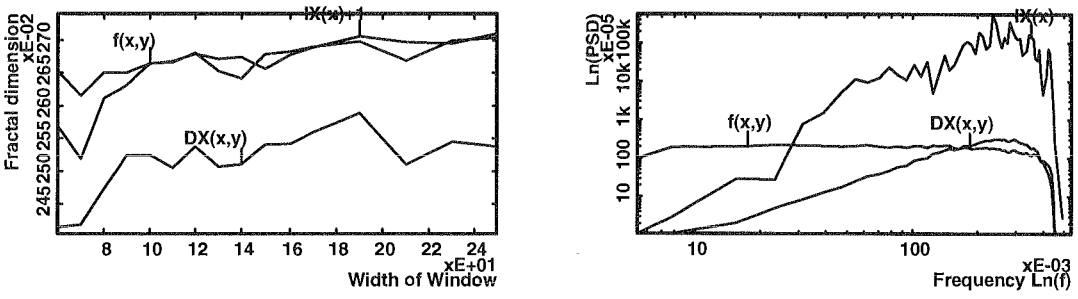

(m) from Figure 4.6.m

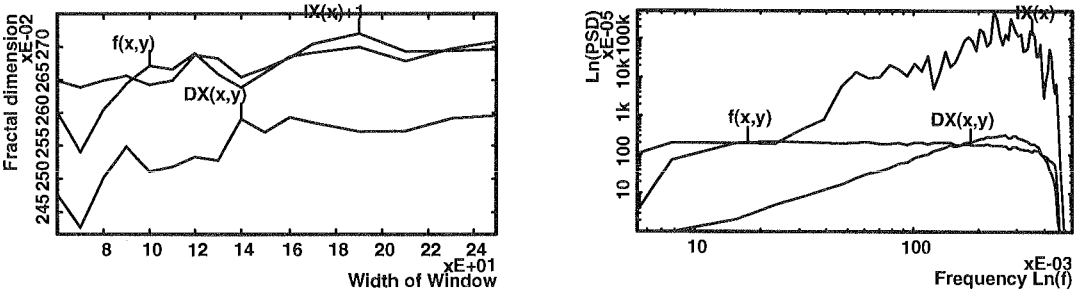

(n) from Figure 4.6.n

Figure 4.8 PSD and fractal dimension comparison of example images variation with windows width. (Centre = 130, Window height = 160 pixel).

Table 4.4.1 The fractal dimension for Figure 4.7 (variation with window height averaged over the range of window height indicated).

Figure 4.6	*f(x,y)*	*DY(x,y)*	*IY(y)+1*	*DY(x,y)-f(x,y)*	*IY(y)+1-f(x,y)*	Hight range for average
a	2.461	2.464	2.520	0.003	0.059	90~160
b	2.426	2.455	2.561	0.029	0.135	90~160
c	2.455	2.457	2.604	0.002	0.150	90~160
d	2.448	2.432	2.561	-0.016	0.113	90~160
e	2.378	2.134	2.396	-0.245	0.018	90~160
f	2.454	2.157	2.431	-0.297	-0.023	90~160
g	2.450	2.152	2.403	-0.298	-0.047	90~160
h	2.318	2.359	2.625	0.040	0.306	90~160
i	2.287	2.296	2.381	0.009	0.094	90~160
j	2.606	2.553	2.654	-0.053	0.047	90~160
k	2.603	2.557	2.645	-0.046	0.042	90~160
l	2.630	2.588	2.617	-0.042	-0.013	90~160
m	2.657	2.524	2.645	-0.133	-0.012	90~160
n	2.661	2.519	2.634	-0.142	-0.026	90~160

Table 4.4.2 The fractal dimension of Figure 4.8 (variation with window width averaged over the range of window width indicated).

Figure 4.6	*f(x,y)*	*DX(x,y)*	*IX(x)+1*	*DX(x,y)-f(x,y)*	*IX(x)+1-f(x,y)*	Width range for average
a	2.468	2.475	2.559	0.007	0.091	110~210
b	2.445	2.486	2.612	0.041	0.166	110~210
c	2.478	2.530	2.608	0.053	0.130	110~210
d	2.463	2.491	2.560	0.028	0.097	110~210
e	2.413	2.183	2.384	-0.229	-0.029	110~210
f	2.465	2.191	2.431	-0.274	-0.035	110~210
g	2.469	2.228	2.372	-0.240	-0.097	110~210
h	2.293	2.398	2.524	0.105	0.231	110~170
i	2.290	2.338	2.495	0.048	0.205	110~210
j	2.622	2.601	2.637	-0.021	0.016	110~210
k	2.627	2.602	2.678	-0.026	0.051	110~210
l	2.647	2.617	2.699	-0.030	0.052	110~210
m	2.674	2.537	2.681	-0.137	0.007	110~210
n	2.675	2.568	2.686	-0.107	0.011	110~210

Table 4.4.3 The estimation of fractal dimension from PSD distribution of Figure 4.7 (variation with the range of window height and width are indicated in table 4.4.1~2).

Figure 4.7	$f(x,y)_{PSD}$	$f(x,y)_{cal.}$	Figure 4.8	$f(x,y)_{PSD}$	$f(x,y)_{cal.}$
a	2.52	2.46	a	2.61	2.47
b	2.63	2.43	b	2.69	2.45
c	2.73	2.46	c	2.77	2.48
d	2.51	2.45	d	2.65	2.46
e	2.44	2.38	e	2.47	2.41
f	2.45	2.45	f	2.48	2.47
g	2.47	2.45	g	2.44	2.47
h	2.54	2.32	h	2.63	2.29
i	2.40	2.29	i	2.41	2.29

subscribe note in the table 4.4.3:

PSD fractal dimension estimated from the slope of PSD distribution according to Equation 4.3.1.

cal. fractal dimension calculated by box counting method.

Figures 4.7~8 show the fractal dimension and PSD for *f(x,y)*, *DX(x,y)*, *DY(x,y)*, *IX(x)* and *IY(y)*. For ease of comparison, the fractal values of *IX(x)* and *IY(y)* have been increased by one in these Figures. As indicated above, the fractal dimension is more reliable with a window width of 120~220 and window height 90~160. Thus the comparison of the fractal dimension will be conducted in this range in order to consider the application of Equation 4.3.1. Table 4.4.1 and Table 4.4.2 tabulate the average fractal dimension of Figure 4.7 and Figure 4.8 separately, the values in these tables being obtained by averaging the fractal dimension over the window size range. The spectra for the derivative fields and after application of the schlieren operations of differentiation and integration (Figures 4.7 and 4.8) did not in general show a regular form with a systematic decrease of PSD over a substantial range of frequency with a negative exponent of the PSD. Therefore it was not considered appropriate to attempt to measure a negative slope or to apply Equation 4.3.1 in these cases. However, the original images *f(x, y)* in Figures 4.7 and 4.8 (a) - (i) did yield substantial sections for which the spectral density reduced regularly with frequency, and for these cases, Table 4.4.3 show the results of fractal dimension calculated by measurement of the negative slope of the power spectra and using Equation 4.3.1 as well as the directly measured fractal dimensions. We see that whilst there is moderately good agreement in most cases, the comparison is certainly not exact. However, it must be borne in mind that

these images do not conform to fractional Brownian form as all the spectra show same irregularity to a greater or lesser degree. It is concluded that the results conform generally to the expectation of Equation 4.3.1, but that the images themselves do not have sufficiently regular behaviour for this equation to apply exactly.

The various leaves images (Figure 4.6.a~d) exhibit very similar fractal character. All the leaves images and their derivative images have almost the same fractal dimensions which are in the narrow range from 2.42 to 2.53. The simulated schlieren image cuts of leaves images *IX(x)* and *IY(y)* have an average fractal dimension of 1.60 + 1 = 2.60. The PSD of *f(x,y)*, *DX(x,y)* and *DY(x,y)* are very similar in trend while the PSD of *IX(x)* and *IY(y)* are quite different from the original images. We see that for these leaves images the original field and derivative field have rather similar spectral and fractal dimension, whilst the differentiating and integrating operations corresponding to a schlieren processing of the original field give rise to a higher fractal dimension and a correspondingly broader spectrum. It appears that in this case the differentiating character of the schlieren operation dominates over its integrating character, and we would expect an increase of the relative contribution of higher frequency spectral components. The correspondence between fractal character and PSD is further supported by the diffusion flame and hot jet images (Figure 4.6.e~h). Figure 4.6.e shows the natural diffusion flame whilst Figure 4.6.f has the same flow condition but with 40 Hz excitation frequency and Figure 4.6.g has 420 Hz excitation frequency. The excitation structures in Figure 4.6.f~g have been analysed in Chapter 3 with the Abel transform method. In the fractal analysis, the effect of excitation is not as obvious as that on induced structures determined by signal averaging in the diffusion flame. First, the three images have a similar fractal relationship between *f(x,y)*, *DX(x,y)*, *DY(x,y)*, *IX(x)* and *IY(y)* except that the excitation generally increases the fractal dimension slightly. In contrast to the leaves images, in which the *f(x,y)* with *DX(x,y)* and *DY(x,y)* have nearly the same fractal dimension, the fractal dimension of *DX(x,y)* and *DY(x,y)* in Figure 4.6.e~g are around 2.15 which is far less than that of *f(x,y)*. The PSD of *DX(x,y)* and *DY(x,y)* represent a departure from *f(x,y)* and show a fluctuating shape due to the large structures in the flow rather than due only to the excitation. The PSD of *f(x,y)*, *IX(x)* and *IY(y)* show a similar trend in all three cases. Due to the roughness of PSD curves, it is still not practicable to quantitatively determine the slope of the PSD and use it to estimate the fractal dimension of images by Equation 4.3.6. We see that for these flame images the fractal dimension of the original field *f(x, y)* and of the result of the schlieren differentiation and integration operations *IX(x)* or *IY(y)* are quite similar in all cases. This result is of particular

interest as it shows us that the fractal dimension determined by a schlieren system would be quite similar to that of the original field for these distributions characteristic of a combustion flame. That is, in these cases the operations of integration and differentiation produce counteracting effects on the measured fractal dimension.

The images of Figure 4.6.h~i are more homogenous than those in Figure 4.6.e~g. Figure 4.6.h is a hot jet image whilst 4.6.i is a portion of an unexcited flame. The images are more homogenous in the y (height of window) direction than in the x (width of window) direction where the total window extends beyond the flow range. The character of the hot jet in the y direction is similar to the leaves images as also is that of Figure 4.6.i. This is taken at a downstream position in a diffusion flame and exhibits a similar fractal character to the leaves images with the fractal dimension of the differentiated and original fields being very similar whilst that generated by the schlieren operation applied to the image flame is significantly higher. The PSD of Figure 4.6.i reflects a corresponding effect with a broader band distribution resulting from the schlieren operation. The exception to these general features is the x derivative field of the hot jet, for which the fractal dimension is more nearly similar to that resulting from the schlieren operation. This is more like the effects observed for the flames in Figure 4.4.e~g, and reflects the presence of rather weaker axial structures which are evident in the hot jet image (Figure 4.6.h). All these results suggest that the homogenous images (Figure 4.6.a~d, i) show more similar fractal character, with comparable fractal dimensions for $f(x,y)$, $DX(x,y)$ and $DY(x,y)$ and bigger fractal dimensions for $IX(x)$ and $IY(y)$. The PSD of these more homogenous images correspond in general form to their fractal characters. The fractal and PSD character of the less homogenous images (Figure 4.6.e~h) depend more on the image structures, but in general yield fractal dimension of the original field which are quite close to those obtained after the schlieren operations of differentiation and integration.

The band limited images (Figure 4.6.j~n) show very different results. The fractal dimensions do not vary significantly for the band limited images due to the selected bandwidth function. The differences of the average fractal dimension between $f(x,y)$, $DX(x,y)$, $DY(x,y)$, $IX(x)$ and $IY(y)$ for these random images are less than 0.15 (as shown in Tables 4.4.1~2). The spectra of the band limited images show that for the original field function $f(x,y)$ the high frequency cut off extend to higher frequency as the pass band is broadened as we would expect. However, the spectra remain flat to low frequency in all cases because the passband filter has been applied by the image generation software to the two dimensional distribution. This has the consequences of

relatively spectral energy in the one dimensional spectra of these fields which are shown owing to the random orientations of the band limited fluctuation which continue to give rise to low wave number fluctuation along the line across which the one dimensional spectrum is evaluated. It should be noted that this applies to all the spectra shown in this section for two dimensional fields. The spectra of the derivative fields simply show the increase of the spectral density with frequency as we would expect. However after application of the schlieren operation of differentiation and integration to the whole field *f(x,y)*, the spectra of *IX(x)* and *IY(y)* show clearly the effects of the pass band filtering which has been applied in the original image generation. This is essentially because of the integration operation which reveals the low frequency cut off in the resultant spectra of *IX(x)* and *IY(y)*.

4.5 Fractal dimension analysis of turbulent images

The turbulent images used for detailed fractal analysis are shown in Figure 4.9 with overlaid location grids. Figure 4.9.a is a natural unexcited diffusion flame. Figure 4.9.b has the same flow condition but with acoustic forcing at 40 Hz excitation frequency, while Figure 4.9.c has a 420 Hz excitation frequency. Figure 4.9.e is a natural hot jet image. The fractal dimension will be calculated for various selected work windows within the overall image. Both the height and width of the window are symmetrical to the centre of window. As already described before, for a certain range of window size, the fractal dimension is quite stable (for the turbulent flame, this range =120~170). Beyond that range the fractal character would be totally changed due to the inclusion of the flow region boundary structure. The fractal dimension variation with window size and window location are shown in Figures 4.10~12. The fractal dimension decreases gradually along the downstream flow direction. The fractal dimension is also sensitive to the change of window width due to the transverse and rounded structure of the turbulent flow region in the flame. The averaged fractal dimension for the Figures 4.10~12 are tabulated in Tables 4.5.1~3.

Figure 4.10 shows the variation in measured fractal dimension with the height of window. It is clear that the measured fractal dimension for both flame and jet generally increases only slowly with window height, but with clear cycles of moderate strength superimposed on the trend which exhibits the effect of large scale periodic

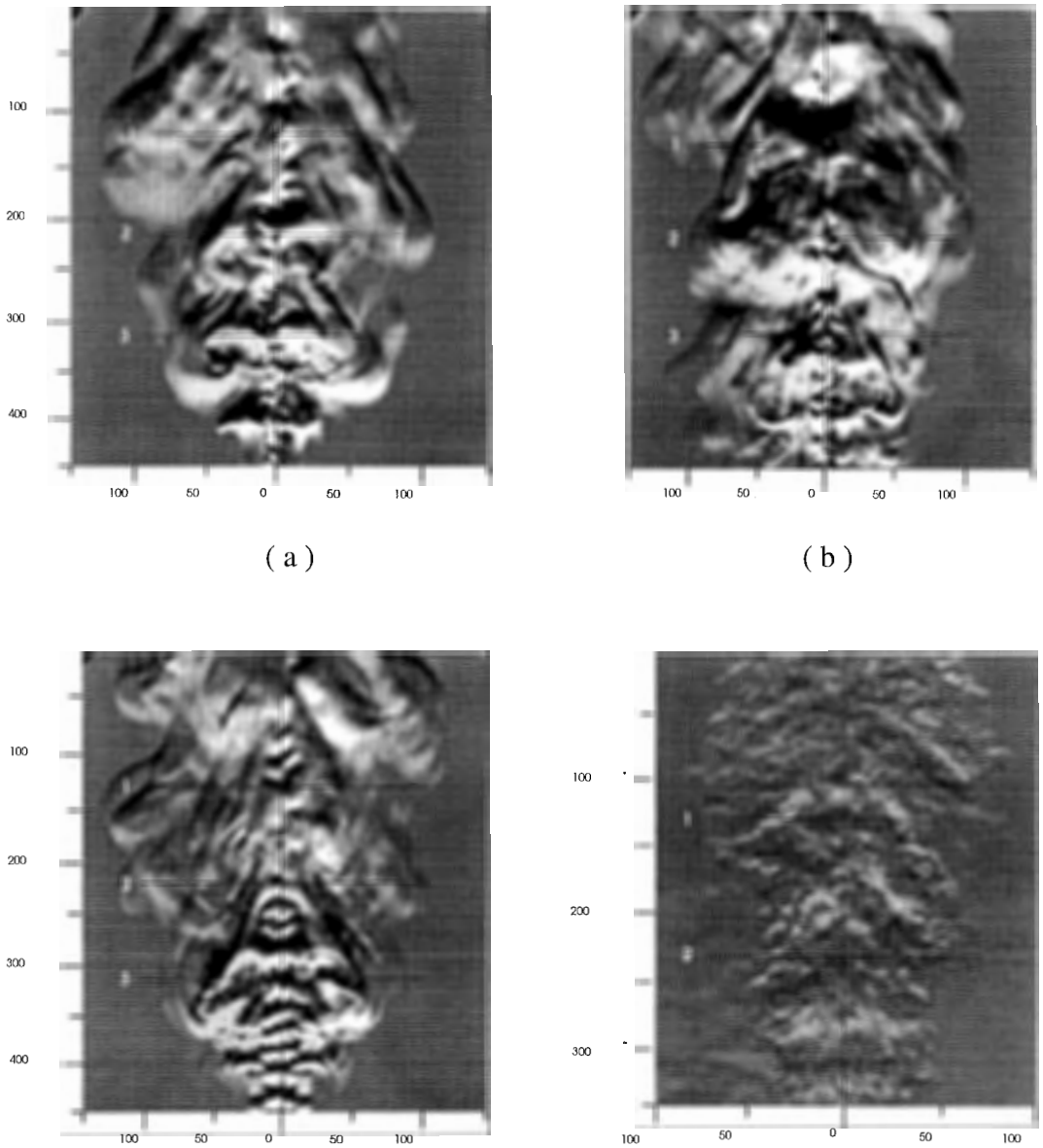

Figure 4.9 The turbulent images used for fractal analysis. (a) No excitation natural diffusion flame, (b) 40 Hz excitation, (c) 420 Hz excitation (Velocity of gas = 2.5 m/s, Velocity of air = 2 m/s). (d) Hot jet (Re = 19000). The scale is pixel (1 pixel equal 0.37 mm in horizontal direction and 0.27 mm in vertical direction).

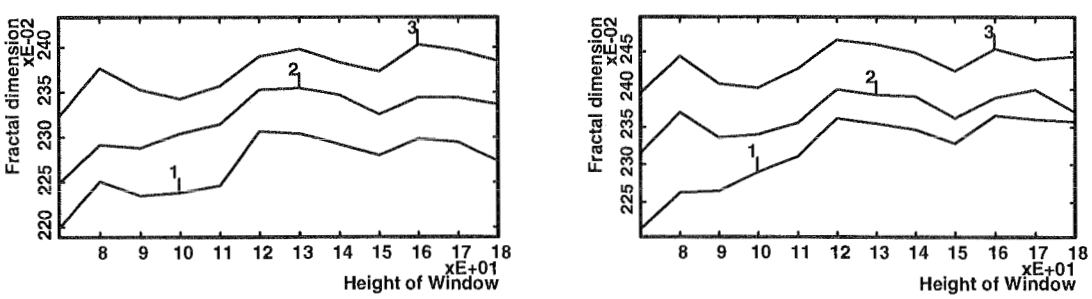

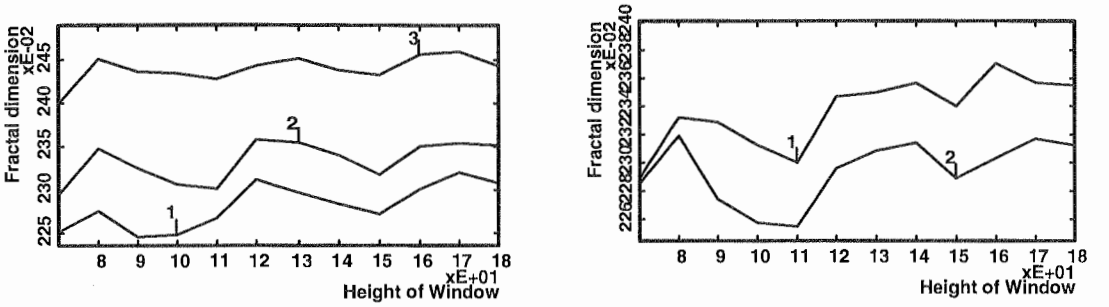

(c) (d)

Figure 4.10 Average fractal dimension of diffusion flame variation with height and position of windows. (a) No excitation diffusion flame, (b) 40 Hz excitation, (c) 420 Hz excitation, (d) Hot jet. Curve 1: Centre = 130, Curve 2: Centre = 220, Curve 3: Centre = 310. Window width =120 pixel.

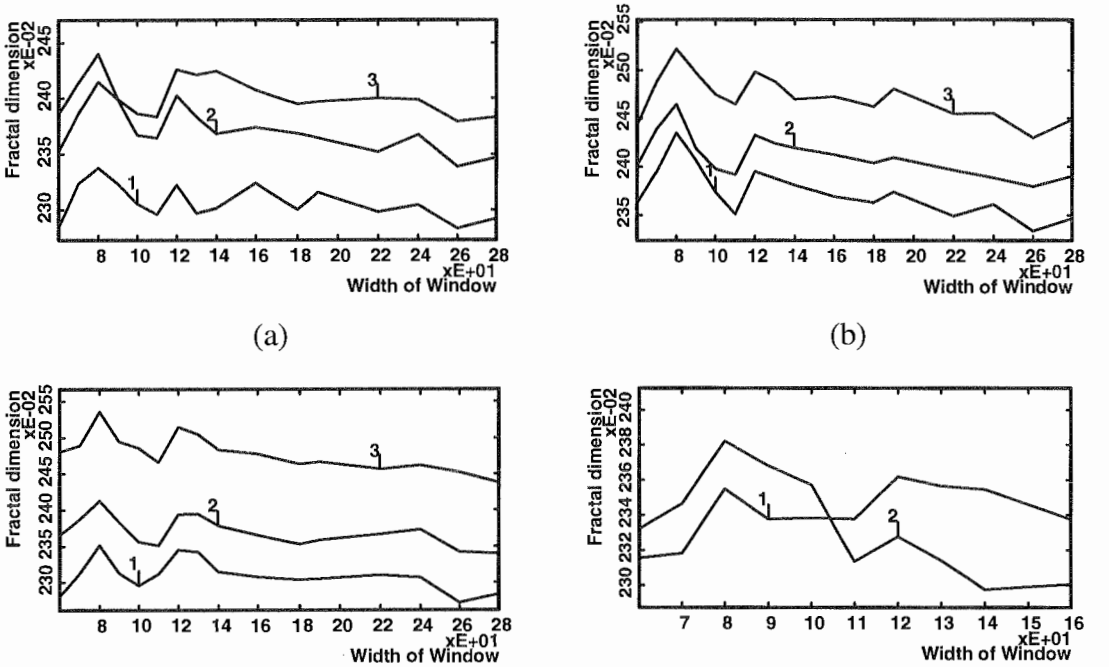

(a) (b)

(c) (d)

Figure 4.11 Average fractal dimension of diffusion flame variation with width and position of window. (a) No excitation diffusion flame, (b) 40 Hz excitation, (c) 420 Hz excitation, (d) Hot jet. Curve 1: Centre = 130, Curve 2: Centre = 220, Curve 3: Centre = 310. Window height = 120 pixel.

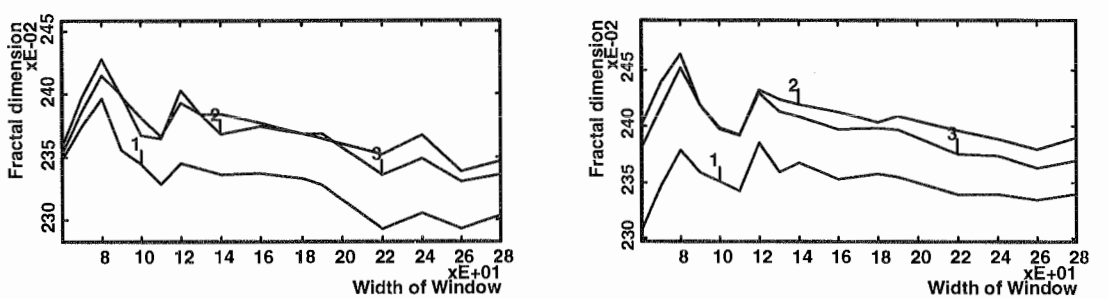

(a) (b)

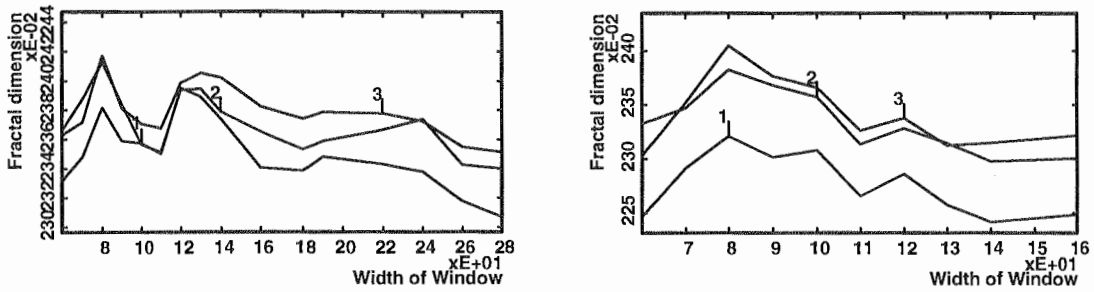

(c) (d)

Figure 4.12 Average fractal dimension of diffusion flame variation with width of window. (a) No excitation diffusion flame, (b) 40 Hz excitation, (c) 420 Hz excitation, (d) Hot jet. Curve 1: height = 100, Curve 2: height = 140, Curve 3: height = 130. Window centre = 220 pixel.

Table 4.5.1 The average fractal dimension variation of Figure 4.10.

Figure 4.10	*Curve 1*	*Curve 2*	*Curve 3*	*Cur. 2-Cur. 1*	*Cur. 3-Cur. 1*
a	2.301	2.353	2.380	0.053	0.079
b	2.355	2.386	2.468	0.031	0.112
c	2.300	2.360	2.463	0.060	0.163
d	2.338	2.287		-0.051	

Table 4.5.2 The average fractal dimension variation of Figure 4.11.

Figure 4.11	*Curve 1*	*Curve 2*	*Curve 3*	*Cur. 2-Cur. 1*	*Cur. 3-Cur. 1*
a	2.293	2.370	2.412	0.077	0.119
b	2.381	2.399	2.471	0.018	0.090
c	2.328	2.386	2.478	0.059	0.151
d	2.353	2.321		-0.032	

Table 4.5.3 The average fractal dimension variation of Figure 4.12.

Figure 4.12	*Curve 1*	*Curve 2*	*Curve 3*	*Cur. 2-Cur. 1*	*Cur. 3-Cur. 1*
a	2.327	2.373	2.370	0.045	0.043
b	2.357	2.411	2.399	0.054	0.042
c	2.358	2.373	2.386	0.015	0.028
d	2.258	2.310	2.321	0.052	0.063

and turbulent structure in the flow. The fractal dimension also tends to decrease as the observation position moves downstream for the flames, as is shown also in Figure 4.11. For the heated jet the opposite trend is apparent, the fractal dimension increases as the flow moves downstream except when the window was narrowed to only the central 100 pixels of the image. The fractal dimension varies as we might expect with the width of window (Figures 4.11~12): when the window width is larger than 120 pixels, the fractal dimension becomes steady and only decreases slightly as the width extends until the width reaches 240 pixel, beyond which the window extends outside the edge of the flame and the fractal dimension starts decreasing. As shown in Figures 4.11~12, the fractal dimension is fairly steady with a window width of 120~220 or window height of 90~160. Smaller than this area, the fractal dimension of turbulent image becomes too volatile to represent whole image, and above this area, the window is so large as to extend beyond boundary. The average fractal dimension is 2.35 for unexcited flame, 2.40 for the excited flames and 2.30 for the hot jet flow. At the top of the images (downstream and centre position 1) where the image is more homogenous than close to the nozzle exit, the average fractal dimension of the turbulent images is 2.30 (including the hot jet).

From above descriptions, we see that the fractal dimension of the turbulent flow schlieren images clearly depends on the excitation and character of the turbulent flow. However, the excitation of turbulent flow only increases the fractal dimension by about 0.05. The range of fractal dimension of the schlieren images in the present investigation is 2.30~2.47, suggesting that an average fractal dimension of approximately 2.35~2.40 would apply to the general description of a diffusion flame or mixing jet image. This result is close to those of Lovejoy (1982), Herntschel and Procaccia (1984) and also Sreenivasan and Meneveau (1986).

4.6 Concluding discussion

Using images of leaves, jet and flame flows and band limited random images we have investigated the relationship between the fractal dimension of an original field and its schlieren image resulting from differentiation in a direction in the image plane and integration along the perpendicular optical path. These images are simply used here to provide an indication of the general relationships that exist. It is found that the random leaves images with spectral level that reduce with frequency give an appreciably

larger fractal dimension after differentiation and integration than for the original field and its derivative field, which tend to have similar fractal dimensions. The band limited random images have fractal dimensions for the field, derivative field and after differentiation and integration, which are more generally close to one another. The images deriving from the flames with some apparent large structures yielded fractal dimensions of the original field and after application of the schlieren operations of differentiation and integration which are quite similar, and which exceeded the fractal dimension of the derivative field appreciably. However the more random images of the heated jet and in the downstream region of the developed turbulent flame gave fractal dimensions which were more similar to the random leaves images. The fractal dimension after application of the schlieren operations of differentiation and integration significantly exceeding these of the original field and its derivative field which were quite similar.

We conclude that the fractal dimension of a schlieren image is close to that of the original density field for cases such as the initial flame where the latter has a sharply reducing spectral density distribution and the appearance of dominant large structure. For cases where more random schlieren images arise, such as the developed flame region or hot jet, the fractal dimension of the schlieren image is likely to exceed the fractal dimension of the original field and its derivative field appreciably.

We are aware of Sreenivasan's suggestion (1986, 1991) that the fractal dimensions of an atmospheric cloud surface and those of it's projection are not same. We believe that the different conclusions between ours and Sreenivasan's are caused by the different approach which have been used to collect the images. The schlieren image of flame represents the combination of projection and differentiation of the fluid density gradient map, whereas Sreenivasan was discussing only the projection. The projection image can be considered as superposition of a large number of sections, each section being separated from other by distances of the order η. However, the effects of differentiation and projection are much more complex and give approximately compensating effects on the calculated fractal dimension of schlieren image and the relation to the dimension of the actual refractive index field.

The fractal dimension of the schlieren images of the initial zones of the diffusion flame where characteristic structure is apparent generally lies in the range of 2.30~2.47, with a tendency to decrease in the flow direction. For the heated jet flow the schlieren image had a fractal dimension also in the range 2.30~2.47 but with a

tendency to rise in the flow direction. Owing to the more random appearance of the hot jet image it appears that the fractal dimension of the flow density field would be somewhat smaller than that of the schlieren image, whilst for the flame cases we expect the fractal dimension observed in the schlieren image to be quite similar to that of the refractive index field in the flow.

The investigation of fractal distribution of diffusion flame images has also shown the box counting is a satisfactory method for analysing the fractal character of turbulent images with a variance of approximately 0.04 in the fractal dimension.

Finally, particular attention is drawn to Figures 4.5(c) and (d). It appears that transverse differentiation of the schlieren image and subsequent contour extraction are highly effective in indicating systematic mixing and reaction flow structures in the turbulent flame which are oriented at approximately 25° to the flow direction (see Figure 4.5.d). It is clear that these images show considerable potential for further valuable investigation of turbulent combustion structures.

Chapter 5 CONCLUSIONS

5.1 The induced structures of diffusion flames

It has been found that signal averaging or recovery from noise by phase reference to an acoustic excitation is an effective means of determining structures induced in a diffusion flame. Generally consistent results for the structure and strength of induced disturbances have been obtained by signal recovery from both axial and radial schlieren deflections, although there are some limitations in the present results due to the relatively small coannular nozzle system and flame investigated.

Two quite distinct physical modes of response have been detected at the two Strouhal numbers which were known from previous investigation to be the most responsive for the particular nozzle system and flame configuration investigated. At the higher excitation frequency and Strouhal number of 1.01, the excitation at 9.5% of inner nozzle exit velocity produced ±5.1% fluctuation of refractive index normalised on the upper bound for refractive index fluctuations, that is the difference between the refractivity of the propane fuel and the fully reacted stoichiometric mixture. The structures formed were a series of alternating disturbances centred along the central nozzle axis with a repeating wavelength of twice the inner nozzle diameter. These small inner flow disturbances showed a very slow rate of reduction of strength with distance from the nozzle and thus would persist for a substantial distance from the nozzle. At the lower excitation frequency and Strouhal number of 0.4 based on the outer nozzle parameters an excitation of 6.5% of the exit velocity induced a ±12% fluctuation of refractive index. In this case the structure induced in the flow was a series of alternating ring structures of approximately the same diameter as the outer nozzle and with a repetition of wavelength 5.2 times the outer nozzle diameter. Contained within these ringlike structures were a series of alternating disturbances along and centred on the flow axis, of opposite sense to the surrounding ring structure. These larger scale disturbances weakened rapidly with distance from the

nozzle, indicating a rapid breakup of the regular ringlike structures between the two measuring points. These results provide conclusive evidence that (1) signal averaging or recovery from noise by phase reference to an acoustic excitation is an effective means of determining structures and (2) the strength of induced disturbances have been obtained by signal recovery from both axial and transverse schlieren beam deflections, although there are some limitation in the present results due to the relatively small coannular nozzle system and flame investigated. Any approach at high excitation frequency should take extra caution in regard to the measurement accuracy, quality of acoustic exciter signal generator and elimination of acoustic asymmetry from the signal near the nozzle.

5.2 The fractal structures of diffusion flame images

The fractal texture of the propane/air diffusion flame was obtained by analysing the fractal distribution of flame schlieren images based on the box counting method. In principle, the fractal parameters can be derived from fractal plots of either L versus ε or N versus ε plot. Therefore, the L versus ε plot provides a sensitive means of extracting the fractal parameters from experimental data. The determination of the fractal dimension relies on a clear indication of the fractal range i.e. the linear region of the fractal plot, and its limits, the inner and outer cut-offs.

The results of the investigation suggest that the diffusion flames exhibits fractal behaviour and that the values of fractal dimension are in the range of 2.35~2.40 and depend on the excitation and character of the turbulent flow. The investigation of the fractal distribution of diffusion flame images has also shown that the box counting is an effective method to determine the fractal texture of diffusion flame schlieren images with a variance of approximately 0.04 in the fractal dimension.

The Power Spectrum Density (PSD) of propane/air diffusion flames have also been investigated. These observations of PSD appeared to be generally consistent with the

fractal dimensions obtained. A numerical simulation of the fractal relationship between the diffusion flames and their schlieren images suggests that fractal character (and the PSD) of the schlieren images are similar to those of the flame itself. There is no simple universal relationship between the fractal dimension of the schlieren image and that of the actual spatial field which gave rise to the image. However, it seems from these results that the fractal dimensions of diffusion flames and their schlieren images are similar. More homogeneous schlieren images fields with less evidence of large scale structures and with correspondingly broader PSD distributions had fractal dimensions which were appreciably greater than those of the original flow field.

It has been found that transverse differentiation of the schlieren image and subsequent contour extraction, is highly effective in indicating systematic mixing and reaction flow structures in the turbulent flame at about ±25° to the flow axis. It seems that this method has considerable potential for further investigation of turbulent combustion structures.

BIBLIOGRAPHY

1. Adrian, R. J. 1991. Particle-imaging techniques for experimental fluids mechanics. *Annual Review of Fluid Mechanics*. 23, 261-304,
2. Anderssen, R. S. 1973. Computing with noisy data with an application to Abel's equation. In *Error, Approximation And Accuracy* (ed. by F. R. de Hoog and C. L. Jarvis). St. lucia, University of Queensland Press.
3. Ballal, D. R. 1986. Studies of Turbulent Flow-Flame Interaction. *AIAA Journal* 24, 1148-1154.
4. Barnsley, M. F. 1988. *Fractals Everywhere*. Academic Press, INC.
5. Batty, M. 1985. Fractals-geometry between dimensions. *New Scientists* 145, 31-35.
6. Bradshaw, P. 1971. *An Introduction to Turbulence and Its Measurement*. Pergamon Press, Oxford.
7. Broadwell, J. E. and Dimotakis, P. E. 1986. Implication of recent experimental results for modelling reaction in turbulent flows. *AIAA Journal* 24, 875-889.
8. Brokman, S. and Levin, D. 1993. A flow visualization study of the flow in a 2D array of fins. *Experiments in Fluids* 14, 241-245.
9. Brown, G. L and Roshko, A. 1974. The effect of density difference on the developing mixing layers. *Journal of Fluid Mechanics*. 64, 775-816.
10. Brown, G. L. and Roshko, A. 1974. On density effects and large structures in turbulent mixing layers. *Journal of Fluid Mechanics* 64, 775-816.
11. Cabelli, A., Pearson, I. G., Shepherd, I. C., and Hamilton, N. B. 1988. Fluid dynamic structures in jet diffusion flames: Acoustic effects. *First World Conference on Heat Transfer, Fluid Mechanic Thermodynamics*, Dubrovnik.
12. Chao, Y. C. and Jeng, M. S. and Han, J. M. 1991. Visualization and image processing of an acoustically excited jet flow. *Experiments in Fluids* 12, 29-40.
13. Chen, L. D. and Roquemore, W. M. 1986. Visualisation of jet flames. *Combustion and Flame* 66, 81-86.
14. Corrsin, S. 1963. Turbulence: Experimental Methods. *Handbuch der Physik*. 8 (2). Springer, Berlin.
15. Crighton, D. G. 1981. Jet noise and the effects of jet forcing. *Lecture Notes in Physics* 136. Springer-Verlag, Berlin.
16. Crow, S. and Champagne, F. M. 1971. Orderly structure in jet turbulence. *Journal of Fluid Mechanics* 48, 547-591.
17. Davis, M. R. 1971. Measurements in a subsonic turbulent jet using a quantitative schlieren technique. *Journal of Fluid Mechanics* 46, 631-656.

18. Davis, M. R. 1972. Quantitative Schlieren measurements in a supersonic turbulent jet. *Journal of Fluid Mechanics* 51, 435-447.
19. Davis, M. R. 1975. Intensity, scale and convection of turbulent density fluctuations. *Journal of Fluid Mechanics* 70, 463-479.
20. Davis, M. R. 1987. Turbulent refractive index fluctuations in a hydrogen diffusion flame. *Combust. Sci. and Tech* 64, 51-65.
21. Davis, M. R. and Jumppanen, P. C 1993. Optical detection of the response of a diffusion flame to excitation. *Combustion and Flame* 93, 349-374.
22. Davis, M. R. and Rerkshananda, P. 1993. Schlieren measurement of turbulent structure in a diffusion flam. *Experimental and Thermal Fluid Science* 6, 402-416.
23. Eichhoff, H. and Winandy, A. 1985. Visualisation of vortex formation in jet diffusion flames. *Combustion and Flame* 60, 99-101.
24. Fisher, M. J. and Krause, F. R. 1967. The cross beam correlation technique. *Journal of Fluid Mechanics* 28, 705-717.
25. Freeman, M. P. and Katz, S. 1960. Determination of the radial distribution of brightness in a cylindrical luminous medium with self-absorption. *Journal of the Optical Society of America* 50, 826-830.
26. Gharib, M. 1986. Flow velocity measurements by image processing of optically modulated tracers. *AGARD-CP.* 413, 22.
27. Gouldin, F. C. and Dandekar, K. V. 1984. Time-resolved density measurements in premixed turbulent flames. *AIAA J* 22, 655-663.
28. Gouldin, F. C. 1987. An application of fractals to modelling premixed turbulent flame. *Combustion and Flame* 68, 249-266.
29. Gouldin, F. C. 1988. Interpretation of jet mixing using fractals. *AIAA J* 26, 1405-1407.
30. Gouldin, F. C., Bray, K. N. C. and Chen, J. Y. 1989. Chemical closure model for fractal flamelets. *Combustion and Flame* 77, 245-259.
31. Goldstein, R. J. 1983. *Fluid Mechanics Measurements.* USA Hemisphere Publishing Corporation.
32. Gonzalez, R. C. and Wintz, P. 1989. *Digital Image Processing.* Addision-Wesley Publishing Company.
33. Gutmark, E., Parr, T. P, Hanson-Parr, D. M. and Schadow, K. C. 1989. Azimuthal structure of an annular diffusion flame. *Combustion and Flame* 75, 229-240.

34. Gutmark, E., Parr, T. P., Hanson-Parr, D. M. and Schadow, K. C. 1991. Simultaneous OH and Schlieren visualization of premixed flames at the lean blow-out limit. *Experiments in Fluids* 12, 10-16.
35. Hama, F. R. 1962. Streakline in a perturbed shear flow. *The Physics of fluids.* 5, 644-650.
36. Hamming, R. W. 1974. *Numerical Methods for Science and Engineers.* New York, McGraw-Hill.
37. Hentschel, H. G. E. and Procaccia, I. 1984. Relative diffusion in turbulent media: The fractal dimension of clouds. *Physical Review A, General Physics* 29, 1461-1470.
38. Hinze, J. L. 1975. *Turbulence* (2nd edition). Mcgraw Hill, New York.
39. Huang, H. T., Fiedler, H. E. and Wang, J. J. 1993. Limitation and improvement of PIV (Part 1). *Experiments in Fluids* 15, 168-174.
40. Huang, H. T., Fiedler, H. E. and Wang, J. J. 1993. Limitation and improvement of PIV (Part 2). *Experiments in Fluids* 15, 263-273.
41. Hussain, A. K. M. F. 1981. Coherent structures and studies of perturbed and unperturbed jets. *Lecture notes in physics* 136. Springer-Verlag, Berlin.
42. Johnston, S. C., Dibble, R. W., Schefer, R. W., Ashurst, W. T. and Kollmann, W. 1985. Laser measurements and stochastic simulations to turbulent reacting flows. *AIAA J.* 26, 918-937.
43. Libby, P. A. and Bray, K. N. C. 1980. Implications of the laminar flamelet model in premixed turbulent combustion. *Combustion and Flame* 39, 33-41.
44. Lovejoy, S. 1982. Area-perimeter relation for rain and cloud areas. *Science* 216, 185.
45. Lumley, J. L. 1970. *Stochastic Tool in Turbulence.* Academic Press, New York.
46. Lysaght, A. J. R., Bilger, R. W. and Kent, J. H. 1982. Visualisation of mixing in turbulent diffusion flames. *Combustion and Flame* 46, 104-108.
47. Mandelbrot, B. B. 1975. On the geometry of homogeneous turbulence, with stress on the fractal dimension of iso-surfaces of scalars. *Journal of Fluid Mechanics* 72, 401-416.
48. Mandelbrot, B. B. 1983. *The Fractal Geometry of Nature.* Freeman, New York.
49. Meneveau, C. and Sreenivasan, K. R. 1991 The multifractal nature of turbulent energy dissipation. *Journal of Fluid Mechanics* 224, 429-484.
50. Merzkirch, W. 1987. *Flow Visualization.* Academic Press, London.
51. Miake-Lye, R. C. and Toner, S. R. 1987. Laser soot imaging of a large buoyant diffusion flame. *Combustion and Flame* 67, 9-26.

52. Minerbo, G. N. and Levy, M. E. 1969. Inversion of Abel's integral equation by means of orthogonal polynomials. *SIAM Journal of Numerical Analysis* 6, 598-616.
53. Nestor, O. H. and Olsen, H. N. 1960. Numerical methods for reducing line and surface probe data. *SIAM Review* 2, 200-207.
54. Oppenheim, A. V. and Schafer, R. W. 1989. *Discrete-time Signal Processing*. Prentice-Hall Inc., Englewood Cliffs, New Jersey.
55. Paschereit, C. O., Oster, D., Long, T. A., Fiedler, H. E. and Wygnanski, I.. 1992. Flow visualization of interactions among large coherent structures in an axisymmetric jet. *Experiments in Fluids* 12, 189-199.
56. Peitgen, Heinz-Otto 1988. *The Science of Fractal Images*. Springer-Verlag, New York.
57. Peters, N. 1986. Laminar flamelet concepts in turbulent combustion. *Twenty-first Symposium (International) on Combustion / The Combustion Institute*, pp. 1231-1250.
58. Rajan, S., Smith, J. R. and Ramback, G. D. 1984. Internal structure of turbulent premixed flame using Rayleigh scattering. *Combustion and Flame* 57, 95-107.
59. Rerkshanandana, P. 1989. *Investigation of Flow Structures in Passive and Reactive Turbulent Mixing*. PhD Thesis. Department of Civil and Mechanical Engineering of University of Tasmania.
60. Sreenivasan, K. R. and Meneveau, C. 1986. The fractal facets of the turbulent. *Journal of Fluid Mechanics* 173, 356-386.
61. Sreenivasan, K. R. and Prasad, R.R. 1989. New results on the fractal and multifractal structure of the large Schmidt number passive scalars in the fully turbulent flows. Physica D 38: 322-329.
62. Sreenivasan, K. R. 1991. The fractal and multifractals in fluid turbulent. *Annual Review in Fluid Mechanics* 23, 539-600.
63. Suzuki, T. and Hirano, T. 1984. Dynamic characteristics of flame fronts in a turbulent premixed flame zone. In *Twentieth Symposium (International) on Combustion / The Combustion Institute*, pp. 437-444.
64. Tennekes, H. and Lumely, J. L. 1972. *A First Course in Turbulence*. M.I.T. Press, Cambridge, Massachussetts.
65. Takeno, T., Murayama, M. and Tanida, Y. 1990. Fractal analysis of turbulent premixed flame surface. *Experiment in Fluids* 10, 61-70.
66. Tanna, H. K. and Ahuja, K. K. 1985. Tone Excited Jets, Part 1: Introduction. *Journal of Sound and Vibration* 102, 57-61.
67. Vernon, D. 1991. *Machine Vision*. Prentice Hall International (UK) Ltd.

68. Weinberg, F. J. 1963. *Optics Of Flames*. Butterworths, London.
69. William, H. P., Brian, P. F., Saul, A. T. and William, T. V. 1989. *Numerical Recipes in Pascal-The Art of Scientific Computing*. Cambrige University Press.
70. Wilson, L. N. and Damkevala, R. F. 1970. Statistical properties of turbulent density fluctuations. *Journal of Fluid Mechanics* 43, 291-303.
71. Winant, C. D. and Browand, F. K.. 1974. Vortex pairing: the mechanism of turbulent mixing-layer growth at moderate Reynolds number. *Journal of Fluid Mechanics* 63, 237-255.
72. Winarto, H. 1973. *Axisymmetric Turbulent Jet Diffusion Near the Ground.* MEngSci Thesis. School of Mechanical and Industrial Engineering, University of N.S.W., Sydney, Australia.
73. Winarto, H. 1979. *Turbulent Density Structures of Jets and Flames.* PhD Thesis. The School of Mechanical and Industrial Engineering of University of New South Wales.
74. Winarto, H. and Davis, M. R. 1984. Fluctuations of density, pressure and temperature in a turbulent mixing region. *Proceedings of the Royal Society of London* (Part A) 395, 203-228.
75. Wu, C. K. and Law, C. K. 1984. On the determination of laminar flame speeds from stretched flames. *Twenty Symposium (International) on Combustion / The Combustion Institute*, pp. 1941-1949.